

**Statistical Study of X-ray Jets using  
Hinode/XRT**

**Nobuharu Sako**

**The Graduate University for Advanced Studies [SOKENDAI]  
Department of Astronomical Science**

**August 13, 2014**

# Abstract

X-ray jets have been first discovered by soft X-ray telescope (SXT) onboard the *Yohkoh* satellite. X-ray jets in active regions (ARs) have been studied using the data by *Yohkoh*/SXT, and magnetic reconnection has emerged as the mechanism of X-ray jets. A model of X-ray jets by reconnection has been thus proposed. X-ray telescope (XRT) aboard the *Hinode* satellite, which is improved in terms of the time and spatial resolutions compared to *Yohkoh*/SXT, has been observing a complex and transient dynamics of jets. In addition, we can study X-ray jets not only in ARs but also in coronal holes (CHs) and quiet regions (QRs) because the temperature response of XRT has a sensitivity of both cool and hot coronal plasmas (1-10 MK in temperature). There are unresolved questions about X-ray jets arising from results by *Hinode*/XRT, such as regional difference in characteristics of X-ray jets and the acceleration mechanism of X-ray jets. We would like to answer these questions. In this thesis, we are to investigate characteristics of X-ray jets in CHs and QRs, to reveal whether X-ray jets by different acceleration mechanism can exist in ARs, QRs, and CHs or not. To our knowledge, in no other studies were analyzed more events than we did; we thus believe that the current study provides the most thorough and extensive views of X-ray jets in the solar corona.

In Chapter 2, we analyze 478 X-ray jets and 1174 transient brightenings around the north pole and 48 X-ray jets and 82 transient brightenings in the equatorial quiet regions near the limbs. We investigate the occurrence rates of X-ray jets and transient brightenings in the polar regions as function of distance from the boundaries of CHs. These rates show that coronal active events in the polar CHs occur uniformly in space, while most of the coronal activity in the polar QRs occurs adjacent to and equatorwards of the boundaries of the CHs. The mean occurrence rate of X-ray jets in the coronal hole boundary regions (CHBs) is 2 to 3 times higher than that in the polar coronal holes (PCHs), polar quiet

regions (PQRs), and equatorial quiet regions (EQRs). The mean occurrence rate of transient brightenings in the CHBs is 8 times higher than that in the PCHs, PQRs, and EQRs. No large differences in the measured physical parameters (e.g. length, lifetime) are found for the X-ray jets or transient brightenings in the PCHs, CHBs, PQRs, and EQRs. The distribution of the directions of the X-ray jets is shown the different characteristics in such coronal regions. Magnetic fields in PCHs are almost radial, while magnetic fields in CHBs have a super radial structure. Closed loops in PQRs and EQRs are rather randomly oriented.

We develop a new scheme for X-ray jet detection using X-ray images in CHs and QRs obtained by *Hinode*/XRT, in Chapter 3. As a by-product, the shape and its time evolution of each X-ray jet were also obtained. To evaluate performance of our scheme, we have applied our scheme to X-ray images that include CHs and QRs within their field of view. We have found that 70% of the selected events in CHs by our scheme are X-ray jets, and are isolated from neighboring events. On the other hand, the rate in the QRs is less than 30%. The poor rate is mainly caused by co-temporal brightenings in neighboring regions. Of the X-ray jets detected by visual inspection, 60% in the CHs and 25% in the QRs can be detected by our scheme. Advantages of our scheme are that we can identify X-ray jets with weak enhancements which do not permit identification by visual inspection, and that we can reconstruct the morphology of the jet structure from the parameters obtained.

In Chapter 4, we analyze 31 X-ray jets in the ARs, 59 X-ray jets in the QRs, and 60 X-ray jets in the CHs and classify the jets into the evaporation jets and the magnetic-driven jets. No large differences in the morphological parameters (length and width of the jets, and area of footpoint flares) are found for jets in the ARs, the QRs, and the CHs. The jet speed and the thermal energy of the footpoint flare in the ARs, however, are larger than those in the QRs and the CHs. We estimate the temperature of the jet structures from the thermal energy of the footpoint flare based on the assumptions described in Shimojo & Shibata (2000). The temperature of the jets in the ARs is found to be higher than those of the jets in the QRs and the CHs. We classify the X-ray jets in the ARs, the QRs, and the CHs into

either the evaporation jet or the magnetic-driven jet using the speed and the temperature of the jets. We find that both evaporation and magnetic-driven jets are produced in the ARs, the QRs, and CHs.

# Contents

<b>Abstract</b>	<b>ii</b>
<b>1 Introduction</b>	<b>1</b>
1.1 Coronal Jets: Overview . . . . .	1
1.2 Coronal Jets: Observational Results . . . . .	7
1.2.1 Physical Parameters of Coronal Jets . . . . .	7
1.2.2 Morphology & Dynamics of Coronal Jets . . . . .	11
1.2.3 Magnetic Fields Associated with Coronal Jets . . . . .	16
1.2.4 Relationship between Coronal Jets and Chromospheric Jets . . . . .	17
1.2.5 Hard X-ray and Radio Burst Associated with Coronal Jets . . . . .	18
1.3 Coronal Jet: Theoretical Results . . . . .	18
1.3.1 Models of Coronal Jets by Magnetic Reconnection . . . . .	19
1.3.2 Acceleration Mechanism of Coronal Jets . . . . .	24
1.3.3 Simulation Results . . . . .	26
1.4 Research Subjects in This Thesis . . . . .	32
1.4.1 Some Unresolved Questions . . . . .	32
1.4.2 Content of the Thesis . . . . .	34
<b>2 A Statistical Study of Coronal Active Events in the North Polar Region</b>	<b>36</b>
2.1 Abstract . . . . .	36
2.2 Introduction . . . . .	37
2.3 Observations and Data Analysis . . . . .	38

2.3.1	Observations . . . . .	38
2.3.2	Detection . . . . .	39
2.3.3	Derivation and Estimation of Parameters of Detected Events . . .	46
2.4	Results . . . . .	48
2.4.1	Classification of Polar Regions based on X-ray Intensity . . . . .	48
2.4.2	Influence of X-ray Background Level on Detection of Events . .	50
2.4.3	Occurrence Rate as Function of Distance from Coronal Hole Bound- ary . . . . .	54
2.4.4	Daily Occurrence Rate of X-ray Jets and Transient Brightenings .	58
2.4.5	Parameters of X-ray jets and transient brightenings . . . . .	62
2.4.6	Frequency Distributions as Function of X-ray Intensity in Foot- point Flares . . . . .	65
2.4.7	Direction of X-ray Jets . . . . .	68
2.5	Summary and Discussion . . . . .	71
2.5.1	Fast Solar Wind Acceleration by X-ray Jets in PCHs . . . . .	72
2.5.2	Difference in Occurrence Rates of Transient Brightenings between the Regions . . . . .	75
<b>3</b>	<b>A New Scheme for Detecting X-ray Jets in Coronal Holes and Quiet Regions</b>	<b>78</b>
3.1	Abstract . . . . .	78
3.2	Introduction . . . . .	79
3.3	Auto detection of X-ray jets . . . . .	81
3.3.1	Preprocessing . . . . .	81
3.3.2	Estimation of the Background Level and High-Lighting of the Jet Structure . . . . .	84
3.3.3	Binarization . . . . .	89
3.3.4	Reconstruction Scheme of Jet Structures . . . . .	92

3.3.5	Identification of Individual Active Events and Detection of Their Shapes . . . . .	94
3.3.6	Selection of X-ray Jets Based on Morphology and Time Evolution . . . . .	94
3.3.7	Cut-off Process caused by Limitation of Scheme . . . . .	98
3.4	Performance Evaluation of Scheme . . . . .	99
3.4.1	Observational Data for Evaluation . . . . .	99
3.4.2	How Many Candidate Events Correspond to Actual X-ray Jets? . . . . .	99
3.4.3	How Many X-ray Jets Detected by Visual Inspection Does Our Scheme Detect? . . . . .	103
3.5	An Application Example . . . . .	106
3.6	Summary . . . . .	109
<b>4</b>	<b>A Study of Acceleration Mechanisms of X-ray Jets</b>	<b>111</b>
4.1	Abstract . . . . .	111
4.2	Introduction . . . . .	112
4.3	Observation Data and Analysis Methods . . . . .	115
4.3.1	Observation Data . . . . .	115
4.3.2	Event Identification and Selection . . . . .	115
4.3.3	Measurement and Estimation of Parameters . . . . .	117
4.4	Estimated Parameters . . . . .	125
4.4.1	Morphological Parameters . . . . .	127
4.4.2	Jet Speed . . . . .	127
4.4.3	Thermal Energy and Heating Flux of Footpoint Flare . . . . .	128
4.4.4	Temperature of Footpoint Flare and Jet Structure . . . . .	128
4.5	Acceleration Mechanism of Jet . . . . .	134
4.5.1	Evaluation of Range For Temperature and Speed. . . . .	134
4.5.2	Identification of Jet Type Based on Temperature and Speed . . . . .	138
4.5.3	Multi-Jet Structures . . . . .	140

4.6	Summary and Discussion . . . . .	146
<b>5</b>	<b>Summary and Future Directions</b>	<b>152</b>
5.1	Summary of Our Results . . . . .	152
5.2	Remaining Questions and Future Directions . . . . .	153
	<b>Reference</b>	<b>156</b>
	<b>Acknowledgments</b>	<b>164</b>

# Chapter 1

## Introduction

### 1.1 Coronal Jets: Overview

A solar flare is an explosive event in the solar atmosphere, and is the largest explosion in our solar system. The amount of energy released by a flare varies. We roughly categorize the flares into the following classes based on the released energy: flare ( $10^{29}$ - $10^{32}$  erg), microflare ( $10^{26}$ - $10^{29}$  erg), and nanoflare ( $10^{23}$ - $10^{26}$  erg). Occasionally, a microflare is called a 'transient brightening' (Shimizu et al., 1992). While flares occur only in active regions, microflares and nanoflares occur at everywhere in the Sun, even in coronal holes. The solar flares, including smaller flares, sometimes are associated with dynamic plasma motions. A 'coronal jet' is a kind of such solar flare. The structure of most coronal jets comprises two components, which is illustrated in Figure 1.1 (Shibata et al. 1992 and Shimojo et al. 1996). One component is 'jet structure', which elongates with time (Figure 1.2). Because the jet structure corresponds to the blue-shift doppler motion by EUV spectroscopic observation (e.g. Kamio et al. 2007, Chifor et al. 2008a), it is considered a plasma flow. The other component is 'footpoint flare', which is located around the footpoint of the jet structure. The coronal jet observed by X-ray and extreme-ultraviolet (EUV) are called an 'X-ray jet' and an 'EUV jet', respectively. From temperature diagnostics using soft X-ray images, the temperature of the X-ray jets is estimated to be above

1 MK (Shimojo & Shibata, 2000). The temperature of EUV jets is considered to be the formation temperature of the spectral lines. The coronal jets can be observed by the EUV spectroscopic instrument using the spectral lines that the formation temperature is above coronal temperature ( $> 1$  MK). Throughout this thesis, we refer 'EUV jets' as coronal jets seen in EUV emission lines, unless otherwise stated. The morphology of EUV jets is similar to that of X-ray jets (e.g. Alexander & Fletcher 1999, Kim et al. 2007, and Chifor et al. 2008a).

X-ray jets were first discovered from X-ray images obtained by the Soft X-ray Telescope (SXT, Tsuneta et al. 1991) aboard the *Yohkoh* satellite (Ogawara et al. 1991) as reported by Shibata et al. (1992). The *Yohkoh*/SXT observation revealed dynamical and morphological characteristics of X-ray jets mainly taking place in the active regions. Based on the observational results, Shibata et al. (1992) proposed a model of X-ray jets based on magnetic reconnection (Figure 1.3). In this model, initial coronal magnetic fields are unipolar, and the bipolar fields emerge or approach to form current sheets. The current sheet then evolves to initiate magnetic reconnection, and a coronal jet is produced by the magnetic reconnection. The other jet-event (e.g. chromospheric jet) is considered to produce by the magnetic reconnection.

After the launch of the *Hinode* satellite, there are the data by the X-ray and EUV telescopes (XRT, EIS, and AIA). The performance of these telescopes significantly improved from SXT, and the details of coronal jets are revealed. In particular, the recent data show that the dynamics and morphology of jet structures are complicated. The complexity of jet structures might play an important role for the process of releasing the energy by magnetic reconnection. Meanwhile, the improved X-ray and EUV telescopes show us that coronal jets frequently occur not only in active regions (ARs) but also in coronal holes (CHs) and quiet regions (QRs). Based on these results, some authors have considered the coronal jets as a candidate of the energy and mass source of solar wind. We can also study about accelerated plasma of the jet (acceleration driver, temporal and spatial behavior of the accelerated plasma). This result is helpful to understand the dynamics of not only

other solar jets (e.g. spicule, surge) but also astrophysical jets.

In the remaining of this chapter, we review observational aspects and theoretical interpretations of coronal jets, and finally we present the objectives of this thesis. Finally we present the goals of the study.

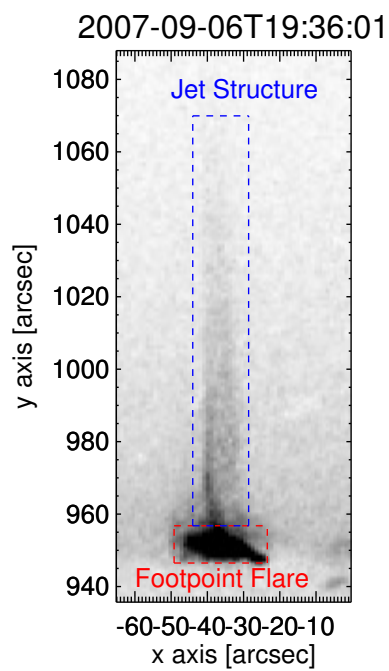


Figure 1.1: X-ray jet around the north pole on September 6th, 2007. The gray scale is reversed. The red dashed box indicates the footpoint flare and the blue dashed box show the jet structure.

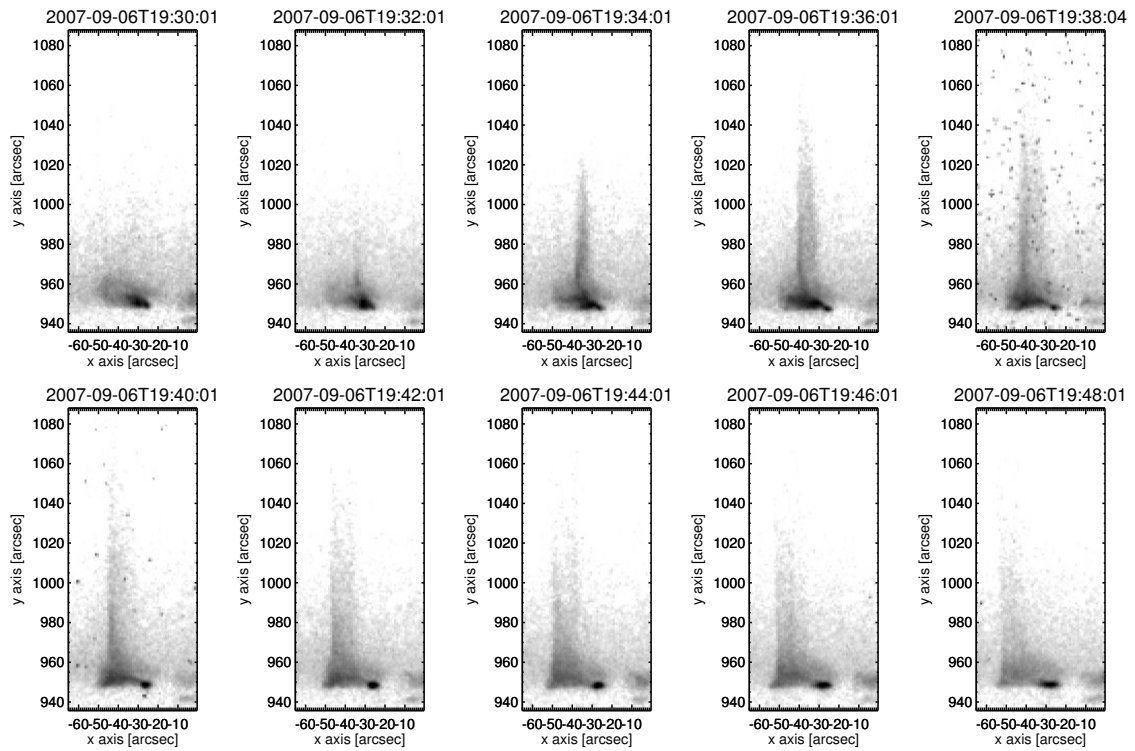


Figure 1.2: Time evolution of the X-ray jet in Figure 1.1. The color scale is reversed. Time between each panel is 120 seconds.

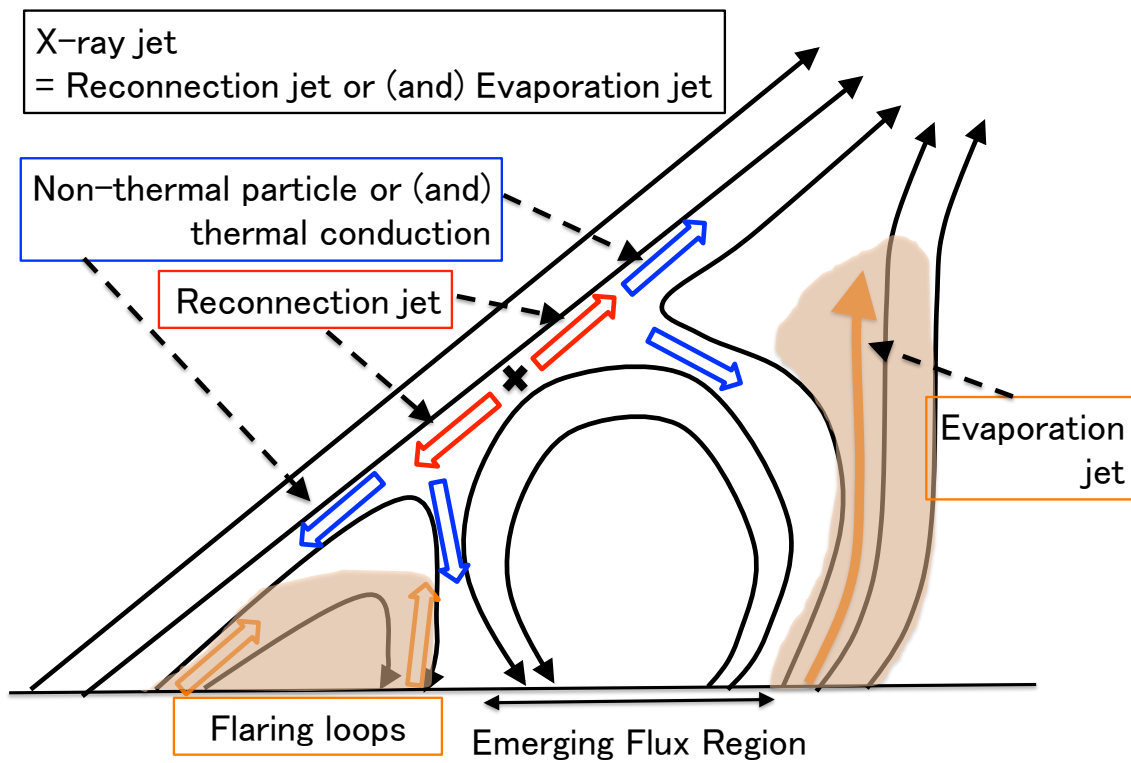


Figure 1.3: Illustration of X-ray jets in the model by magnetic reconnection based on Figure 3.10 by Shimojo (1999)

## 1.2 Coronal Jets: Observational Results

### 1.2.1 Physical Parameters of Coronal Jets

We first review characteristics of coronal jets found by statistical studies.

Table 1.1 is a summary of the ranges and the typical values of the apparent length, the lifetime, the width, and the apparent speed of coronal jets. Because the difference in the characteristics of the observing instruments, between SXT and XRT, affected the process of deriving these parameters (Savcheva et al. 2007), parameters obtained by SXT are not to be directly compared with those by XRT. The results by Savcheva et al. (2007) used only the X-ray jets in the polar CHs along the vertical direction in the polar field of view. There is no statistical study for these parameters in ARs, QRs, and CHs obtained by XRT

The speed of a jet is an important parameter for discussing the acceleration mechanism of the jet. The jet's speed is expected to be a sound speed or an Alfvén speed by different acceleration mechanism. Because both the sound speed and the Alfvén speed vary, however, we cannot distinguish the acceleration mechanism by the jet's speed alone. Certain et al. (2007) reported that four jets in the polar CHs have the multi jet structures with speeds of  $200 \text{ km s}^{-1}$  and  $800 \text{ km s}^{-1}$ . There are few observational reports for jets near  $800 \text{ km s}^{-1}$ . To detect the jet with the sound speed, some studies investigated a relationship of the observed speed with the temperature of the jet (Shimojo & Shibata 2000, Chifor et al. 2008a, Matsui et al. 2012, and Tian et al. 2012). Chifor et al. (2008a) and Matsui et al. (2012) showed the speed increases with temperature, as evidence of the sound speed. Matsui et al. (2012) and Tian et al. (2012) reported two types of the jet's speed, one depending on the temperature, the other, that is nearly constant.

EUV spectroscopic observations (ex. *SOHO*/SUMER and *Hinode*/EIS) provide information of the line-of-sight plasma motion. Some studies clearly show the blue-shift motion of the X-ray jet (e.g. Kamio et al. 2007, He et al. 2010). Kamio et al. (2007) found both the blue-shift motion of the jet structure and the red-shift motion of the footpoint flare.

This result is interpreted as the bi-directional jet produced by magnetic reconnection.

The jet structure also moves transversely, i.e. in the direction to perpendicular to the elongation. The speed of transverse motion is 0-35 km s<sup>-1</sup> (Shibata et al. 1992, Savcheva et al. 2007, and Savcheva et al. 2009). A detail of the transverse motion is shown in Section 1.2.2.

Some studies perform the temperature diagnostic using the intensity of jet structures and footpoint flares. A summary of the temperature and the plasma number density of the jet structure and the footpoint flare is shown in Table 1.2. Because these results were obtained by the different analysis methods and the instruments, we cannot directly compare the temperature and number density in Table 1.2. Shimojo & Shibata (2000) found the temperature of the jets in ARs is similar to that of the footpoint flares. The estimated thermal energies of the jets in ARs are 10<sup>27</sup>-10<sup>29</sup> ergs. They also found the correlation between the thermal energy of the jets and those of the footpoint flares and between the thermal energy of the jets and the kinetic energy of the jets. The thermal energy of the footpoint flares is about 4-7 times the thermal energy of the jets and the thermal energy of the jets is about three times the kinetic energy of the jets.

The event number of X-ray jets is considered as a proxy of coronal activities. From the *Yohkoh*/SXT observations, Shimojo et al. (1996) reported 66 X-ray jets in ARs, 13 X-ray jets in QRs, and 11 X-ray jets in CHs during 6 months around the solar maximum. So it indicates that the coronal activity in ARs higher than those in QRs and CHs. From the observation by *Hinode*/XRT, however, X-ray jets frequently occur in PCHs. Savcheva et al. (2007) showed that the number of X-ray jets in the polar CHs with the vertical direction is 60 events day<sup>-1</sup>. The difference in the characteristics between SXT and XRT affected the difference of the event number of the X-ray jets. The coronal jets also frequently occur around the boundary of CHs (Subramanian et al. 2010, Yang et al. 2011). Subramanian et al. (2010) showed the event number of the transient brightenings with the outflow per 100×100 arcsec<sup>2</sup> per day is 52 in the CH and around boundary of the CH, while it is 6 in the QR.

Table 1.1: Parameters of coronal jets

Paper	1	2	3
Region	AR(70%),QR(10%),CH(10%)	PCH	PCH,ECH
Instrument	SXT	XRT	SECCHI
Lifetime	1.6-270		20-40
(minute)		(10)	(30)
Length	a few-40	1.0-12	
( $10^4$ km)	(15)	(5)	
Width	5-100	6-10	
( $10^3$ km)	(18)	(8)	
Speed	10-1000		
( $\text{km s}^{-1}$ )	(200)	(160)	(200)

AR: active region, QR: quiet region, CH: coronal hole

PCH: polar CH, ECH: equatorial CH

Paper 1 is Shimojo et al. (1996), Paper 2 is Savcheva et al. (2007), and

Paper 3 is Nisticò et al. (2009) and Nisticò et al. (2010).

Parentheses indicate the typical value (e.g. average, median).

Table 1.2: Temperature and number density of coronal jets

Paper	1	2	3	4	5
Region	AR	AR	PCH	ECH,EQR	ECH
Instrument	SXT	SXT	EIS	EIS,SUMER	EIS
Filters or Lines	Al.1 AlI	Al 12 m AlMgMn	Fe XII 186.8Å Fe XII 195.1Å	Fe XII 186.88Å Fe XII 195.12Å	Fe XII 186.88Å Fe XII 195.12Å
$T_{\text{jet}}$ (MK)	3-8 (5.6)	6-8.5	0.3-2.2 (1.4)	-2.5	1.6
$T_{\text{flare}}$ (MK)	4-8 (5.6)		(1.3)	-2.5	-3 1.3
$N_{\text{jet}}$ ( $10^8 \text{ cm}^{-3}$ )	7-40 (17)	2-3	-10	(5.8)	0.9-1.7
$N_{\text{flare}}$ ( $10^8 \text{ cm}^{-3}$ )	24-100 (5.4)		-10	(3.2)	7.6

AR: active region, QR: quiet region, CH: coronal hole  
PCH: polar CH, ECH: equatorial CH, EQR: equatorial QR  
Paper 1 is Shimojo & Shibata (2000), Paper 2 is Kim et al. (2001),  
Paper 3 is Doschek et al. (2010), Paper 4 is Madjarska et al. (2012),  
and Paper 5 is Young & Muglach (2014).  
Paper 5 also used a pair of Fe XIII 203.82Å and Fe XIII 202.04Å.

## 1.2.2 Morphology & Dynamics of Coronal Jets

To understand the mechanism of the jets, we need to know the dynamics of the jet structure observationally. A width of the jet structure is a parameter, which characterizes the dynamics of jets. Shimojo et al. (1996) first show five morphology types of the jet structure using 100 X-ray jets based on difference in the width between at the bottom and at the top of the jet structure:

- Converging: The width of the jet decrease with the distance (33 events).
- Constant: The width of the jet is nearly constant (43 events).
- Diverging: The width of the jet increase with the distance (14 events).
- Undulating: The jet shows an undulating configuration (6 events).
- Untwisting: The jet appears to be untwisting (4 events).

They found that the most common jet is the constant type and that the second is the converging type. The observation by *Hinode*/XRT shows the fine structure of the jet and details of the time evolution of the jet. Shimojo et al. (2007), Moore et al. (2010), and Moore et al. (2013) reported the width of the jet structure near the footpoint flare expands with time. Figure 1.4 is an example of the expansion of the jet structure near a footpoint flare widthways.

After the *Hinode* launch, detailed studies for time evolution and complex structures of jets are reported. We propose an additional classification of the jet structure from XRT observation.

- Untwisting motion

Both types of events exist in which the coronal jet untwists and don't untwist during the elongation of the jet. Kamio et al. (2010) reported that the chromospheric jet with the untwisting motion associated with the X-ray jet, which is a radial outflow. To produce jets for the untwisting type, the closed field before reconnection must be

twisted changing to open field by reconnection. One possible interpretation could be that the guide field for elongating the chromospheric jet differs from that for the coronal jet.

- **Transverse Motion**

The jet move transversely and the speed of the transverse motion is presented in Section 1.2.1. Because the transverse motion is observed during the elongation of the jet structure, this motion is associated with the energy release by magnetic reconnection. There are two types of the transverse motion observationally. One is the transverse oscillation (Cirtain et al. 2007, Chandrashekhara et al. 2014b, and Zhang & Ji 2014). The undulating type by Shimojo et al. (1996) is a group of the transverse oscillation. Some studies predicted the creation of the wave by transverse oscillation. The other type shows only the transverse motion, but not oscillation (Shibata et al. 1992, Shimojo et al. 2007, Savcheva et al. 2007, Savcheva et al. 2009, and Chandrashekhara et al. 2014a). Chandrashekhara et al. (2014a) first reported a uniform transverse speed at different heights of the coronal jet.

- **Recurrent Jet**

Coronal jets taking place at the same location are called a 'recurrent jet'. There are two kinds of the recurrent jet classified by their time intervals. One type is the time difference of a few hours (AR; Jiang et al. 2007, Yang et al. 2011, Zheng et al. 2013, and Guo et al. 2013, CH; Wang & Sheeley 2002, Savcheva et al. 2007, and Zhang et al. 2012). Because this jet occurs periodically, the mechanism to store the free energy and to produce the recurrent jet can be studied. The other is that multiple-jet structures occur during a lifetime of the recurrent jet, which is from an appearance to a disappearance of a footpoint flare (Chae et al. 1999, Cirtain et al. 2007, Madjarska 2011, and Jiang et al. 2013). Light curves of footpoint flares show

multiple peaks, and the recurrent jet-structures appear at these peaks (Jiang et al., 2013). This result is interpreted that the energy release happens more than once in the footpoint flare, and the jet structures are reproduced corresponding to these energy releases.

- Associated Plasma Eruption

Sometimes, coronal jets observed with the plasma eruption (e.g. Shimojo et al. 2007, Nisticò et al. 2009, Liu et al. 2011). Some studies interpreted that the loop expansion around the footpoint flare causes the plasma eruption. There are both observational reports of the coronal plasma eruption and the chromospheric plasma eruption associated with the jet, respectively (e.g. Moore et al. 2010). A mechanism to trigger the plasma eruption associated with the occurrence of the coronal jet should be further investigated observationally.

A morphological structure of footpoint flares is closely related with the configuration of coronal fields for producing jets. There are some types for the configuration of the footpoint flares. Shimojo et al. (1996) classified 34 events in the 90 events into the 'anemone' type (20 events) and the 'upside-down Y' type (14 events). For the anemone type, the footpoint flare is comprised the multiple loops like a sea anemone (Shibata et al., 1994). For the 'upside-down Y' type, the footpoint flare is constructed of the single loop. Their X-ray jets in the CHs and QRs are classified into the XBP type, which is not resolved the structure of the footpoint flare. From the observation by SECCHI-EUVI, XRT, and AIA, a detail of the configuration of the loop in the footpoint flare in not only ARs but also CHs and QRs is reported. Nisticò et al. (2009) classified 59 coronal jets in 79 events into the two different types of the jet based on the displacement of the coronal jets and the footpoint flares. The 'Eiffel tower' type is roughly same of the 'upside-down Y' type (37 events). The 'Lambda' type, which a small-scale photospheric magnetic bipole recon-

nects with ambient unipolar field lines near its footpoints, is the XBP type in classification by Shimojo et al. (1996). The jet of the 'Lambda' type is the footpoint flare located separately the jet structure, Raouafi et al. (2010) showed that several jets in the CHs erupt from small-scale and S-shape bright regions. The S-shape bright region indicates to store a magnetic helicity, and the large energy release will be caused by reconnection. Pucci et al. (2012) reported that two X-ray jets occurred in a close temporal association with the brightness maxima in multiple XBPs. They suggest the jets result from a significant magnetic connectivity changes.

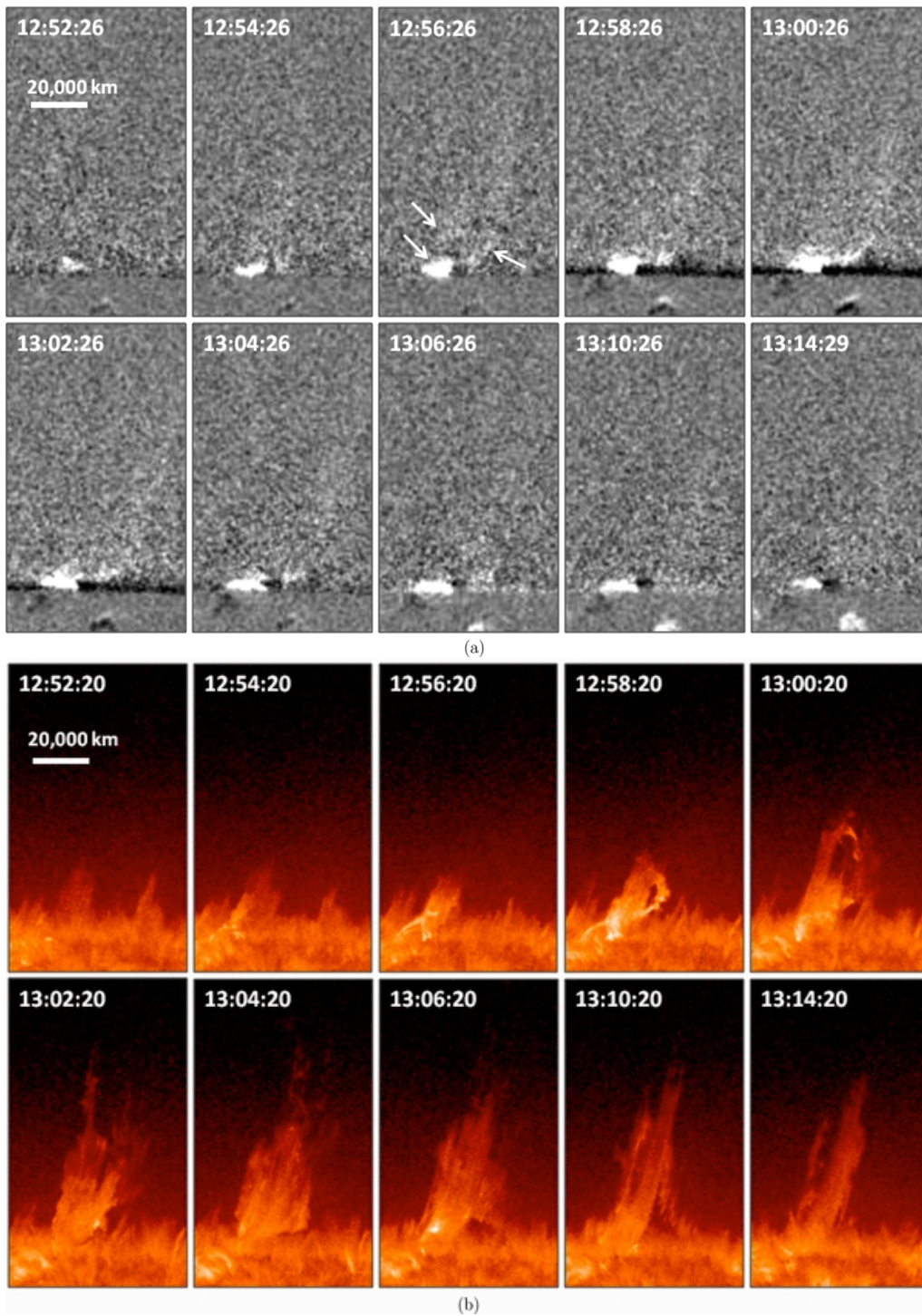


Figure 1.4: Time behavior of the blowout-jet in fixed-difference X-ray images (upper panels) and AIA He II 304 Å channel images (lower panels) (Figures 5a and 5b in Moore et al. 2013). In frame 3, the lower downward-slanting arrow in frame 3 points to the location of the bright point on the limb. The higher downward-slanting arrow points to an outward-moving clot. The upward-slanting arrow points to a bright strand on the jet structure's western edge that has appeared in step with the bright point in the base.

### 1.2.3 Magnetic Fields Associated with Coronal Jets

We can roughly guess the magnetic configuration of the coronal jets from the displacement of the magnetic field in the photosphere. Shimojo et al. (1998) found that 72% of 25 X-ray jets occurred at the mixed polarity region. They also found that the magnetic flux of the jet-producing region is increasing or decreasing. The decreasing magnetic flux is interpreted as indication of the cancelling magnetic bipole flux. The flux-loss rate (the decreasing magnetic flux divided by a time interval) of AR jets is reported to be around  $10^{15}$ - $10^{16}$  Mx s<sup>-1</sup> (e.g. Jiang et al. 2007, Yang et al. 2011, and Yang et al. 2012), while Huang et al. (2012) reported that the rate in the equatorial CH is  $3.9 \times 10^{14}$  Mx s<sup>-1</sup>. The duration of the magnetic flux decrease is for a few hours. It is not clarified whether the flux-loss rate of AR jets is different from that of CH jets or not. On the other hand, the increasing magnetic flux in the jet-producing region is interpreted as the emerging magnetic flux. So the occurrence of coronal jets is associated with the emerging flux or the cancelling flux.

The X-ray jets frequently occur around the pole from the observation by XRT. The measurement of the vector magnetic fields around the pole needs a high spatial resolution, sensitivity and accuracy. The spectropolarimeter (SP) of the Solar Optical Telescope (SOT) onboard the *Hinode* can investigate the magnetic structure around the pole. A magnetic element with the vertical field to the solar surface is locally concentrated like a patch around the jets and the X-ray bright points (Shimojo & Tsuneta 2009 and Kamio et al. 2009). Large magnetic flux concentrations above  $10^{18}$  Mx (hereafter LMFCs) are stable structures with a lifetime of 5-15 hours (e.g. Tsuneta et al. 2008, Shiota et al. 2012). The LMFCs are located not only in CHs but also in QRs (Ito et al., 2010). Shimojo & Tsuneta (2009) first reported that the polar X-ray jet occur in the emerging flux region. So X-ray jets around the pole also associated with the interaction between the emerging flux and LMFCs. They proposed an idea that the X-ray jet occurs by reconnection between the open fields like a canopy structure rooted into the LMFC and emerging loop structure.

Huang et al. (2012) reported the X-ray jet and the transient brightening occur above the LMFCs and these LMFCs are located at the edge of supergranules.

#### **1.2.4 Relationship between Coronal Jets and Chromospheric Jets**

From multi-wavelength observations of coronal jets, some coronal jets are associated with chromospheric jets (e.g. Shimojo et al. 1996, Canfield et al. 1996, Alexander & Fletcher 1999). About half of coronal jets are associated with chromospheric jets around the pole (Moore et al., 2013). Since there is a large difference in the plasma temperature in the chromosphere (0.01-0.03 MK) and in the corona (above 1 MK), the coronal jet and the chromospheric jet are called a 'hot jet' and a 'cool jet', respectively. Examples of both hot and cool jets are shown in Figure 1.4.

There are two types in a temporal relationship between the cool jet and the hot jet. One is that the cool jet occurs simultaneously with the hot jet, which indicates a multi-thermal structure produced by the same energy release. Other is that the hot jet is delayed by a few minutes after the cool jet (Shibata et al. 1992, Canfield et al. 1996, Alexander & Fletcher 1999, Chae et al. 1999, Zhang et al. 2000, Ko et al. 2005, Nishizuka et al. 2008, and Yang et al. 2012). Some studies compare the position of the hot jet with that of the cool jet to study the magnetic configuration for elongating these jets, and two different cases are reported. One is that the cool is spatially coincident with the hot jet (e.g. Zhang et al. 2000, Kim et al. 2007). This means the both jets elongate along to the same magnetic fields. Other is that the cool jet is contiguous to the hot jet (e.g. Canfield et al. 1996, Chae et al. 1999, and Jiang et al. 2007), which suggests that the hot and the cool jet elongate along different field lines.

### **1.2.5 Hard X-ray and Radio Burst Associated with Coronal Jets**

Non-thermal emissions are observed, when coronal jets appear. The first observational report of the non-thermal emission was made by the Type-III burst, which implies that electrons are accelerated to several tens of keV (e.g. Aurass et al. 1994, Kundu et al. 1995, Raulin et al. 1996). Hard X-ray observations obtained by the *RHESSI* can provide information on the position and the spectrum of the hard X-ray sources. The hard X-ray sources are distributed around the footpoint flare (Fletcher et al. 2001, Chifor et al. 2008b, Christe et al. 2008, Chen et al. 2009, Krucker et al. 2011, Glesener et al. 2012, and Chen et al. 2013). Krucker et al. (2011) reported six events in which the hard X-ray sources over 25 keV are located in the footpoints of the EUV jets. For their two EUV jets, three hard X-ray sources associated with the EUV jet, which clearly correspond to the magnetic configuration of the jets by reconnection (see Figure 1.3). Glesener et al. (2012) found that the hard X-ray sources located at the footpoint flares include the non-thermal components, based on the spectral analysis. Bain & Fletcher (2009) suggest presence of hard X-rays and non-thermal electrons in the jet structure from their observational result.

## **1.3 Coronal Jet: Theoretical Results**

The observational results strongly suggest that reconnection between closed fields and ambient open fields is the mechanism for producing jets. In this section, we review the models of coronal jets produced by magnetic reconnection and the simulation results based on the model.

### 1.3.1 Models of Coronal Jets by Magnetic Reconnection

Shibata et al. (1992) first proposed a 2-D model of X-ray jets by magnetic reconnection. A scenario is as follows: An initial magnetic configuration is ambient unipolar fields (Figure 1.5a). Suppose that one footpoint of the closed fields get closer to the ambient fields with the opposite polarity, and the current sheet is created in between them. There are two ways to get the loop close to the unipolar fields (Figure 1.5b). One is that a magnetic loop surrounding the unipolar fields emerges from the solar interior into the corona. The other is that the coronal loops swept together by photospheric convection. The magnetic reconnection starts at the current sheet in the corona.

After the reconnection, some unipolar fields change to the closed field, and coronal loops are reconnected to the open fields (Figure 1.5c). Released energy by magnetic reconnection heats plasmas in the reconnected closed and open fields, and accelerates coronal jets.

In a model of polar jets proposed by Pariat et al. (2009) the magnetic reconnection takes place in a different way. The initial configuration of this model is illustrated in the upper panel of Figure 1.6, in which the external fields cover axis-symmetric fan-like magnetic structure. The photospheric magnetic feature with the opposite polarity to the external fields is twisted by photospheric motion. Beyond a certain critical twist (helicity), almost axis-symmetric magnetic system became unstable to initiate a 3-D kink-like instability that broke the axis-symmetric structure and immediately induced pervasive reconnection. So a kink-like instability can trigger fast energy release. A high-speed (Alfvénic), massive jet is generated by this impulsive reconnection.

Moore et al. (2010) proposed the 'blowout-jet model' (Figure 1.7) based on the observed features of the X-ray jet and the associated chromospheric jet. The initial configuration of the blowout-jet model is the same with the model by Shibata et al. (1992) except the sheared field lines below the emerging flux region (called the core-arch field, see the top left panel in Figure 1.7). The core-arch field is so strongly sheared and twisted to store free energy enough for driving an ejective eruption. The top right panel in Figure 1.7 shows

the triggering of the eruption of the core-arch field. When the core-arch field erupts, the observed jet structure extends like a curtain. They proposed that multi-time reconnection caused by the erupted core-arch fields (ex. interacting with the ambient fields) would lead to a stronger energy release than that in the model by Shibata et al. (1992), thus called as a blowout jet.

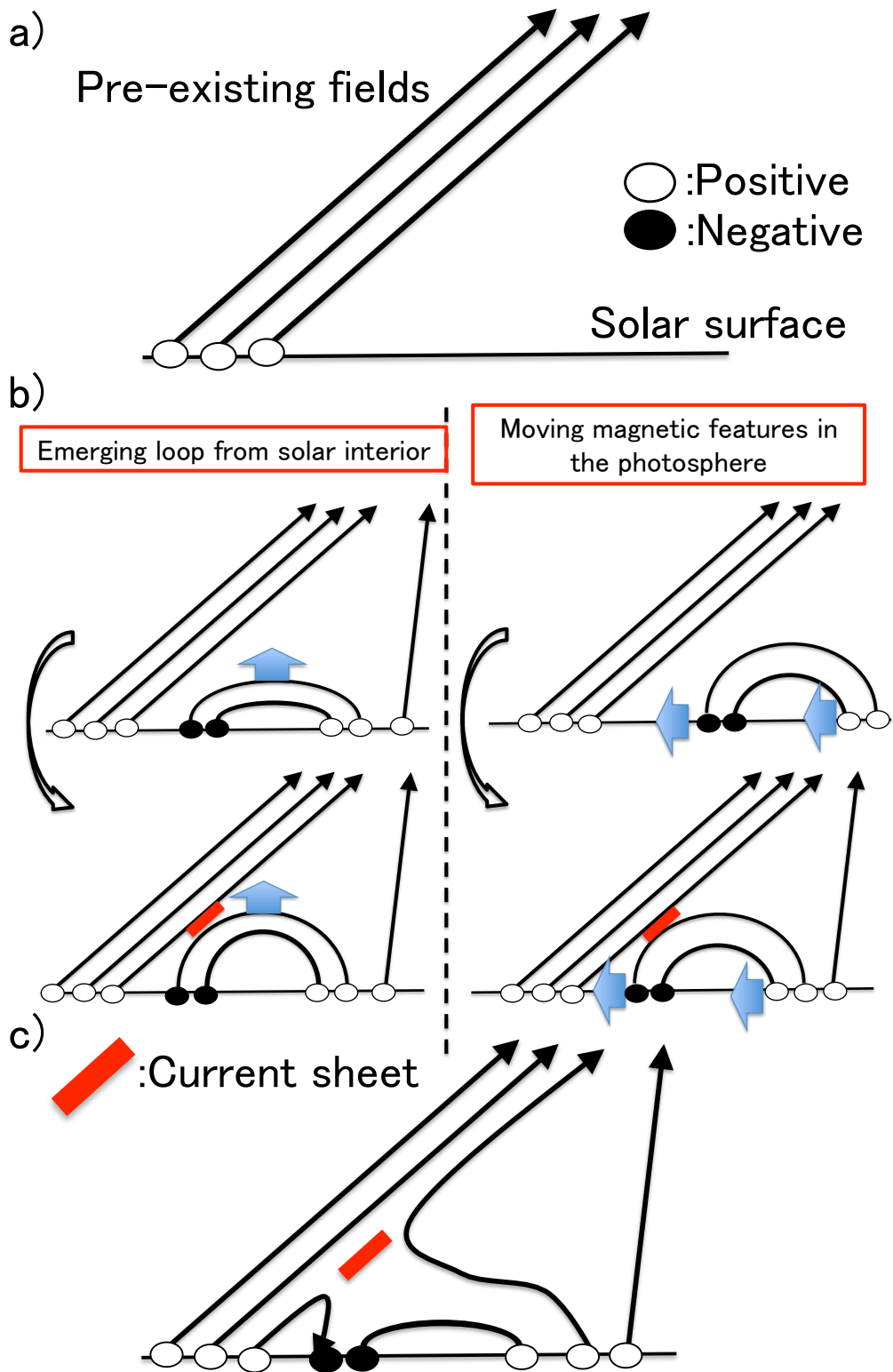


Figure 1.5: Cartoons of magnetic configuration by the model of Shibata et al. (1992)

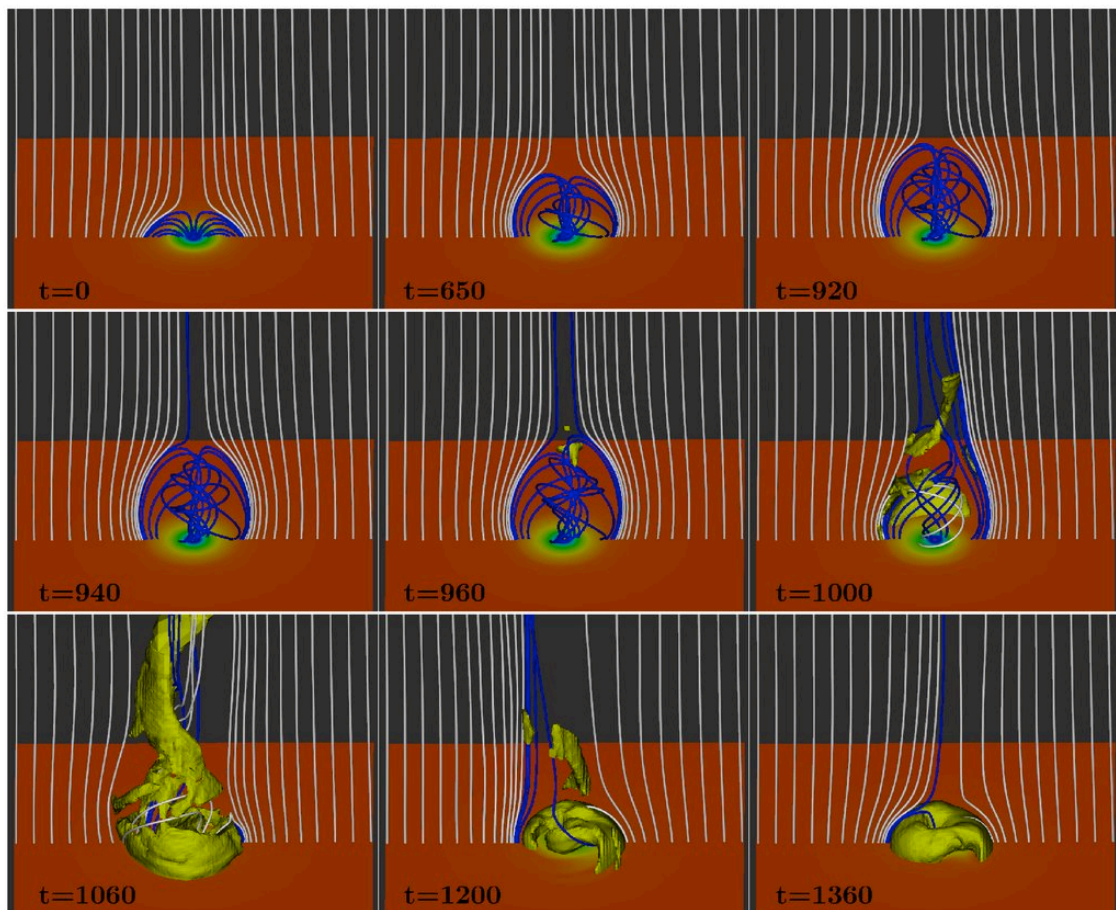
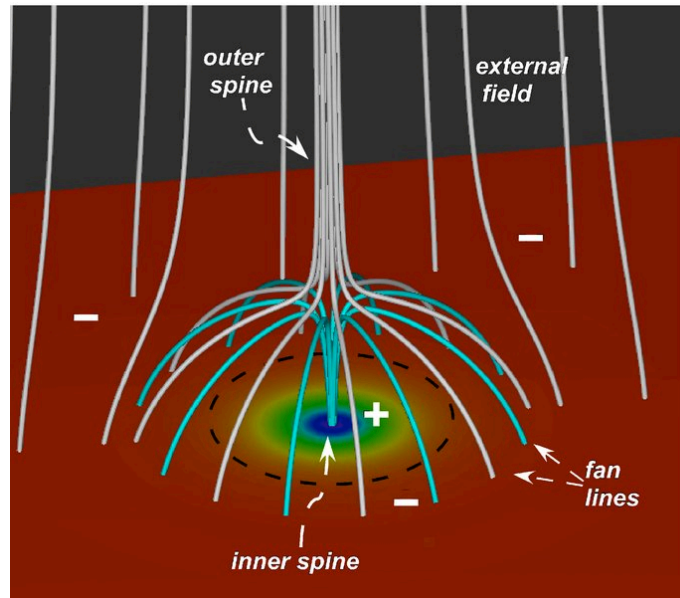


Figure 1.6: The result of the numerical calculation based on the model of polar jet by Pariat et al. (2009). From the initial configuration of their model (upper panel), the time evolution of the magnetic configuration illustrated in the lower panel. The field lines are plotted starting from fixed positions at the bottom boundary along the y-axis. The white ones initially belong to the open connectivity domain, the blue ones to the closed connectivity domain. The yellow isosurfaces show the contour of high mass density.

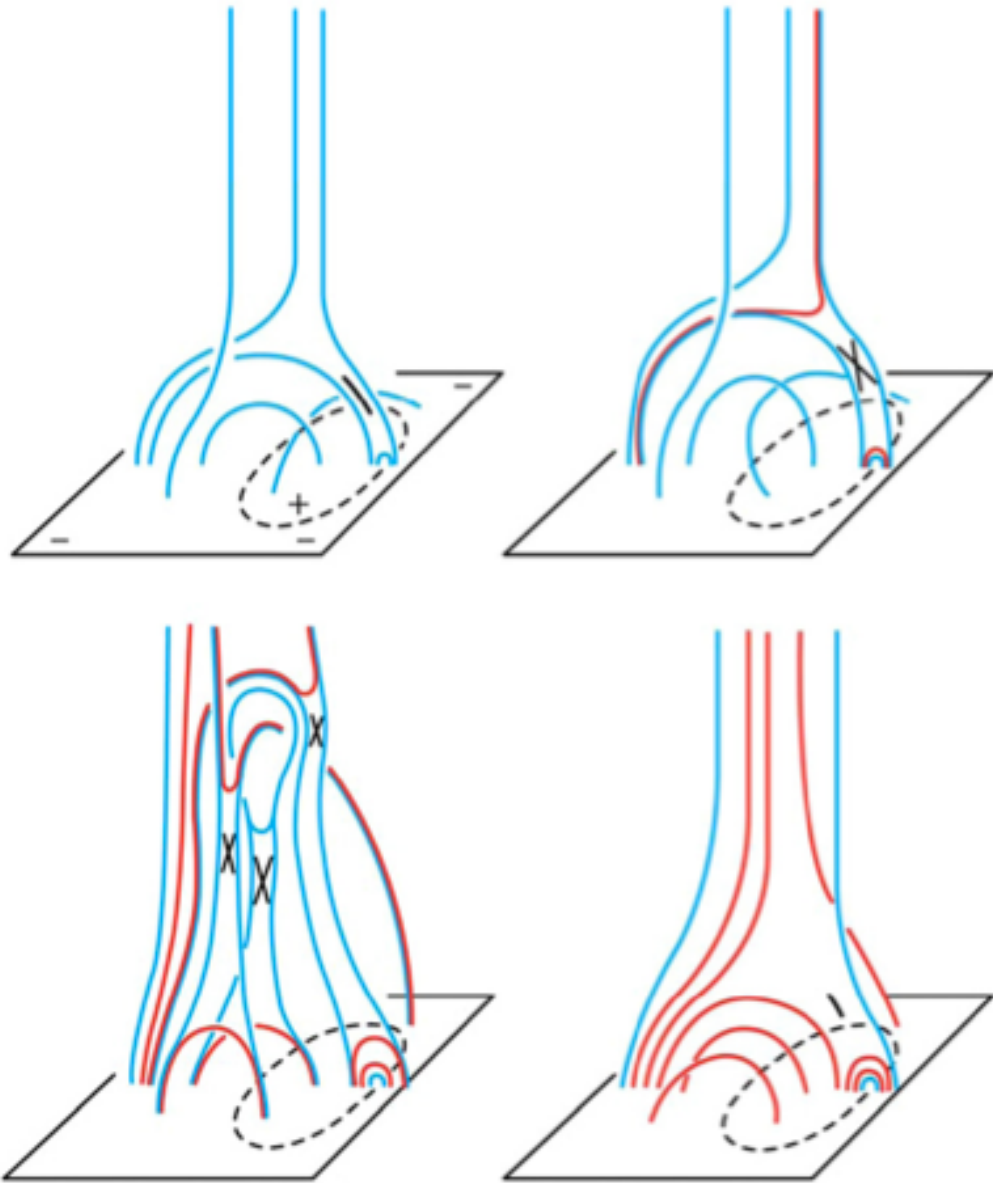


Figure 1.7: Cartoon of the Blowout-jet model (Figure 2 in Moore et al. 2010). Red field lines are those that have been reconnected; these have reconnection-heated X-ray plasma on them. Blue field lines either have not yet been reconnected or will not be reconnected.

### 1.3.2 Acceleration Mechanism of Coronal Jets

Shibata et al. (1992, 1997) proposed different types of independent coronal jets by accelerating drivers ('evaporation jet', 'reconnection jet', and 'twisted jet').

#### Reconnection Jet

A bipolar field is changed to an open field by magnetic reconnection. Thus, the newly opened field has the magnetic tension force. The heated plasma by reconnection is driven by the magnetic tension force of the reconnected fields (like a sling-shot). This jet is called a 'reconnection jet'.

The reconnection outflow by magnetic reconnection is the Alfvén speed (e.g. Aschwanden 2006). So a speed of the reconnection jet is the Alfvén speed ( $V_A = B(4\pi\rho)^{-0.5}$ , where  $B$  is a coronal magnetic strength,  $\rho$  is a mass density of the corona). If  $B=10$  G and  $\rho=10^{-15}$  g cm<sup>-3</sup>, Alfvén speed is 890 km s<sup>-1</sup>.

#### Twisted Jet

The basic idea of a 'twisted jet' is proposed for the astrophysical jets by Uchida & Shibata (1985), and Shibata & Uchida (1985, 1986) extended the model of the twisted macro-spicule. After the reconnection between the twisted loop and the untwisted unipolar field, the shear propagates to the unipolar field and the twisted unipolar field untwists to relax (Figure 1.8). The heated plasma by reconnection is accelerated by  $J \times B$  force upward along untwisted fields. The speed of the twisted jet is the Alfvén speed.

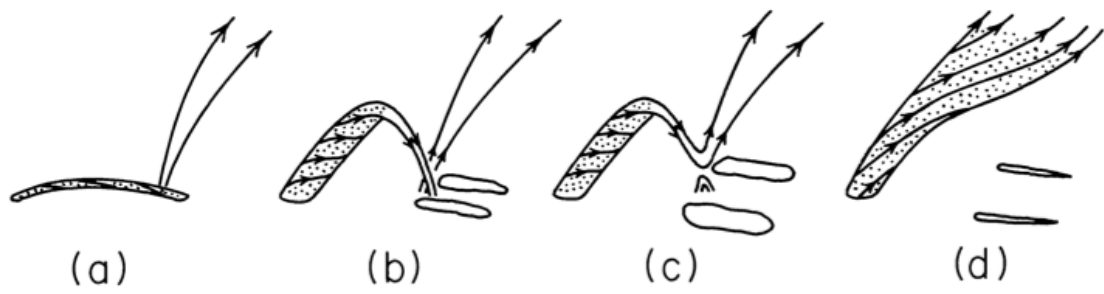


Figure 1.8: Schematic picture illustrating the situation of the filament eruption model (Figures 5a–5d in Shibata & Uchida 1986).

## Evaporation Jet

The energy released by reconnection accelerates non-thermal particle and/or produces thermal conduction. Then the chromospheric plasma around the footpoints is heated. Since the radiative loss rate above 0.1 MK falls toward higher temperature, the chromospheric plasma is quickly heated to above the coronal temperature. Then the pressure is raised by a factor of  $10^2$ - $10^3$ , and the heated plasma rapidly expands. This expanding plasma is called an 'evaporation jet'.

A speed of the evaporation jet is roughly a sound speed ( $C_s = \sqrt{2k_B\gamma T m_p^{-1}}$ , where  $k_B$  is the Boltzmann constant,  $T$  is a temperature,  $m_p$  is a proton mass, and  $\gamma$  is the specific heat ratio). If  $T$  is 1 MK, sound speed is  $165 \text{ km s}^{-1}$ . The upper limit of the chromospheric jet is  $2.35 C_s$  assuming the ratio of the number density of the chromosphere to that of the corona before the flare is  $10^2$  (Fisher et al., 1984).

### 1.3.3 Simulation Results

To understand the time evolution of the jet based on the model, some authors carried out the numerical simulation. In this section, we review these results.

Yokoyama & Shibata (1995, 1996) performed numerical simulation based on the model of X-ray jets by Shibata et al. (1992), by solving resistive magnetohydro dynamics (MHD) equations. The effects of the thermal conduction and the radiative cooling are omitted in their simulation. Two cases are considered for the initial magnetic configuration (the horizontal-coronal-field and the oblique-coronal-field) that corresponds to the two loop-sided jet type and the anemone jet type (Shibata et al., 1994). They succeeded in reproducing an X-ray jet driven by magnetic reconnection. For the oblique-coronal-field case, the reconnection jet is not directly ejected to the oblique field. The high-pressure region is created by the collision of the upward reconnection jet with the oblique field. The final acceleration of the hot jet is due to the gas-pressure gradient from the high-pressure re-

gion behind the MHD shock (Figure 1.9). On the other hand, the downward reconnection jet collides with the top of the reconnected loop, and the loop becomes hot. They can produce both the hot jet and the cool jet by the reconnection. The chromospheric plasma is carried by emerging flux and is ejected by magnetic tension force, which is produced by a whip-like motion.

The 3-D simulation results of Shibata et al. (1992)'s model for the oblique-coronal-field case are reported (Moreno-Insertis et al., 2008). In their simulation, the reconnection happens at the interface between the twisted emerging flux tube and the existing unipolar fields. Moreno-Insertis et al. (2008) showed that a thin, elongated current sheet that embrace the emerged volume like a helmet is thereby formed and reconnection takes place across the current sheet. In their simulation, the position of the jet shift transversely. This is associated with emerging magnetic flux and the corresponding growth of the reconnected-loop to a size similar to the original emerged volume. The speed of this motion is roughly  $10 \text{ km s}^{-1}$  comparable to the observed transverse speed (Savcheva et al. 2007 and Savcheva et al. 2009).

The recent 3-D MHD simulation can reproduce the blowout jet. Moreno-Insertis & Galsgaard (2013) reported a hot and fast coronal jet followed by several violent eruptions in their 3-D MHD simulation based on the model the emergence of a twisted magnetic flux rope from underneath the solar surface into unipolar fields. Archontis & Hood (2013) first reproduce the transition from the standard jet to the blowout jet in the experiment of their 3-D MHD simulation based on the model the twisted emerging flux into unipolar fields. They can reproduce the blowout jet associated with both the cool and hot plasma eruption.

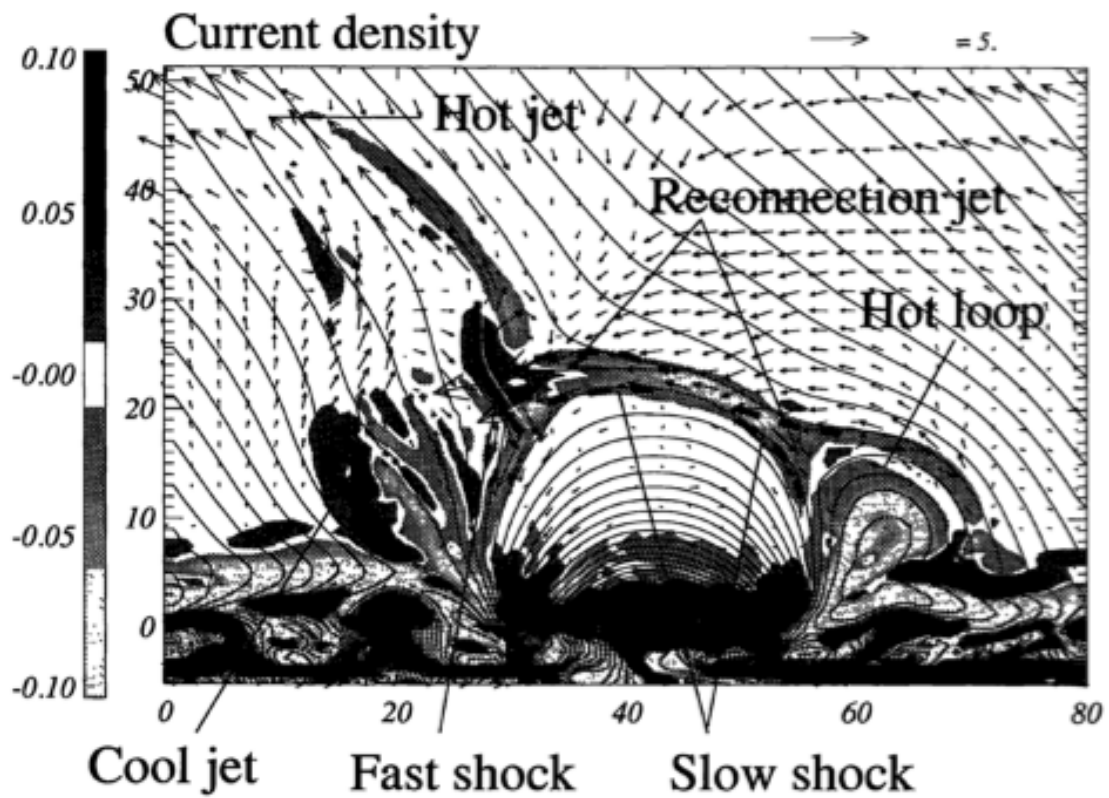


Figure 1.9: Simulation result of the Shibata et al. (1992)'s model for the oblique-coronal field by Yokoyama & Shibata (1996).

Pariat et al. (2009) carried out the 3-D simulation based on their model, and produce the massive, high-speed jets driven by non-linear Alfvén wave. They point out that the kink-like instability caused by the unstable, however this instability does not directly drive the jet. The interchange reconnection of a high twisted closed field with a twisting open field produces the non-linear torsional Alfvén wave. As the waves propagate out their pressure gradients push up the plasma, resulting in the extended jet of upward moving material evident (the lower panel of Figure 1.6). In their simulation result, the speeds of the extended jet fall in the range from 0.65 to 0.9 Alfvén speed. The other simulation extending Pariat et al. (2009) show that the maximum free magnetic energy, which stored at the time when the jet is generated, decreases with the increasing inclination angle of the background coronal magnetic field (Pariat et al. 2010, Dalmasse et al. 2012). So the magnetic structure strongly influences the trigger threshold for the jets.

The above-noted studies perform the MHD simulation without an effect of the thermal conduction onto X-ray jets. So their simulation reproduces only the reconnection jet or the twisted jet. So far, there are two numerical simulations of the jets including the effect of the thermal conduction.

Shimojo et al. (2001) performed 1-D & pseudo 2-D hydrodynamic simulation based on the chromospheric evaporation by microflare in a large coronal loop (radius $\sim 1.7\times 10^5$  km) using the observed parameter by Shimojo & Shibata (2000). They can produce the evaporation jet by the energy input in both cases of a single loop and multiple loops. The physical parameters (for example, temperature and speed) of the evaporation jet in their simulation are similar to those of observed X-ray jet by Shimojo & Shibata (2000).

Miyagoshi & Yokoyama (2003, 2004) performed the 2-D MHD simulation for including the effect of the thermal conduction. This simulation extends the simulation of Yokoyama & Shibata (1996) for the horizontal-coronal-field. They can produce two different types of jets (the evaporation jet and the low-density jet) to exist simultaneously around the emerging flux region, which illustrated in Figure 1.10. They found the evaporation jet is produced by the thermal conduction. The evaporation jet has the high density and low

speed, and the emission measure is large. On the other hand the low-density jet is produced directly by reconnection jet, and the low-density jet has the high speed and the low emission measure. They interpreted that the evaporation jet is probably the observed X-ray jet by *Yohkoh*/SXT considering the contrast of the emission measure. The energy of the evaporation jet is somewhat larger than that of the low-density jet.

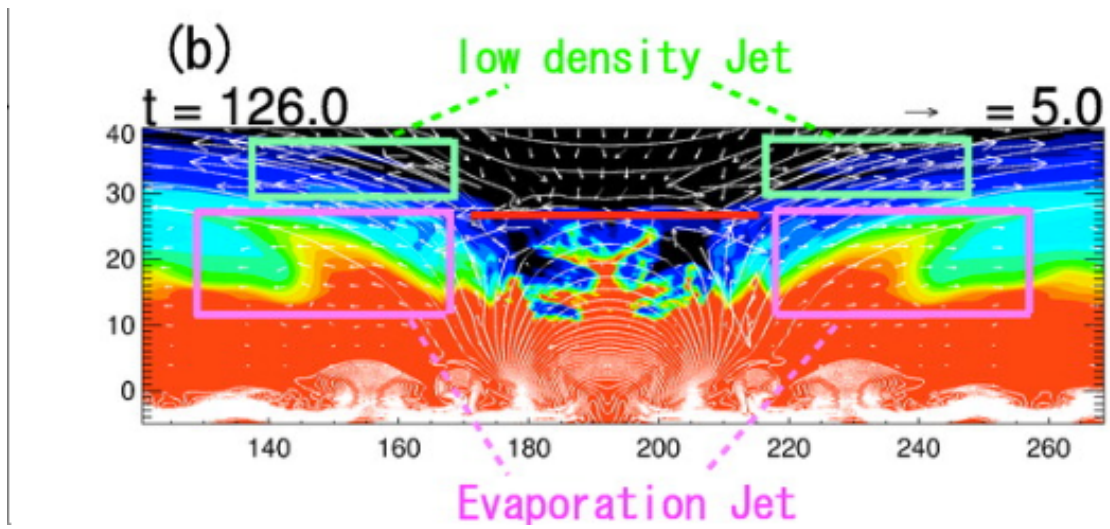


Figure 1.10: The location of two types of jets, evaporation jets and low-density jets by Miyagoshi & Yokoyama (2004). Background color shows the density, and white contour indicates magnetic fields.

## 1.4 Research Subjects in This Thesis

### 1.4.1 Some Unresolved Questions

XRT can observe X-ray jets smaller than the jets observed by *Yohkoh/SXT* in various coronal regions (Chapter 1.2). The studies for X-ray jets not only in ARs but also in QRs and CHs increased using the XRT data. Because statistical properties of X-ray jets in various coronal regions are not understood well, it is not clear what parameters strongly influence on the formation of X-ray jets. On the other hand, XRT also shows that the jet structures are more complex and dynamic than previously known. To understand the mechanism of these structures, we need to know how these jets are accelerated. Because we cannot identify the acceleration mechanism by studying the apparent motion of X-ray jets, the identification of the acceleration mechanisms are not satisfactorily done. In this paper, we have studied mainly about two subjects for X-ray jets.

#### **Regional Difference in X-ray Jets Properties**

From the statistical studies of X-ray jets by *Yohkoh/SXT*, it is known that the number of X-ray jets in ARs is much larger than those in CHs and QRs (Shimojo et al., 1996). If the event number of X-ray jets and the background intensity are good indicators of the coronal activity in these regions, the coronal activities in CHs are low. However, the observation by *Hinode/XRT* shows frequent X-ray jets in polar CHs. Savcheva et al. (2007) found that the jets observed by *Hinode/XRT* appear smaller than the jets observed by *Yohkoh/SXT* because of the instrumental difference. To discuss the event number of X-ray jets in each region extending to smaller jets, we need to use the X-ray images by XRT for statistical studies of X-ray jets. Statistical properties including the event number are not studied well for X-ray jets in ARs, QRs, and CHs used XRT data. Is there regional difference in characteristics of X-ray jets in the corona? To answer the question, we need to know

characteristics of X-ray jets in various coronal regions.

### **Driver of the acceleration of the jet structure**

In Section 1.3.2, we discussed three types of coronal jets accelerated by different forces (evaporation jet, reconnection jet, and twisted jet). The *Hinode*/XRT shows that the jet structures are more complex and dynamic than previously known. To understand the mechanism of the complex and dynamic jet structures, identifying acceleration mechanism is necessary. How do you classify, observationally, jets into three types? One difficulty in the classification of the jets is that there is no realistic simulation that can be used as references. Three-dimensional numerical calculations in previous studies do not take account of the key physical processes to produce both reconnection jets and evaporation jets (thermal conduction, radiative cooling, and gravity are not included). In particular, the thermal conduction is important for producing the evaporation jets (Miyagoshi & Yokoyama 2003, Miyagoshi & Yokoyama 2004).

Some studies try to classify the observed jets into three types by observationally derived parameters (e.g. speed, temperature, and motion of the jet structure). Because the sound speed and the Alfvén speed vary in the corona, the observed jets cannot be distinguished by their speeds alone. There are only two studies for the jet speed connected to the temperature of the jet by spectral analysis (Matsui et al. 2012, Tian et al. 2012) and investigated the relationship between the temperature and the speed of the jets. Shimojo & Shibata (2000) reported that the estimated mass of the jet in ARs is comparable to the theoretical values derived from the balance between conductive flux and enthalpy flux carried by the evaporation jet as evidence for the evaporation jet. In these studies, either the evaporation jet or the reconnection is discussed, but not both. There are few reports for classifying observed jets into these types of the jets observationally.

## 1.4.2 Content of the Thesis

We study about two objects for X-ray jets statistically. The thesis is organized as follows;

### Chapter 2. A Statistical Study of Coronal Active Events in the North Polar Region

Is there a regional difference of characteristics of coronal active events, which include transient brightenings and X-ray jets? In this chapter, we report on our attempt to answer the question by statistically studying the characteristics of transient brightenings and X-ray jets (e.g. occurrence rate, length, lifetime, speed) in the polar CHs, the regions around the boundary of the CHs, the polar QRs, and the equatorial QRs using the X-ray images taken by *Hinode*/XRT during three weeks.

### Chapter 3. A New Scheme for Detecting X-ray Jets in Coronal Holes and Quiet Regions

There are too many X-ray images, taken by *Hinode*/XRT, to be manually handed. To improve the efficiency in using these images for X-ray jet detection, we develop a scheme for automatic detection.

### Chapter 4. A Study of Acceleration Mechanism of X-ray Jets

To investigate observationally the process for driving the jet, we try to classify the observed jets into two types: the evaporation jet and the magnetic-driven jet (reconnection jet and twisted jet). Considering the process of transportation of the released energy by reconnection, we estimate the temperature and speeds of the jets. We compare the estimated parameters with the expected regions of the evaporation jet and the magnetic-driven jet.

### Chapter 5. Summary

In this chapter, we summarize the studies of this thesis.



## **Chapter 2**

# **A Statistical Study of Coronal Active Events in the North Polar Region**

### **2.1 Abstract**

In order to study the relationship between characteristics of polar coronal active events and the magnetic environment in which such events take place, we analyze 526 X-ray jets and 1256 transient brightenings in the polar regions and in regions around the equatorial limbs. We calculate the occurrence rates of these polar coronal active events as function of distance from the boundary of coronal holes, and find that most events in the polar quiet regions occur adjacent to and equatorwards of the coronal hole boundaries, while events in the polar coronal holes occur uniformly within them. Based primarily on the background intensity, we define three categories of regions that produce activity: polar coronal holes, coronal hole boundary regions, and polar quiet regions. We then investigate the properties of the events produced in these regions. We find no significant differences in their characteristics, for example, length and lifetime, but there are differences in the occurrence rates. The mean occurrence rate of X-ray jets around the boundaries of coronal holes is higher than that in the polar quiet regions, equatorial quiet regions, and polar coronal holes. Furthermore, the mean occurrence rate of transient brightenings is also

higher in these regions. We make comparison with the occurrence rates of emerging and canceling magnetic fields in the photosphere reported in previous studies, and find that they do not agree with the occurrence rates of transient brightenings found in this study.

## 2.2 Introduction

Dynamic events are commonly observed in the solar corona, and the frequency of the events is often used as a measure of the level of coronal activity. Observations by Soft X-ray Telescope (SXT: Tsuneta et al. 1991) aboard the *Yohkoh* satellite (Ogawara et al., 1991) revealed that many small flares, named 'transient brightenings', are constantly occurring in the corona. Shimizu et al. (2002) showed that half of these transient brightenings appeared above emerging flux regions, while Kotoku et al. (2007) discussed the possibility that transient brightenings associated with X-ray bright points (XBPs) are related with magnetic flux cancelation. These results suggest that we should consider both flux emergence and cancelation as photospheric counterparts of transient brightenings.

X-ray jets are also commonly observed in the solar corona (Shibata et al., 1992). These jets are characterized by thin elongated structures in X-rays. They are also associated with small flares, and people generally think that this small flare is a kind of a transient brightening. Some authors have reported that X-ray jets occur in photospheric regions where magnetic fields are emerging or canceling (e.g. Canfield et al. 1996, Shimojo et al. 1998, Chifor et al. 2008b, and Huang et al. 2012). The magnetic and morphological evolution of X-ray jets is well explained by MHD simulations and theoretical modeling of magnetic reconnection (e.g. Yokoyama & Shibata 1995, 1996, Nishizuka et al. 2008, and Moreno-Insertis et al. 2008).

Shimojo et al. (1996) carried out a statistical study of 100 X-ray jets observed by *Yohkoh*/SXT, and showed that the frequency of X-ray jets in coronal holes is lower than that in active regions. However, recent X-ray observations have revealed that X-ray jets in polar coronal holes are occurring more frequently than previously thought (Cirtain et al.,

2007). Savcheva et al. (2007) showed that the typical length scale and lifetime of X-ray jets in polar coronal holes were smaller than those reported by Shimojo et al. (1996). It has therefore been suggested that the spatial and temporal resolution of *Yohkoh/SXT* was not enough to detect polar X-ray jets, and that the occurrence rate of X-ray jets in coronal holes was underestimated. Furthermore, recent studies have suggested that jets in coronal holes appear more frequently than in quiet regions, and that this is true not only in coronal holes themselves, but also around their boundaries (Subramanian et al. 2010, Yang et al. 2011).

The relationship between coronal activity in the polar regions and the structure of the magnetic field is not yet well understood. In order to study this relationship, we have identified X-ray jets and transient brightenings in the polar regions (including both coronal holes and quiet Sun), using images taken by X-Ray Telescope (XRT; Golub et al. 2007, Kano et al. 2008) aboard the *Hinode* satellite. We then statistically investigate the characteristics of these X-ray jets and transient brightenings, and examine the regional differences between these phenomena. In Section 2.2, we describe the observations and our detection method. In Section 2.3, we discuss the characteristics of the X-ray jets and transient brightenings and the differences between region.

## **2.3 Observations and Data Analysis**

### **2.3.1 Observations**

In September 2007, the *Hinode* satellite (Kosugi et al., 2007) observed regions around the north pole for three weeks. X-ray images were taken by XRT in the period of September 5 - 22. We obtained 35 sets of observations and the average duration of each observation was about 6 hours. The temporal cadence of the observations was 80 seconds for some datasets and 120 seconds for the others. The XRT plate scale was 1.028 arcsec

pixel<sup>-1</sup>, and the field of view was 1,053 arcsec (E-W) × 395 arcsec (N-S). The exposure time for the observations was 16 seconds.

In order to detect X-ray jets and transient brightenings even if they show only weak X-ray intensity enhancements, we used the thinnest of the XRT filters: Al-poly. The Al-poly filter has extended temperature sensitivity down to plasma at 1 MK (Narukage et al., 2011). To investigate differences in the characteristics of these phenomena around the pole and equator, we also used X-ray images that contained the equatorial limbs within the field of view in September and November of 2007. The total observing time for the data we analyzed is about 66 hours. The spatial and temporal resolution and the XRT filter used for the equatorial limb observations are similar to those of the polar images, but the field of view was 527 arcsec × 527 arcsec and the time cadence was 80 seconds. We calibrated the X-ray intensity and instrument pointing using 'xrt\_prep.pro' and 'xrt\_jitter.pro' in the Solar Software package (SSWidl; Freeland & Handy 1998).

### **2.3.2 Detection**

#### **Detection of X-ray Jets by Visual Inspection**

Most X-ray jets have two prominent structures. The first is that they are thin structures, and this structure elongates over time. The X-ray intensity distribution along the structure also shows an exponential decrease towards the apex (Shibata et al., 1992). The second feature is that brightenings near the base of the thin structure; an XBP or a small loop system, usually exist prior to the event (Shimojo et al., 1996), and they brighten when the thin structure of the jet appears. We call these brightenings 'footpoint flares'. Using the footpoint flares as markers, we define X-ray jets as follows;

- A thin structure, which was not observed before, appears when a footpoint flare initiates and then elongates with time.

- The ratio of the length to the width, of the thin structure, is more than 2 at the maximum elongation.

We visually inspected the datasets to search for events that satisfy both these criteria. Running difference images (see Figure 2.1) were used to detect as many small and short-lived X-ray jets as possible (Savcheva et al., 2007). Applying this method, we successfully detected 844 events around the north polar regions and 55 events in the equatorial quiet regions.

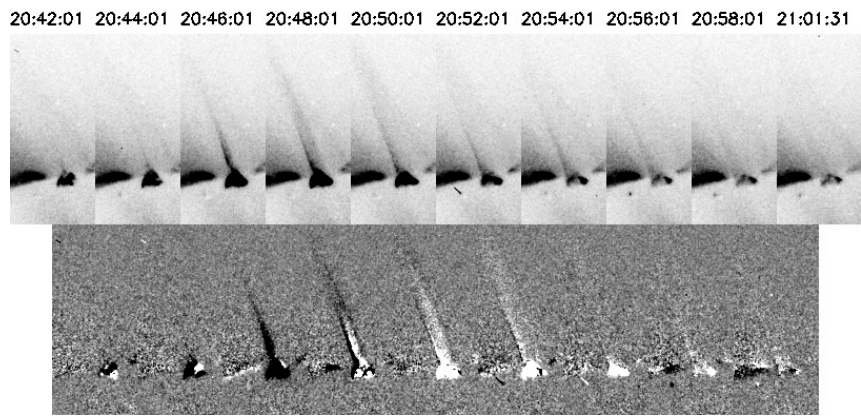


Figure 2.1: An example of a polar X-ray jet. The field of view in each panel is  $82 \text{ arcsec} \times 185 \text{ arcsec}$ . An X-ray jet occurred on 2007 September 5th, near the north pole. Upper panels show X-ray images, while lower panels show running difference images.

## **Automatic Detection of Transient Brightenings**

We also studied another kind of dynamic coronal event: transient brightenings. Schemes to automatically detect transient brightenings have already been developed (e.g. Shimizu 1995, Aschwanden et al. 2000a, Subramanian et al. 2010). We made some improvements to these methods and applied them to our XRT data sets. Our automatic detection scheme is as follows.

### **1) Preparation of Macro-Pixel Images**

To improve the signal-to-noise ratio in the images, we sum the X-ray counts in  $4 \times 4$  pixels to obtain 'macro-pixel' images. We then only use the macro-pixels that are located fully inside the solar X-ray limb. The spatial resolution of these macro-pixel images is 4.098 arcsec.

### **2) Detection of X-ray Enhancement**

To detect the X-ray enhancement in a brightening, we use the temporal intensity profile of the X-ray counts in each macro-pixel. First, we compute the mean count level in each macro-pixel over the observation period (about 6 hours). Then we select counts that are smaller than this average, and assume that they represent the background. We then compute the 'average background level' by averaging the background X-ray counts. Next, we derive the standard deviation of the X-ray count in each macro-pixel. If the enhancement above the average background level exceeds three times the standard deviation, we identify the macro-pixel as a 'candidate pixel' for a transient brightening (see Figure 2.2). By repeating this procedure for the entire dataset, we make a 'candidate map', showing the times and positions of candidate pixels.

Highly energized particles passing through the orbit of *Hinode* sometimes also produce

X-ray enhancements. To eliminate these events, we add two more criteria. The purpose of the first is to exclude events produced by high-energy particles in South Atlantic Anomaly (SAA). When *Hinode* enters SAA, the X-ray count rates increase in many macro-pixels simultaneously (Figure 2.3). We define the SAA period as the period during which more than 3% of all the macro-pixels become 'candidate pixels', and any candidates detected during the SAA period are ignored.

The second criterion is mainly for eliminating cosmic ray events or those coming from the High Latitude Anomaly (HLA). If a candidate macro-pixel does not show the enhancement in three consecutive images, the candidate pixel is not identified as exhibiting a transient brightening.

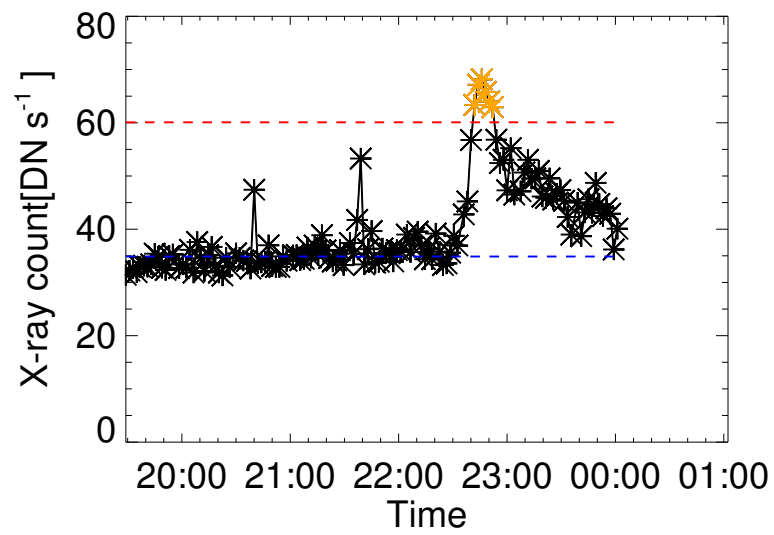


Figure 2.2: A sample time profile of the X-ray counts in a macro-pixel. The red and blue dashed lines indicate three times the standard deviation and the background level, respectively. The orange asterisks show the candidates for transient brightenings.

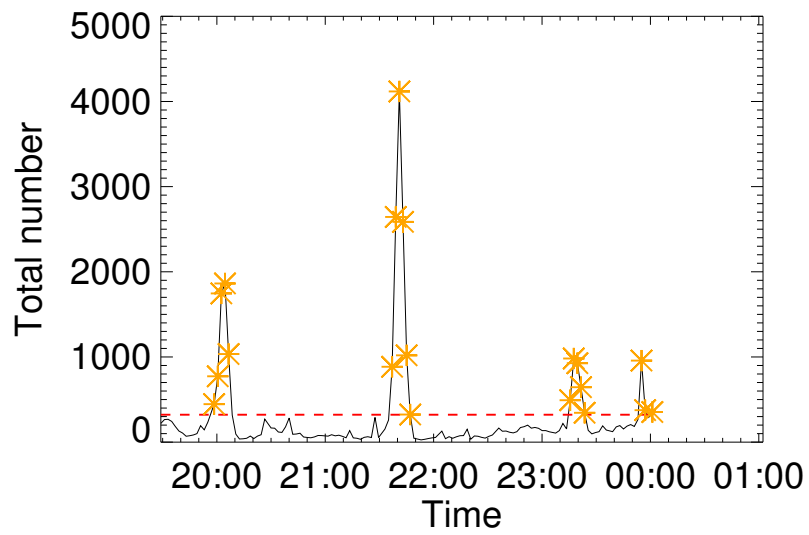


Figure 2.3: The time profile of the total number of candidate pixels in an on-disk macro-pixel. The red dashed line indicates the threshold value for SAA. The orange asterisks show the SAA periods.

### **3) Identification of Transient Brightenings as Single Events**

Occasionally, the size of a transient brightening exceeds the size of the macro-pixel, leading to the X-ray enhancement taking place in more than one macro-pixel. To account for such events, our program identifies these brightenings as one event, provided the candidate pixels are located side by side. We also employ this criterion in the time domain. More precisely, if there are candidates in the same position in successive images, candidates in these pixels are identified as belonging to the same event.

### **4) Categorization of Transient Brightenings as with/without an Associated X-ray Jet**

In order to compare X-ray jets with 'pure' transient brightenings, we categorized them into those that are associated with an X-ray jet and those that are not. Transient brightenings with X-ray jets, which account for 4% of all the transient brightenings, are the ones whose position and timing are consistent with this association.

Under these criteria, we identified 3436 transient brightenings in the north polar regions and 257 in the equatorial quiet regions.

## **2.3.3 Derivation and Estimation of Parameters of Detected Events**

### **Parameters of X-ray Jets**

In this study, we derive and estimate five parameters for the elongated thin structures and three parameters for the footpoint flares. The parameters characterizing the thin structures are length, lifetime, apparent velocity, width, and angle between the direction of elongation and the normal vector of the associated footpoint flare. The derived parameters are values projected on the image plane, of course, since XRT does not have the capability to observe the line of sight components of motion associated with the footpoint flares. For

the footpoint flares, the area, total X-ray intensity, and thermal energy are derived. The length of the thin structures is measured, by visual inspection, between the apex of the structure and the footpoint flare at the time of the maximum of the X-ray counts. The lifetime of an X-ray jet is defined as the time interval between the time of its first appearance and the time of its disappearance. The width is defined as the diameter of the thin structure at its mid-point, when the height of the jet reaches its maximum. The apparent velocity of the X-ray jet is estimated by dividing the maximum length by the time interval between the times of its first appearance and the time it reaches its maximum length. The direction of the X-ray jets is also used for investigating the coronal magnetic fields.

In this study, the normal vector is defined at the center of the footpoint flare for reference. On the other hand, the X-ray jet's direction is defined as a vector starting from the center of the footpoint flare and ending at the apex of the X-ray jet. We measure the angles clockwise from the normal direction to the X-ray jet's direction, projected on the image plane, and use this as one of the parameters characterizing X-ray jets.

The area of a footpoint flare is defined as the area of the rectangle that circumscribes the footpoint flare. In this paper, the limb foreshortening effect is corrected by taking account of the latitude and longitude of the event. The total X-ray intensity of the footpoint flare is obtained by integrating the X-ray counts in the rectangular area at the time of its maximum and subtracting the background level. The background level is determined by the same method that we used for the automatic detection of transient brightenings. For the thermal energy of the footpoint flare, we assume that its temperature is 1 MK. This corresponds to the temperature of the peak of the XRT response curve for the Al-poly filter (Narukage et al., 2011). The depth of the footpoint flaring loop is assumed to be the same as the shorter side of the rectangle. The assumption of the plasma temperature is not entirely justified, but the thermal energy is only proportional to the temperature and therefore this rough estimation should not affect our results significantly.

## **Parameters of Transient Brightenings**

In order to investigate the properties of the transient brightenings in each region, we derive four parameters for the candidate maps: the area, total X-ray intensity, lifetime, and thermal energy. The lifetime of a transient brightening is the duration from first appearance to disappearance of the brightening in the candidate pixels. The total X-ray intensity is the maximum of the integrated X-ray counts over the candidate pixels during the event. The area of the transient brightening is derived from the number of the candidate pixels at the peak time of the total X-ray count. Finally, we estimate the thermal energy of the transient brightening using the same method as applied for the footpoint flares.

## **2.4 Results**

### **2.4.1 Classification of Polar Regions based on X-ray Intensity**

In order to compare the characteristics of X-ray jets and transient brightenings in open and closed magnetic field regions, we first divide the polar regions into coronal holes and quiet regions. By visual inspection of X-ray images, we choose an intensity threshold of  $3.5 \text{ DN s}^{-1} \text{ pixel}^{-1}$  to define the boundaries of the coronal holes (where DN is the data number). A region with an intensity less than the threshold is considered to be a coronal hole in this study (see Figure 2.4). Using this classification scheme, 467 X-ray jets are detected in the polar coronal holes, and 377 are detected in the polar quiet regions. The number of transient brightenings detected in the polar coronal holes reaches 1862 during our observations, and 1564 are detected in the polar quiet regions. All the events detected in regions near the equatorial limb fall into the quiet region classification.

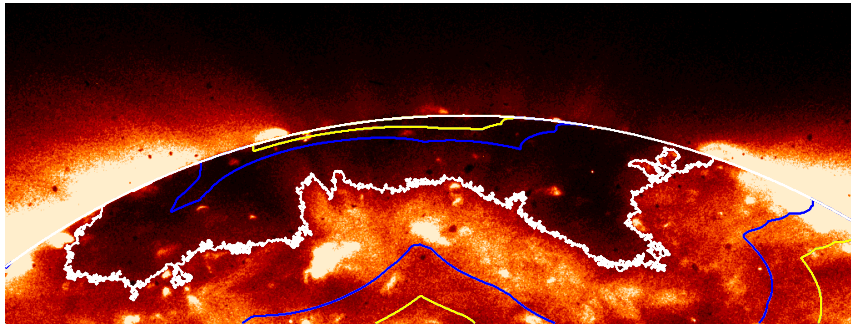


Figure 2.4: An X-ray image on 2007 September 5th around the north pole. The white line shows the boundary of the coronal hole. The boundary between the CHB and the PQR is indicated in the blue line for X-ray jets and the yellow line for transient brightenings

## 2.4.2 Influence of X-ray Background Level on Detection of Events

Because our X-ray jet/transient brightening detection method uses the contrast between the background level and X-ray intensity of the event, the background level could affect the efficiency of the event detection. In particular, we may tend to detect more events in regions with weaker background levels, such as coronal holes. In order to evaluate the influence of the background level on the performance of the detection method, we investigate the X-ray intensity of events in such regions, after subtracting the background level. Figures 2.5 and 2.6 show the frequencies of X-ray jets and transient brightenings plotted against the excess of their X-ray intensities. In Figure 2.5, for the X-ray jets, the excess of the X-ray intensity at the half of the jet's length is used, and in Figure 2.6, for the transient brightenings, the average excess of the X-ray intensity of the brightening is used. The error bars in the figures represent  $\pm 1 \sigma$  uncertainties, assuming a Poisson distribution for the number of events in each bin. Hereafter, the error bars in all the figures indicate  $\pm 1 \sigma$  Poisson errors.

Assuming that the inverse relationship between the frequency and excess of X-ray intensity is valid down to unobservable values, the positions of the peaks of the distributions suggest where the lower limits for a consistent use of our detection method might be. In Figure 2.5, for the X-ray jets, no significant difference in the peak positions is found and they are located at around  $1 \text{ DN s}^{-1} \text{ pixel}^{-1}$ , while for the transient brightenings in Figure 2.6, the peak position in the polar coronal holes is lower than that in the polar and equatorial quiet regions, indicating that the background level is affecting the detection method. To avoid this possible bias due to the background levels, we set lower limits for the sample of events as follows: For X-ray jets, the value of  $1 \text{ DN s}^{-1} \text{ pixel}^{-1}$  is naturally adopted, and for transient brightenings, it is set to  $10 \text{ DN s}^{-1} \text{ pixel}^{-1}$ , which is the peak position in the quiet regions. After rejecting events below these limits, the number of X-ray jets used in this study become 213 in the polar coronal holes, 265 in the polar quiet regions, and 48 in the equatorial quiet regions. The number of transient brighten-

ings became 216 in the polar coronal holes, 958 in the polar quiet regions, and 82 in the equatorial quiet regions.

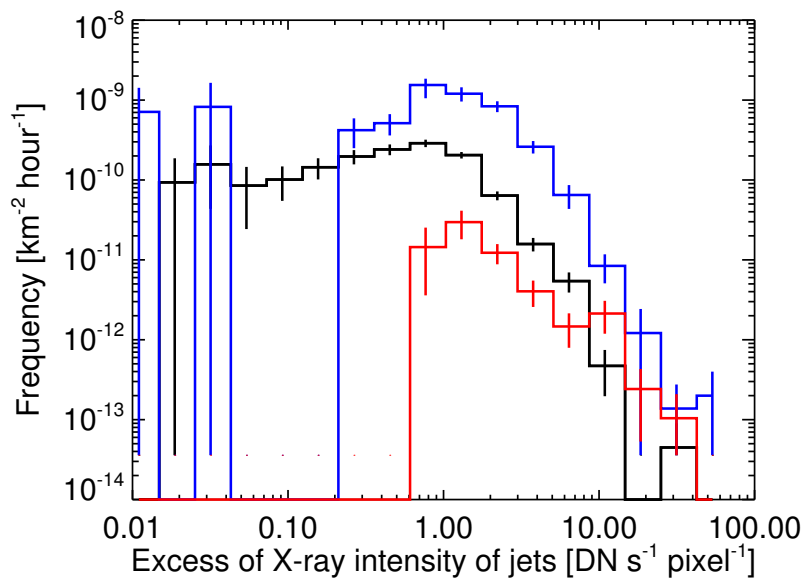


Figure 2.5: The frequency distributions of the X-ray jets: The black, blue, and red lines show X-ray jets occurring in the polar coronal holes, the polar quiet regions, and the equatorial quiet regions, respectively. The horizontal axis indicates the excess of the X-ray intensity of the thin structures and the vertical axis indicates the event number normalized by total area, and duration of the observation.

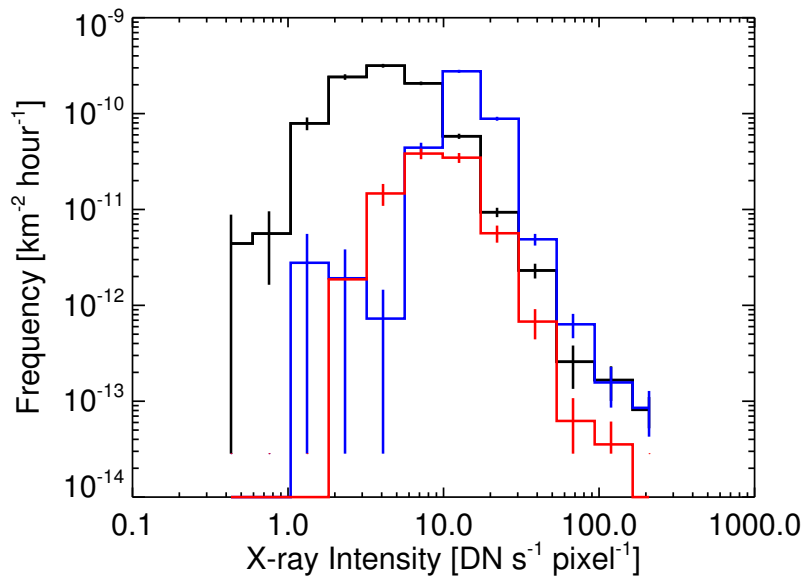


Figure 2.6: The frequency distributions of the transient brightenings: The black, blue and red lines show transient brightenings in the polar coronal holes, the polar quiet regions, and the equatorial quiet regions, respectively.

### 2.4.3 Occurrence Rate as Function of Distance from Coronal Hole Boundary

In order to examine the spatial distribution of the events occurring in each region, we measured their distances from the coronal hole boundaries. We investigated the distribution of the occurrence rate as a function of the distance, that is, the minimum of the distances measured from the locus of the boundary to the event position (Figures 2.7 and 2.8). The occurrence rate is the frequency of the events normalized by the time and area in each distance bin. Figure 2.7 shows that the frequency of X-ray jets is uniformly distributed in the polar coronal holes between the distance of  $2 \times 10^4$  km and  $2 \times 10^5$  km, and decreases from a distance of  $2 \times 10^5$  km. The uncertainty of the distribution becomes large above  $2 \times 10^5$  km, because the observed areas, being close to the north pole, are very small. We found that the occurrence rates of X-ray jets in the polar quiet regions starts to decrease rapidly at a distance of  $10^5$  km, and this cannot wholly be attributed to the observational uncertainties. Therefore, most of the X-ray jets in the polar quiet regions are concentrated within  $10^5$  km of the boundary. Note that there is a dip in the 0 to  $+3 \times 10^4$  km distance bin. We have carefully checked our analysis method and found that it is a real feature. It probably reflects a difference in the physical environment just at the vicinity of the regions around the boundary of the coronal holes. We have, however, no simple explanation for this observation.

Figure 2.8 shows the distribution of transient brightenings as a function of the distance from the boundaries of the coronal holes. The distribution in the polar coronal holes is roughly uniform within a distance of  $2 \times 10^5$  km. We also find that most of the transient brightenings in the polar quiet regions occur adjacent to and equatorwards of the boundaries of the coronal holes. While the other properties are similar to those of the X-ray jets, the largest distance where the occurrence rates are high is somewhat larger in the polar quiet regions, and is estimated to be  $1.5 \times 10^5$  km.

We also find some differences in the occurrence rates of the X-ray jets and transient

brightenings in Figures 2.7 and 2.8. The ratio of the mean occurrence rate of the X-ray jets in the polar quiet regions to that in the polar coronal holes is about 2, while the same ratio for the transient brightenings is about 6. In coronal holes, a single magnetic polarity is dominant, and large-scale coronal loops may be created more often than they are in quiet regions with mixed polarities. Magnetic reconnection could tend to take place more often in large-scale coronal loops and produce X-ray jets.

To investigate the characteristics of X-ray jets and transient brightenings near the boundaries of coronal holes, we classify the polar areas into three regions. The 'polar coronal hole (PCH)' is defined as the region where the X-ray intensity is lower than  $3.5 \text{ DN s}^{-1} \text{ pixel}^{-1}$ . The 'coronal hole boundary region (CHB)' is defined as the region where the X-ray intensity is higher than  $3.5 \text{ DN s}^{-1} \text{ pixel}^{-1}$  and the distance to the boundaries of the coronal holes is less than  $10^5 \text{ km}$  for X-ray jets and  $1.5 \times 10^5 \text{ km}$  for transient brightenings, and the 'polar quiet region (PQR)' is defined as the region where the X-ray intensity is greater than  $3.5 \text{ DN s}^{-1} \text{ pixel}^{-1}$  and the distance to the boundaries of the coronal holes is more than  $10^5 \text{ km}$  for X-ray jets and  $1.5 \times 10^5 \text{ km}$  for transient brightenings. Based on these classifications, the number of X-ray jets in these three regions is 213 in the PCHs, 240 in the CHBs, and 25 in the PQRs. Also, the number of transient brightenings is 216 in the PCHs, 934 in the CHBs, and 24 in the PQRs. The sum of the events in the PCHs, CHBs, and PQRs is equal to the number of events in the complete sample in the polar region.

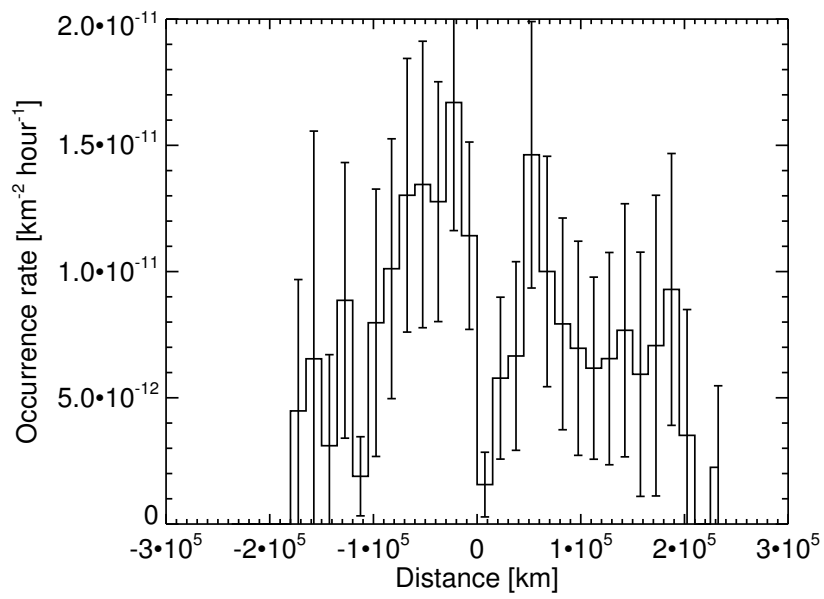


Figure 2.7: The occurrence rates of the X-ray jets as function of distance from the boundary of coronal holes. Zero is the position of the boundary of coronal holes. Negative values of distances indicate a location in the polar quiet regions, and positive values indicate a location in the polar coronal holes.

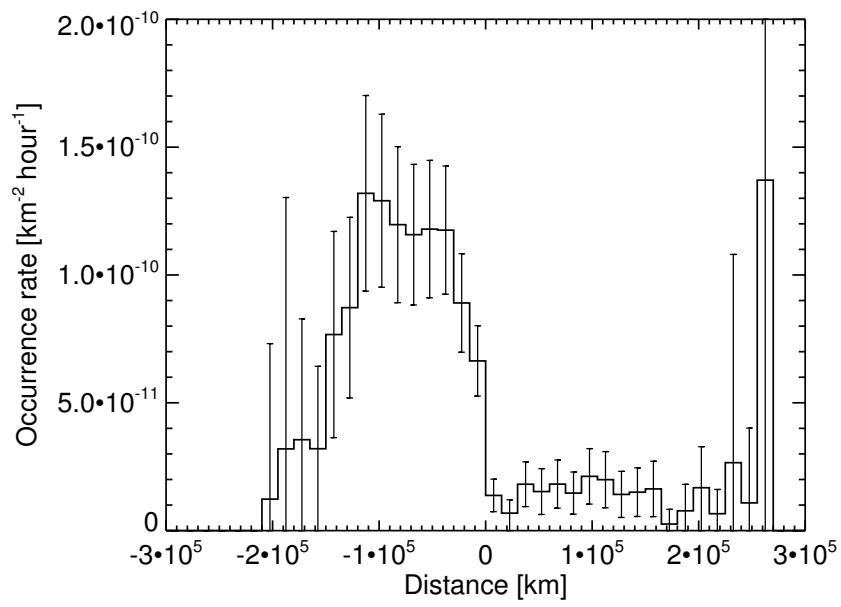


Figure 2.8: As Figure 2.7, but for the transient brightenings.

#### **2.4.4 Daily Occurrence Rate of X-ray Jets and Transient Brightenings**

In order to study differences between the X-ray jets and transient brightenings that depend on the region observed, we compared the characteristics of these phenomena in the PCHs, CHBs, and PQRs. First, we compared the daily occurrence rates of these phenomena in each region.

Figure 2.9 shows the temporal variation of the daily occurrence rates of the X-ray jets in each region. The daily occurrence rate is the number of the events per day normalized by the area and the total observing time. The amount of variation is such that, in each region, the ratio of the maximum to the minimum is 3 to 8. The mean occurrence rate of the X-ray jets in the CHBs is 2 to 3 times larger than that in the PCHs, PQRs, and the 'equatorial quiet region' (EQR) (Table 2.1).

The temporal variation of the daily occurrence rates of the transient brightenings is shown in Figure 2.10. When we calculate the mean occurrence rate of the transient brightenings in the PQRs, we exclude the September 16 data because the area of the PQRs on that date is an order of magnitude less than the area on the other days. The mean daily occurrence rate of the transient brightenings in the CHBs is 8 times more than that in the PCHs and 3 times more than that in the PQRs and EQRs (Table 2.1).

The period of our observational data covers half of the rotation period around the pole. The daily occurrence rates of the X-ray jets and transient brightenings in each region vary within the error bars. This result shows that these events do not have a longitudinal dependence.

Table 2.1: The daily occurrence rates of X-ray jets and transient brightenings

	PCH	CHB	PQR	EQR
X-ray jets	6.84	12.5	4.80	4.52
( $10^{-12}$ km $^{-2}$ hour $^{-1}$ )	$\pm 0.54$	$\pm 0.89$	$\pm 1.09$	$\pm 0.74$
Transient brightenings	1.64	11.4	4.33	4.11
( $10^{-11}$ km $^{-2}$ hour $^{-1}$ )	$\pm 0.12$	$\pm 0.42$	$\pm 1.15$	$\pm 0.52$

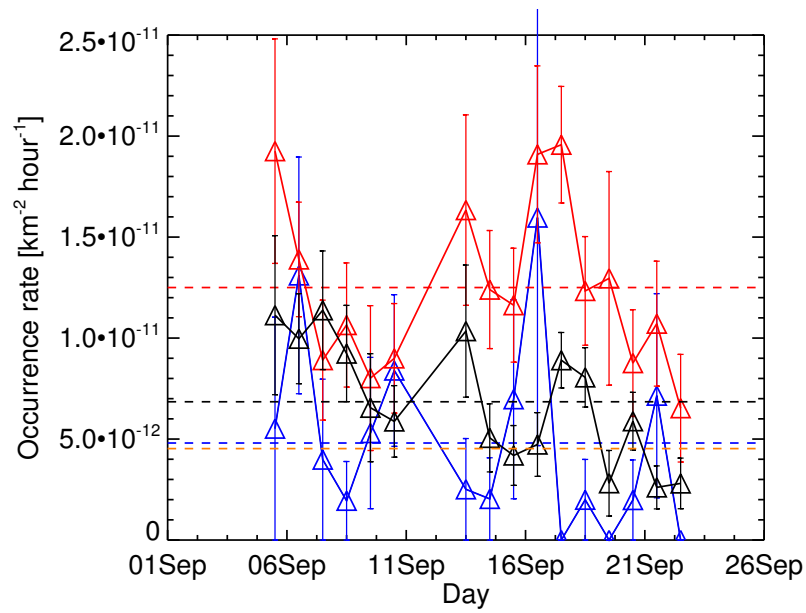


Figure 2.9: Temporal variations of daily occurrence rates of X-ray jets. The triangles joined by the solid lines are daily occurrence rates, while horizontal dashed lines are the mean values. The black, red, blue, and orange show the rates in the PCHs, CHBs, PQRs, and EQRs, respectively.

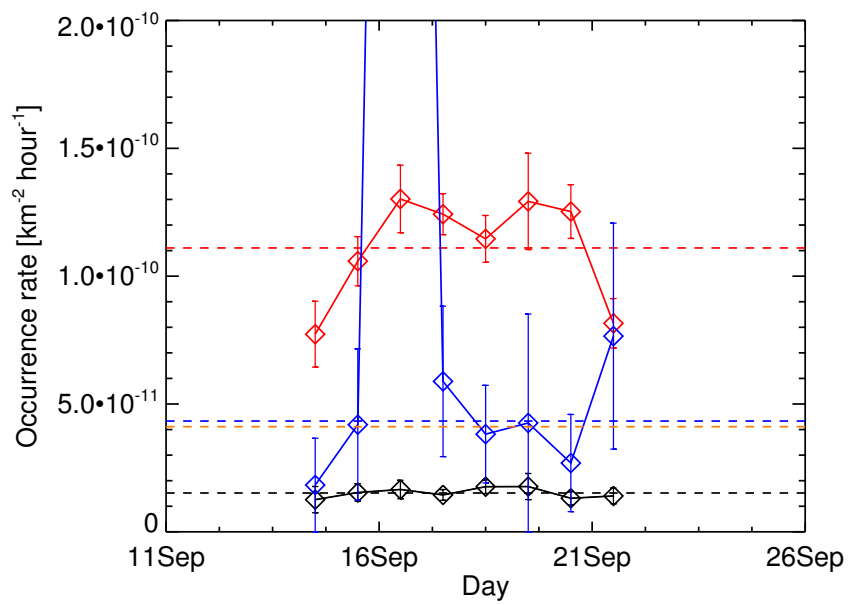


Figure 2.10: Temporal variations of daily occurrence rates of transient brightenings (diamonds). The dashed lines are mean values. The black, red, blue, and orange solid lines show distributions of transient brightenings in the PCHs, CHBs, PQRs, and EQRs, respectively.

### **2.4.5 Parameters of X-ray jets and transient brightenings**

Tables 2.2 and 2.3 summarize our measured physical parameters, for example, the length and lifetime for the X-ray jets and transient brightenings, respectively. No significant differences exist between the regions producing the transient activity. Our results are also consistent with those reported by Savcheva et al. (2007).

Table 2.2: The X-ray jets parameters

		PCH	CHB	PQR	EQR
Length ( $10^4$ km)	Mean	2.63	2.96	2.84	2.64
	Range	0.44-16.2	0.62-9.19	0.76-10.8	0.56-9.72
Lifetime (minute)	Mean	10	11	10	8
	Range	3-45	3-38	3-27	3-33
Velocity ( $\text{km s}^{-1}$ )	Mean	181	173	164	177
	Range	23-811	30-615	43-611	15-538
Width ( $10^3$ km)	Mean	4.07	4.42	4.15	3.54
	Range	0.76-13.1	0.76-12.7	1.52-12.2	1.52-7.76
Area ( $10^7$ $\text{km}^2$ )	Mean	3.26	3.79	3.36	2.47
	Range	0.92-16.6	0.46-27.8	0.92-11.1	0.92-6.95
Thermal energy ( $10^{25}$ erg)	Mean	7.27	8.72	6.13	8.29
	Range	0.36-65.5	0.30-185	0.71-30.6	0.59-58.8

Table 2.3: The transient brightenings parameters

		PCH	CHB	PQR	EQR
Lifetime (minute)	Mean	5	5	5	4
	Range	4-12	4-15	4-12	4-10
Area ( $10^7$ km <sup>2</sup> )	Mean	2.61	2.35	1.81	2.04
	Range	0.92-13.9	0.92-25.9	0.92-4.63	0.92-12.0
Thermal energy ( $10^{25}$ erg)	Mean	9.06	7.47	4.20	6.37
	Range	1.14-228	1.13-193	1.16-19.3	1.38-89.7

## 2.4.6 Frequency Distributions as Function of X-ray Intensity in Footpoint Flares

Figure 2.11 shows frequency distributions of the footpoint flares that are associated with X-ray jets. The power-law indices of the distributions are  $-1.78 \pm 0.17$  (PCHs),  $-1.75 \pm 0.13$  (CHBs), and  $-1.13 \pm 0.09$  (EQRs). Because only 25 X-ray jet events are detected in the PQRs, we cannot derive the power-law index for that region. The distributions in the PCHs and CHBs have indices steeper than that in the EQRs. Shimojo et al. (1996) showed that the power-law index of footpoint flares associated with X-ray jets is  $-1.2$ . In their study, about 70% of their samples are X-ray jets that occurred in active regions. The indices in quiet regions are therefore closer to those in active regions, rather than in PCHs and CHBs.

The frequency distributions for the transient brightenings are shown in Figure 2.12. The power-law indices are  $-2.12 \pm 0.17$  (PCHs),  $-2.03 \pm 0.07$  (CHBs), and  $-1.92 \pm 0.08$  (EQRs). We cannot derive the index for the PQRs because only 24 transient brightenings were detected there. The power-law indices are consistent with each other; the differences being within the error bars. Shimizu (1995) reported that the power-law index of transient brightenings in active regions is  $-1.4$ , and Aschwanden & Parnell (2002) reported that the power-law index of transient brightenings in equatorial quiet regions is  $-1.74 \pm 0.08$ . The power-law index in active regions is therefore flatter than that for other coronal regions.

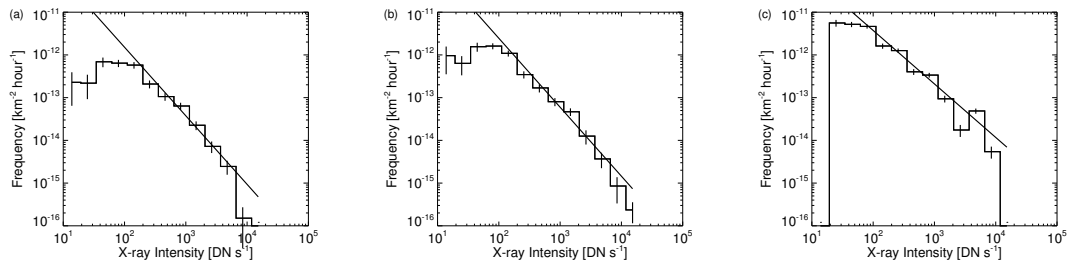


Figure 2.11: The frequency distributions as function of the X-ray intensity of footpoint flares. The panels from (a) to (c) show frequency distributions in the PCHs, CHBs, and EQRs. The solid lines show least-square fits. Vertical axes indicate the X-ray intensity of footpoint flares normalized the exposure time, total area, and the duration of the observation.

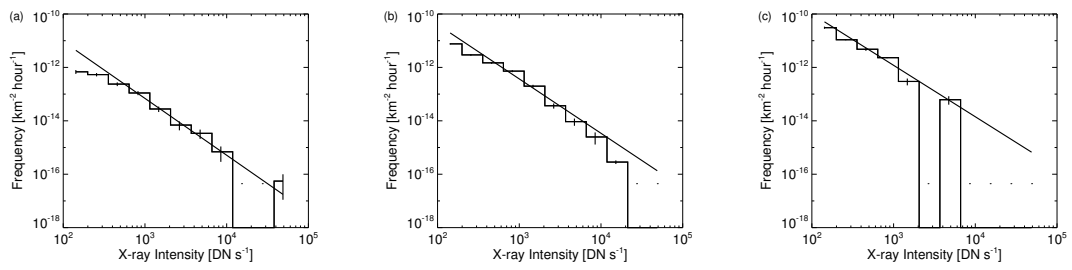


Figure 2.12: As Figure 2.11, but for transient brightenings.

### 2.4.7 Direction of X-ray Jets

Hot plasma, created in an X-ray jet, flows along the coronal magnetic field. We can therefore investigate the structure of the polar magnetic fields from the X-ray jet's flow direction. Figure 2.13 shows histograms of the absolute values of the angle from the direction of the X-ray jets to the normal direction at the center of the footpoint flares. Most of the X-ray jets in the PCHs flow along the normal direction of the solar surface. This suggests that magnetic fields in PCHs are mostly radial. On the other hand, the erupting angles of the X-ray jets in the PQRs and EQRs are rather uniformly distributed. These distributions indicate that magnetic elements are randomly oriented in quiet regions, in which closed magnetic fields would be preferentially created. Finally, the distribution in the CHBs has a peak around 20 degrees. The peak may indicate that magnetic fields in CHBs have super radial structures, or a converging structure toward the pole. Figure 2.14 is a scatter diagram of the horizontal (East-West) coordinates of the footpoint flares and the clockwise angles from the surface normal vector to the directions of the X-ray jets. If magnetic fields in CHBs have a super radial structure, most of the data points will be distributed in the 2nd and 4th quadrants of the diagram. If most of the data points are distributed in the 1st and the 3rd quadrants, it would mean that magnetic fields tend to converge toward the pole. Figure 2.14 show that 71% of the data points are distributed in the 2nd and 4th quadrants. We can therefore conclude that the magnetic fields in CHBs have a super radial structure.

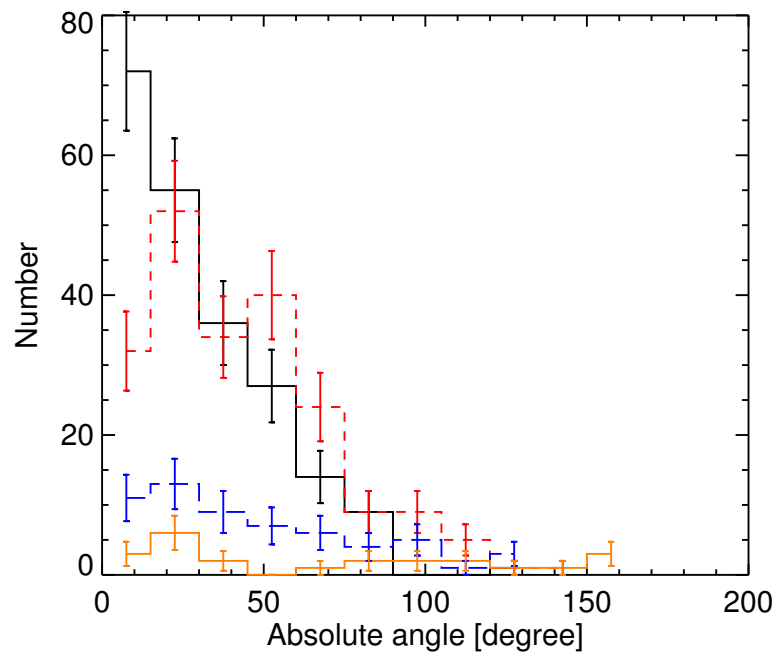


Figure 2.13: The histograms of the absolute angles between the direction of the X-ray jets and the normal directions of the footprint flares: The black solid, red dashed, blue long dashed, and orange solid lines are for the X-ray jets observed in the PCHs, CHBs, PQRs, and EQRs, respectively.

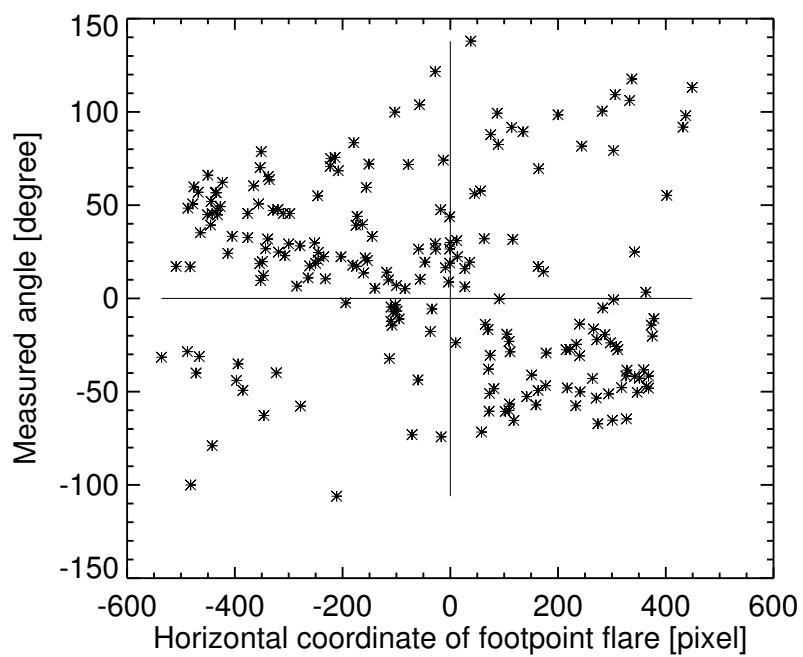


Figure 2.14: The scatter diagram of the horizontal (East-West) coordinates of footpoint flares and the clockwise-measured angles from the surface normal vector to the directions of X-ray jets.

## 2.5 Summary and Discussion

We detected X-ray jets and transient brightenings around the north pole and in quiet regions near the equatorial limbs. We carried out a statistical study of these events associating them with regions in the PCHs, CHBs, PQRs, and EQRs. We found the following results.

1. We detected 844 X-ray jets by visual inspection and 3553 transient brightenings using an automatic detection method around the north pole. Furthermore, we detected 55 X-ray jets and 258 transient brightenings in equatorial quiet regions near the limbs. Different thresholds for the excess of X-ray intensities were set for the X-ray jets and transient brightenings. We therefore selected 478 X-ray jets and 1174 transient brightenings around the north pole for analysis. We have also selected 48 X-ray jets and 82 transient brightenings in the equatorial quiet regions near the limbs.
2. We investigated the occurrence rates of the X-ray jets and transient brightenings in the polar regions as function of distance from the boundaries of coronal holes. These rates show that coronal active events in the polar coronal holes occur uniformly in space, while most of the coronal activity in the polar quiet regions occurs adjacent to and equatorwards of the boundaries of the coronal holes.
3. The mean occurrence rate of X-ray jets in the CHBs is 2 to 3 times higher than that in the PCHs, PQRs, and EQRs. The mean occurrence rate of transient brightenings in the CHBs is 8 times higher than that in the PCHs, PQRs, and EQRs.
4. No large differences in the measured physical parameters (e.g. length, lifetime) are found for both the X-ray jets and transient brightenings in the PCHs, CHBs, PQRs, and EQRs. The mean parameters for X-ray jets are as follows; the length is  $2.7 \times 10^4$  km, the lifetime is 10 minute, the velocity is  $170 \text{ km s}^{-1}$ , the width is  $4 \times 10^3$  km, the area is  $3.5 \times 10^7 \text{ km}^2$ , and the thermal energy is  $7 \times 10^{25}$  erg. The parameters for

transient brightenings are as follows; the lifetime is 5 minute, the area is  $3.0 \times 10^7$  km<sup>2</sup>, and the thermal energy is  $8 \times 10^{25}$  erg.

5. The distribution of the directions of the X-ray jets suggests: 1) Magnetic fields are almost radial in PCHs. 2) Magnetic fields in CHBs have a super radial structure, and 3) Closed loops in PQRs are rather randomly oriented.

Based on these results, we discuss the acceleration of the fast solar wind and the difference in occurrence rates of events among the polar regions in the following subsections.

### **2.5.1 Fast Solar Wind Acceleration by X-ray Jets in PCHs**

Polar coronal holes (PCHs) are thought to be the source region of the fast solar wind and we have also found that these regions frequently produce energetic X-ray jets. Cirrain et al. (2007) pointed out that polar X-ray jets may contribute to the fast solar wind, because there are so many of them. Additionally the apparent velocity of the outflows is very high. Furthermore, the unsigned angle distribution of the PCHs in Figure 2.13 shows that most X-ray jets in the PCHs erupted along open field. These facts suggest that X-ray jets in open field regions in PCHs may contribute to the acceleration of the fast wind.

We have estimated the thermal energy content in a thin X-ray jet structure. Our estimation is based on the results of Shimojo & Shibata (2000), who derived the temperatures and densities of X-ray jets that occurred in active regions using filter ratio analysis. The thermal energy of a typical footpoint flare was estimated by Shimojo & Shibata (2000) to be four to seven times as large as that of the thin structure. The thermal energy of the thin structure is on average three times larger than the kinetic energy. Therefore, we assume that the thermal energy of the thin structure is 1/4 of that in the footpoint flare and the kinetic energy of the thin structure is 1/12 of that of the footpoint flare. Using these estimates, we derive the total energy released by the occurrence of X-ray jets in the PCHs, as the sum of the estimated thermal and kinetic energies of the thin structures. In this study, the thermal energy of a footpoint flare is measured at the time of its peak intensity. The

time of the peak intensity in the footpoint flare, in most X-ray jets, is roughly consistent with the time when the X-ray jet's length is at its maximum. So our estimation of the energy released by X-ray jets is at the time of the maximum length.

From Figure 2.15, the distribution of the energy released by X-ray jets in the PCHs is a power-law with an index of  $-1.79 \pm 0.12$ , which is flatter than  $-2$ . If this distribution and power-law index remains valid between  $10^{22}$  erg (nanoflare) and  $10^{27}$  erg, we can derive  $10^3 \text{ erg cm}^{-2} \text{ s}^{-1}$  as the upper limit of the total energy supplied by X-ray jets in the PCHs. Wang et al. (1996) estimated the energy flux of the solar wind to be more than  $10^5 \text{ erg cm}^{-2} \text{ s}^{-1}$ . Even if X-ray jets directly become solar wind outflow, our PCH's value suggests that they are not sufficiently energetic to explain the fast wind.

Neugebauer (2012) proposed that polar X-ray jets are the sources of microstream peaks in the fast solar wind. Microstream peaks exhibit velocity fluctuations of  $\pm 35 \text{ km s}^{-1}$ . Fluctuations of the energy flux by these velocity variations are estimated to be lower than 1% of the total energy flux, i.e.  $10^3 \text{ erg cm}^{-2} \text{ s}^{-1}$ , as kinetic energy is thought to dominate the total energy flux of the fast solar wind. Polar X-ray jets therefore can supply sufficient energy to produce these velocity fluctuations in microstream peaks.

Shimojo & Shibata (2000) did not include the contribution of waves and Alfvénic flows in PCHs later discovered by Cirtain et al. (2007). We could not detect any evidence of waves or Alfvén flows because of the poor time cadence of our observations. However, reconnection models of X-ray jets suggest that the thermal energy of a footpoint flare is the dominant source of the energy provided to the entire X-ray jet, and the thin structure contains only a quarter of the total energy. Therefore, the contribution by waves and flows could be far less than these values.

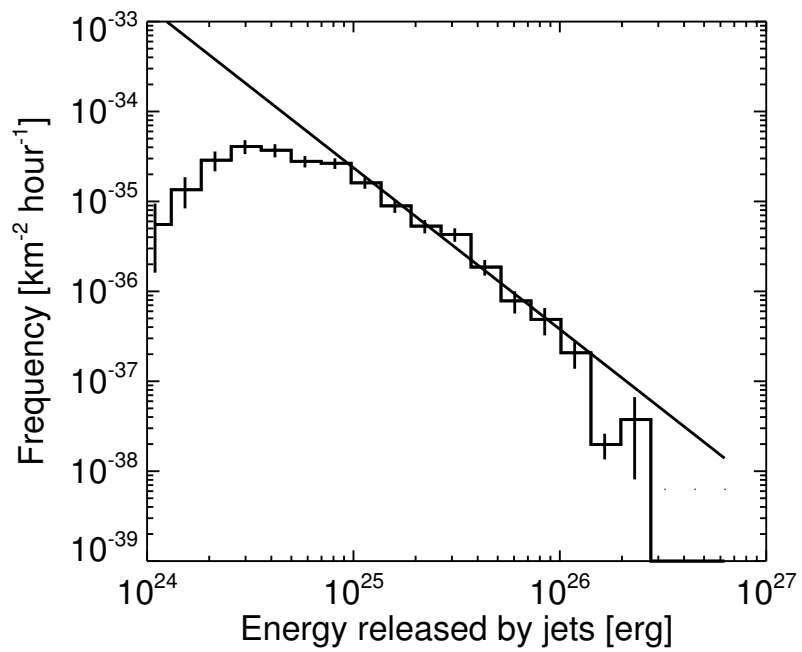


Figure 2.15: The frequency distribution as function of the energy release by the occurrence of X-ray jets in the PCHs.

## 2.5.2 Difference in Occurrence Rates of Transient Brightenings between the Regions

The mean occurrence rate of transient brightenings in the CHBs has been found to be higher than that in the PCHs, PQRs, and EQRs. Following previous studies (e.g. Shimizu et al. 2002, Huang et al. 2012) on the relationship between transient brightenings and emerging or cancelling flux, we tried to estimate the occurrence rates of transient brightenings from those of flux emergence or cancellation events.

Iida et al. (2012) showed that the occurrence rate of flux emergence events was  $1.2 \times 10^{-10} \text{ km}^{-2} \text{ hour}^{-1}$  and that of flux cancellation events was  $3.5 \times 10^{-9} \text{ km}^{-2} \text{ hour}^{-1}$  in quiet regions. A few papers (Zhang et al. 2006, Abramenko et al. 2006, Hagenaar et al. 2008) reported that the occurrence rate of flux emergence events in coronal holes was less than half of that in quiet regions. Based on these results, we estimate the ratios of occurrence rates in the photosphere as follows; flux emergence in coronal holes : flux emergence in quiet regions : flux cancellation in quiet regions = 1 : 2 : 60. Note, however, that we actually need the rate of flux emergence to the height of the corona, not the photosphere, because transient brightenings occur in the corona. Some authors (e.g. Martínez González & Bellot Rubio 2009, Wiegmann et al. 2010) have tried to evaluate the rate of events that reach the corona. However, their investigations were limited to quiet regions. Assuming that the difference in this rate is not significant between regions, our estimate for the ratios of the flux emergence/cancellation rates in the photosphere could also be applied to the coronal ratios.

The likelihood that magnetic fields will be involved in the coronal interaction may depend on the magnetic configuration in each coronal region. In PCHs, a single magnetic polarity is dominant except during solar maximum. Therefore, most of the open fields have the same polarity and closed loops rarely reach the corona, except by flux emergence (Shimojo & Tsuneta, 2009). Assuming this is the case, we can infer that transient brightenings in PCHs are caused only by flux emergence. On the other hand, quiet regions

are filled with magnetic loops, and the polarity of the magnetic fields is balanced. Therefore, transient brightenings in PQRs and EQRs may be caused by magnetic interactions between emerging flux and existing coronal loops, or between two coronal loops that are identified as cancelling flux.

The magnetic environment in CHBs is not well known. However, we speculate that CHBs may have intermediate properties between coronal holes and quiet regions. Let us assume, therefore, that the situation with transient brightenings in CHBs is a mixture of those in PCHs and in PQRs/EQRs.

With these assumptions, however, the ratios of the occurrence rates of transient brightenings in the regions would be the PCHs : CHBs : PQRs (EQRs) = 1 : 31.5 : 62, if the entire CHB area is equally divided between CH-like areas and QR-like areas. This is not consistent with our results, in which the occurrence rate in the CHBs exceeds the PQRs/EQRs rates.

It is interesting to note that the region with enhanced X-ray jet and transient brightening activity extends equatorward of the boundary beyond a distance of  $10^5$  km, although no contribution from active regions was recognized in the northern hemisphere as solar activity was very low in September, 2007. A possible scenario is that transient brightenings in CHBs are enhanced by interchange reconnection. Kahler et al. (2010) introduced a model suggesting that interchange reconnection could operate to maintain the quasi-rigid rotation of the boundaries of coronal holes against eastward photospheric convective motions. Fisk (2003) originally proposed the idea of interchange reconnection around the boundaries of coronal holes as results of photospheric convective motions. These models present magnetic reconnection around the boundaries of coronal holes as a result of cancelling flux in CHBs, but they cannot explain our result that extended CHB regions enhance the occurrence of X-ray jets and transient brightenings.

One possibility is that our assumption that the rate of flux emergence to significant heights is uniform all over the solar surface may be too simplistic. A more detailed understanding of magnetic evolution from below the photosphere to high up in the corona

is needed. Shimojo & Tsuneta (2009) presented the relationship between flux emergence and X-ray jets in the polar coronal hole with only a very limited dataset. We need further detailed statistical studies using more comprehensive datasets to clarify the relationship between activity in the corona and magnetic fields in the photosphere.

# Chapter 3

## A New Scheme for Detecting X-ray Jets in Coronal Holes and Quiet Regions

### 3.1 Abstract

We propose a new scheme for detecting X-ray jets in coronal holes and quiet regions using X-ray images obtained by X-ray Telescope aboard the *Hinode* satellite. The scheme is divided into two main processes. In the first process, we identify active events by X-ray enhancements they exhibit, and reconstruct narrow continuous structures. In the second process, the X-ray jets are selected from the active events based on expected characteristics of X-ray jets.

To evaluate performance of our scheme, we have applied our scheme to X-ray images that include quiet regions and coronal holes. We have found that 70% of the selected active events in coronal holes by our scheme are X-ray jets, and are isolated from neighboring events. On the other hand, the rate in the quiet regions is less than 30%. The poor rate is mainly caused by co-temporal brightenings in neighboring regions. Of the X-ray jets detected by visual inspection, 60% in the coronal holes and 25% in the quiet regions can be detected by our scheme.

We can obtain a large number of X-ray jets by our scheme using a lot XRT data automat-

ically. As by-products, the new scheme outputs the shape and its time evolution of each X-ray jet. So we can easily derive the parameters of jets as function of time and jet-height for a large number of X-ray jets. So our procedure can support studies for not only time-averaged properties of X-ray jets but also the time evolution of X-ray jets (e.g. untwisted motion, multiple-jet structures).

## 3.2 Introduction

X-ray jets are coronal active events discovered from the X-ray images taken by Soft X-ray Telescope (SXT) aboard the *Yohkoh* satellite (Shibata et al. 1992). An X-ray jet comprises two components seen in X-ray images. One is 'jet structure', a narrow strip that elongates with time. The other is 'footpoint flare', an enhancement in the X-ray intensity at the root of the jet structure. The footpoint flare exhibits significantly large X-ray enhancement than the jet structure. The X-ray enhancement decreases along the major axis of the jet structure from the footpoint flare to the apex. Based on the observed characteristics of the X-ray jets, a model of the X-ray jets generated by magnetic reconnection was proposed by Shibata et al. (1992). Numerical MHD simulations support the model (e.g. Yokoyama & Shibata 1995, Yokoyama & Shibata 1996).

From recent observations with the latest coronal imagers with higher resolutions and wider temperature coverages than those of SXT, it is revealed that the jet structures show complexity and dynamic motion. For example, there are blobs and loops in the jet structure which may be controlled by details of the energy release, which will also affect the motion of the X-ray jet (Shimojo et al. 2007, Moore et al. 2010); the jet structure moves transversely with respect to the direction of the elongation (Savcheva et al. 2007); multiple-jet structures appear during a single event (10~20 minutes) (e.g. Chae et al. 1999, Cirtain et al. 2007, Jiang et al. 2013). To understand the mechanism of X-ray jets, the complexity and dynamics of the jet structures is a key because such dynamics are

caused by the energy release of the magnetic reconnection. So, it is important to identify the shape of the jet structure and capture its time evolution based on the commonly accepted set of criteria.

The polar X-ray images obtained by *X-ray Telescope* (XRT: Golub et al. 2007, Kano et al. 2008) aboard the *Hinode* satellite (Kosugi et al. 2007) show that X-ray jets frequently occur in the polar coronal hole (Cirtain et al. 2007, Savcheva et al. 2007). Recently, it is revealed that the occurrence rate of the X-ray jet in the boundary of a coronal hole is higher than that in the coronal holes (CHs) and quiet regions (QRs) (Subramanian et al. 2010 Sako et al. 2013). Some studies have been discussed the energy and mass contributions of X-ray jets to the solar wind (e.g. Cirtain et al. 2007, Moore et al. 2010, Paraschiv et al. 2010). To examine the contributions of X-ray jets, it is essential to investigate the statistical properties of X-ray jets from a large number of events. For such an investigation, we need first to detect numerous X-ray jets. With (the semi-) automatic detection scheme of X-ray jets, the difficulty of such investigations would be significantly decreased.

The development of such a detection scheme for capturing X-ray jets is more difficult than that for transient brightenings, because an X-ray jet is characterized by the jet structures that is elongating with time. It means that we need to identify the shape of the jet structure and capture its time evolution for identifying X-ray jets. Some schemes for identifying X-ray jets have already been suggested. Shimojo (2012) demonstrated that jet structures can be detected using the optical flow method (Lucas & Kanade 1981). Martens et al. (2012) suggested application of the Gaussian and Sobel filter to the coronal image for identifying jet structures as straight lines in the filtered images. In this paper, we propose a new scheme for detecting X-ray jets in CHs and QRs using soft X-ray images obtained by XRT. Unlike the previous schemes, our scheme not only identifies the shape of the jet structure but also capture its time evolution, and generates maps that indicate the identified structures. The maps are useful not only for the identification of X-ray jets but also for the scientific analysis of the jets, as we will discuss in Section 3.3.5.

In Section 3.3, we describe our scheme, which is tested in Section 3.4. We show a study

using the time evolution and morphology of the jets detected in Section 3.5. Finally, we summarize this study in Section 3.6.

### 3.3 Auto detection of X-ray jets

Our detection scheme is composed of two main parts, preceded by preprocessing. In the first, active events, including transient brightenings and X-ray jets, are identified from X-ray images of CHs and QRs. In the second, the X-ray jets are selected from the active events based on the time evolution of the elongated structures. The average lifetime and width of the X-ray jets in CHs and QRs are 10 minutes and  $4 \times 10^3$  km, respectively (Sako et al. 2013). Our scheme needs three succeeding X-ray images to confirm the time evolution of the X-ray jets. Therefore, to detect a typical X-ray jet in CHs and QRs, our scheme requires X-ray images with a time cadence shorter than 3 minutes and the spatial resolution better than  $1000 \text{ km pixel}^{-1}$ .

#### 3.3.1 Preprocessing

Before we start the detection procedure, we preprocess the X-ray images. We calibrate the X-ray count and the pointing of the X-ray images by 'xrt\_prep.pro' and 'xrt\_jitter.pro', which are included in the Solar SoftWare package (SSWidl; Freeland & Handy 1998). Each X-ray image is normalized by the exposure time. Additionally, we execute the following processes for eliminating the effects of non-solar phenomena. First, in order to eliminate the effect of cosmic rays and high-energy particles in South Atlantic Anomaly (SAA) and High Latitude Anomaly (HLA), we apply the de-spike method proposed by Aschwanden et al. (2000a). Next, to improve the signal to noise ratio, we sum up the counts in  $2 \times 2$  pixels. After this process, we use the macro-pixel images.

The X-ray time profile of a pixel shows a small fluctuation that influences the detection

of X-ray jets. An average power spectrum of the X-ray time profile in CHs and QRs (Figure 3.1a) shows the power-law with the index of about -1. The fluctuation is therefore pink noise. We do not explore what causes the fluctuation in this paper. In order to remove the effect of the fluctuation, we create a running average with the 200-seconds window, and use the values for the following main processes.

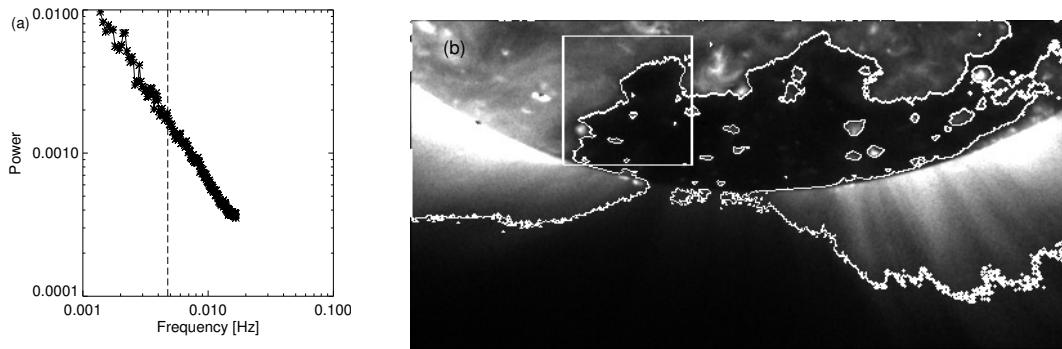


Figure 3.1: Figure 3.1a: A power spectrum of X-ray counts with a frequency. The dashed line shows  $4.7 \times 10^{-3}$  Hz. Figure 3.1b: An X-ray image around the south pole in January 17th, 2007. The white square presents the sample area to derive the power spectrum. White lines indicate contour of  $2 \text{ DN s}^{-1} \text{ pixel}^{-1}$  as the boundary of the CH.

### 3.3.2 Estimation of the Background Level and High-Lighting of the Jet Structure

We subtract the background level from an X-ray image to high-light the jet structure, but it is not easy to derive the background level automatically from the X-ray time profile that includes active events. To estimate the background level for the detection, we first take the minimum value from moving the 20-minutes window in the X-ray time profile of a pixel. This 20 minutes is two times the typical lifetime of X-ray jets (Savcheva et al. 2007, Sako et al. 2013). Thus we obtain the time profile of the local minimum of the X-ray counts. Because this time profile of the local minimum is still not varying smoothly, we once again create the running average of the local minimum with 20 minute window, and define the running average as the background level in the pixel. As an example, the dashed curve in Figure 3.2b is the time profile of the background level at the position of the asterisk mark in Figure 3.2a.

Figure 3.3a is an 'excess image' made by subtracting the background level from the X-ray image. In this figure, the visible structures include not only the active events but also bright and stable structures of XBPs, coronal loops, and polar plumes. They are caused by the intensity fluctuations of such structures larger than these of the dark region. To avoid these bright and stable structures, we use a modified excess image, which is normalized by a standard deviation of the excess (see below). We call the image as 'normalized excess image'. Because the standard deviations in the stable and bright structures are large, the normalized excess in these structures is similar to that in dark regions. Active events thus stand out in the normalized excess images.

The standard deviation used for making normalized excess images is calculated from the following process. First, we calculate the standard deviation and the average from the time series of the excess in a pixel. This standard deviation is not suitable for making the normalized excess image because it includes the excess by active events. To remove the effect by the active events, we re-calculate a new standard deviation and average from

the excesses only using the value that is smaller than the sum of the average and three times the standard deviation. After repeating for four times, we obtain the standard deviation for making the normalized excess image. The normalized excess image created from Figure 3.3a is shown as Figure 3.3b. The X-ray jet around the position (250 arcsec, -900 arcsec) in Figure 3.3b indicates not only the footpoint flare but also the jet structure. Outflow like threads over the limb are also emphasized in the normalized excess image.

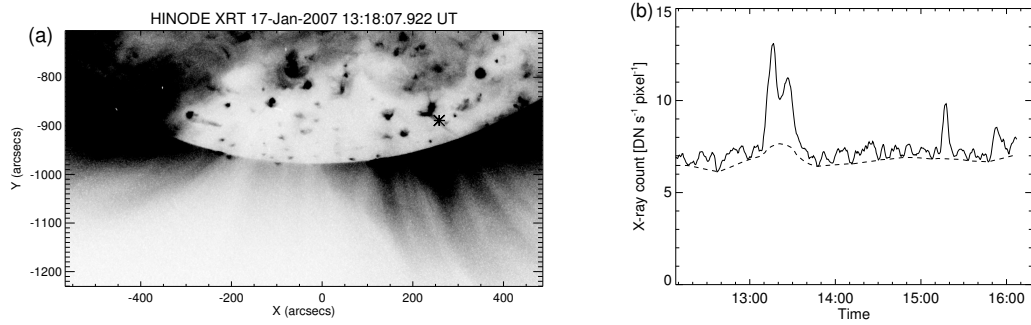


Figure 3.2: a) The X-ray image overplotted the asterisk point (the jet structure). The coordinate of this point is (250 arcsec, -900 arcsec). b) The time profile of the X-ray counts in this jet structure. The solid line is the original profile and the dashed line indicates the time profile of the background.

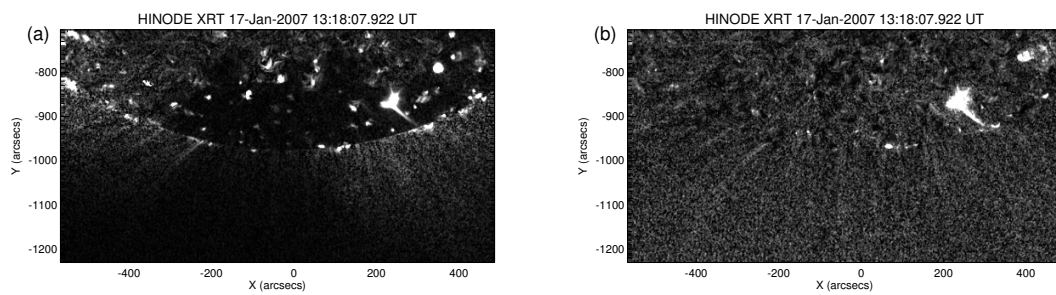


Figure 3.3: Examples of the excess image (a) and the normalized excess image (b) at the same time of Figure 3.2a.

Table 3.1: Terms of pixels defined in this study.

Terms	Explanation
'Candidate pixel'	A pixel in which the normalized excess is larger than a threshold.
' $r1^\pm$ pixel'	A candidate pixel with into increasing (+) or decreasing (-) X-ray intensity.
' $r2^\pm$ pixel'	A center pixel of the 'rectangular box', which satisfy two criterions for the number of $r1^\pm$ pixels.
' $r3^\pm$ pixel'	A pixel in a reconstructed shape of a candidate X-ray jets using the $r1^\pm$ pixel and the $r2^\pm$ pixel.
'Identified pixel'	A pixel in a candidate of X-ray jets.

### 3.3.3 Binarization

In Section 3.3.3 and 3.3.4, we define five terms for labeling pixels ('identified pixel', 'candidate pixel', 'r1 pixel', 'r2 pixel', and 'r3 pixel'). Table 3.1 gives the definition of these terms.

To identify the candidate pixels that indicate the structure of active events, we make a binary image from the normalized excess image based on a threshold of the normalized excess. The constant threshold is not satisfactory in identifying the candidate pixels, so we calculate the threshold in each pixel by a process similar to the one we used for obtaining the normalized excess image, but this time it is done in the spatial domain, rather than in the temporal domain. A blurred image is made from a normalized excess image using two-dimensional averaging filter with  $8 \times 10^4$  km radius. We execute the smoothing process twice to make the blurred image. The blurred image is used as a background level image of the normalized excess image. We first calculate the standard deviation from the normalized excess image. Then, we define the threshold, which is the sum of the background level and the three times the standard deviation. Next, we re-calculate a new standard deviation, only using values that are smaller than the threshold. After re-calculation, the threshold is renewed. After iterating the process for four times, we obtain the standard deviation of the normalized excess image. We choose the sum of two times the standard deviation and the background level of the normalized excess image as the threshold of a 'candidate pixel'. Finally, we identify the pixels where the normalized excess is larger than the threshold, and we make the binary image of the candidate pixels of the active events. Figure 3.4a is an image of the candidate pixels made from Figure 3.3b.

The normalized excess of the dark region is strongly influenced by the noise. Therefore, some dark pixels have survived in the binary image. Such pixels that the value in the 'excess' image smaller than  $1 \text{ DN s}^{-1} \text{ pixel}^{-1}$  are deleted from the binary images. For this, we make the mask (Figure 3.4c) from the 'excess' images.

As we mentioned in Section 3.2, an X-ray jet contains a jet structure and a footpoint

flare. When an X-ray jet occurs over the limb, there is no way to find the footpoint flare. The scheme cannot identify the X-ray jets that occur over the limb. On the other hand, some jet structures of the X-ray jets that occur on the disk elongate beyond the limb. To be able to study the length of such jets, we cannot remove the region over the limb. The over-the-limb events are observed frequently above the QRs and the ratio between the excess and the background is relatively small. Based on the tendency, we make a mask to remove the pixels where the ratio is smaller than 5%. The image of the mask is shown in Figure 3.4d. Figure 3.4b is the binary image of the candidate pixel (Figure 3.4a) after the filtering processes by two masks.

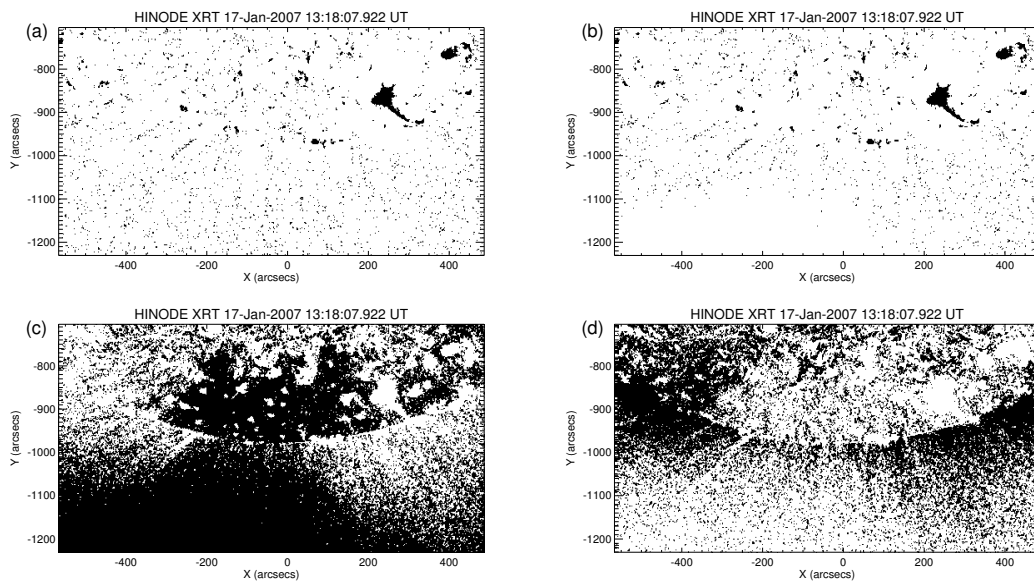


Figure 3.4: Results of the binary scheme. Figure 3.4a is the binary image, and Figure 3.4b is the binary image after the filtering processes by two masks. Figure 3.4c is an image of the pixels that the excess is larger than  $1 \text{ DN s}^{-1} \text{ pixel}^{-1}$ . Figure 3.4d is an image of the pixels that the ratio is smaller than 5%.

### 3.3.4 Reconstruction Scheme of Jet Structures

To detect X-ray jets in the later step of our method, described in Section 3.3.6, we identify the continuous narrow structures that are the candidate of jet structures. In a jet structure, the X-ray counts in some pixels can be too small to survive the process described in the previous sections. As a result, patchy structures appear in the binary image of the candidate pixels, and it is difficult to identify X-ray jets automatically from such structures. In order to reduce the difficulty, we reconstruct the structure of the active events.

Before identifying pixels of the candidate of jet structures, we need to take care of the group of candidate pixels that contain more than one event. If two active events occur by near simultaneously, their structures might appear to be connected. In this case, we cannot divide the events only from the binary image of candidate pixels. Since the time variations of their X-ray counts are different in most cases, we divide the candidate pixels into 'increasing' and 'decreasing' pixels from the difference of the X-ray counts between two time steps. We call an increasing pixel and a decreasing pixel as an ' $r1^+$  pixel' and ' $r1^-$  pixel', respectively. Until we merge the result of the final process in this section, we separately apply the same process to images of  $r1^+$  pixels and  $r1^-$  pixels (the  $r1^+$  and  $r1^-$  pixel are collectively called 'r1 pixel'). Due to the separation, the number of the r1 pixels in each binary image is now smaller and it is hard to identify the structures of active events from the images. To reduce the difficulty, when the r1 pixel exists in the binary image at one time step, we put the r1 pixel at the same position in the previous and next time steps. Figures 3.5a and 3.5b are examples of the binary image of  $r1^+$  pixels and  $r1^-$  pixels respectively. In this case, there is a possibility of artificially elongating the lifetime of an event, but such a possibility is small.

As the first step of the reconstruction, we enhance the continuous narrow structures. As a criterion to enhance the structure, we use the total number of the r1 pixels in two types of boxes. One box is named the 'rectangular box' and its size is  $10^4 \text{ km} \times 2 \times 10^4$

km which is similar to the typical size of the jet structures. In order to extract a shape of the jet structure, we successively rotate the rectangular box by 5 degrees to derive, in total, 36 boxes. We then use the box, among the 36 of them, that returns the maximum number of the  $r_1$  pixels. If the total number is over a threshold, we mark the pixel of the center of the box. The threshold is 30% of number of pixels of the rectangular box. We have to consider a bad case where the  $r_1$  pixels are distributed only around the edge of the rectangular box. Using the total number of the  $r_1$  pixels in the other box (called the 'square box'), which is smaller than the rectangular box, we can ensure that the  $r_1$  pixels concentrate around the center of the rectangular box. Its size is  $7.5 \times 10^3$  km  $\times$   $7.5 \times 10^3$  km except the four corner pixels of the box (therefore, it is not strictly a square.). We center a square box to each  $r_1$  pixel, and mark the pixel if the total number of the  $r_1$  pixels in the square box exceeds the threshold. The threshold is 30% of the number of pixels of the square box. We selected the marked pixels by both the 'rectangular' and 'square' box processes, and name the selected pixels ' $r_2$ ' pixels. Figures 3.5c and 3.5d are the binary image of  $r_2^+$  pixels and  $r_2^-$  pixels respectively. The narrow structures are enhanced in the binary image of the  $r_2$  pixels, but we cannot use the image for the detection directly because the structures of  $r_2$  pixels are expanded from the structures in the normalized excess image.

Based on the binary image of the  $r_2$  pixels, but still counting the  $r_1$  pixels, we reconstruct the continuous narrow structures. First, we apply the 'rectangular box' process, like the creation of the  $r_2$  pixel. There are two differences from the  $r_2$  pixel creation processes. One is that we use the position of the  $r_2$  pixel for setting up the rectangular box. The other one is that we mark the gravity center of the  $r_1$  pixels, not the center pixel of the rectangular box, if the total number of  $r_1$  pixels in the box exceeds the threshold. The marked pixels indicate the structure of an active event well, but there are still some non-marked pixels inside the structures. To fill the marked pixels inside of the structure, we mark a pixel when the 4 pixels of the  $3 \times 3$  pixels around the pixel are the marked pixel. We named the marked pixel ' $r_3$  pixel'. Figures 3.5e and 3.5f are the binary images of the

$r3^+$  pixels and  $r3^-$  pixels, respectively.

Finally, we combine the binary images of  $r3^+$  pixels and  $r3^-$  pixels. Figure 3.5g is the combined image made from Figures 3.5e and 3.5f. We call the  $r3^+$  and  $r3^-$  pixels in the combined image 'identified pixels'.

### **3.3.5 Identification of Individual Active Events and Detection of Their Shapes**

If identified pixels are located side by side in spatial and time domain, the group of the identified pixels indicates the range of one active event spatially and temporary (we call the process 'clustering'). Nevertheless, we cannot rule out the possibility that more than one event are included in the group of the identified pixels. To reduce the possibility, we temporally integrate the  $r3^+$  pixels that are in the group, and make a map that indicates the shape of the active event. We name the map a 'shape map'. In a typical event, the X-ray intensity rises faster than it falls, so the possibility that the group of the identified pixels includes the multiple events become large if the  $r3^-$  pixels were used. The shape-map process is applied to the binary image of the identified pixels in each time step, and the identified pixels that are located outside the structure identified by the shape map are removed. The group of the identified pixels that is cleaned up using the shape map are called 'identified event'.

### **3.3.6 Selection of X-ray Jets Based on Morphology and Time Evolution**

Among the identified events, there are not only X-ray jets but also other events, mainly transient brightenings. The group of the identified pixels of an identified event has the information of the shape and its time evolution, so it is easy to investigate the time evolution of the X-ray intensity distribution automatically. Based on the information, we select

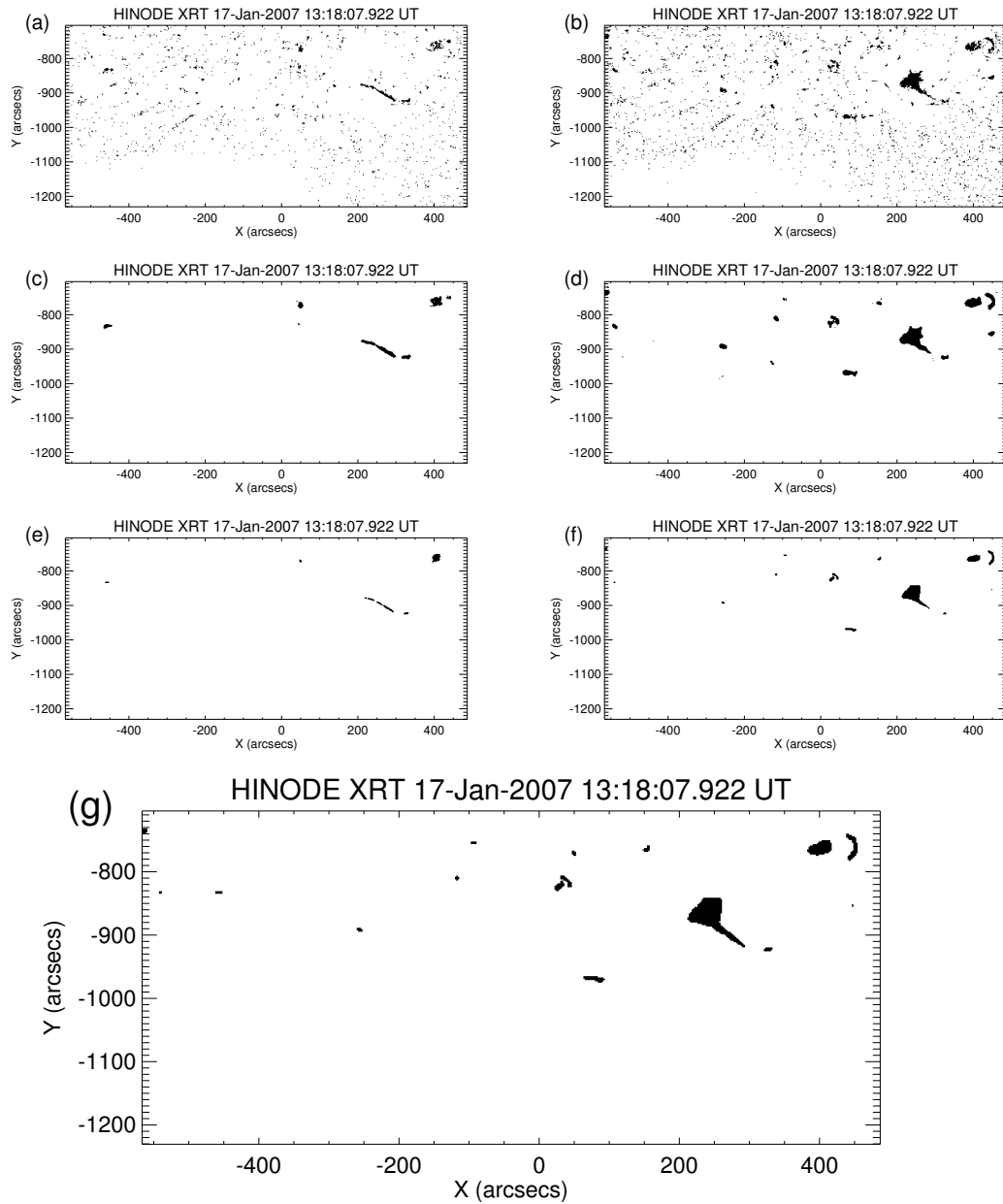


Figure 3.5: Results for the reconstruction process. Figures 3.5a and 3.5b are the images of the  $r1^+$  pixel and  $r1^-$  pixel. Figures 3.5c and 3.5d are the images of the  $r2^+$  pixel and  $r2^-$  pixel. Figures 3.5e and 3.5f are the images of the  $r3^+$  pixel and  $r3^-$  pixel. Figure 3.5g is the image to combine between Figures 3.5e and 3.5f.

the X-ray jets from the identified events using the following characteristics of X-ray jets;

- The apex of a jet structure is darker than the footpoint flare.
- A jet structure is narrow.
- A jet structure is elongating with time.

We set up the three criteria based on three characteristics. The candidate of X-ray jets is an identified event that satisfies the three criteria in the following sub-sections. In this section, we describe the details of the criteria.

### **Difference of X-ray Excesses between Apex and Footpoint Flare**

The X-ray excess along an X-ray jet decreases from the footpoint flare to the apex of the jet. We consider discriminating the X-ray jets from the others using the difference in the X-ray excess between the footpoint and the apex.

First, to find the position of the most enhanced region that is the footpoint if the event is an X-ray jet, we determine the temporal range during which this event is taking place. The images are integrated temporally and the averaged excess image of the event is obtained. From the averaged excess image, the enhanced pixels in which the averaged excess is larger than 10% of the largest excess in the image are selected. If the selected pixels make a single region, the center of the enhanced region is calculated as the center of gravity of the selected pixels, and we use this center as the origin of the coordinate for the identified event. If the selected pixels make multiple regions, the averaged excess of each region is calculated and the region that has the largest averaged excess is selected as the enhanced region of the jet. Then, the center of gravity of the region is calculated. The selected pixel that is farthest from the origin in the shape map is selected as the position of the apex. Using the positions of the origin and the apex, we determine the central axis along the narrow structure, and the bottom of the shape map is the position that is farthest from the apex. The length from the bottom to apex along the center axis is measured as

the maximum length of the identified event.

To compare the X-ray excesses at the apex and at the footpoint flare, the two time profiles are made. One time profile that indicates the time variation of the excess in the footpoint flare is made from integrating spatially the excess between the origin and 30% of the maximum length toward to the apex. The other for the excess time variation at the apex region is made from integrating the excess between the apex and 30% of the maximum length toward to the origin. One of the criterions is that the maximum value of the excess at the footpoint is larger than that at the apex.

### **Aspect Ratio of Jet Structure**

According the previous studies of X-ray jets (e.g. Sako et al. 2013), the structure with the aspect ratio (the length divided by the width) larger than 2 has been identified as the X-ray jet. To apply the criterion in our scheme, the width of an identified event is defined as the length of the structure in the shape map along the axis that is orthogonal to the major axis at the half maximum length. The aspect ratio is calculated from the width and the length, that is the distance from the origin to the apex.

### **Elongation of Jet Structure**

The most important criterion for identifying an X-ray jet is the elongating motion of the jet structure. To make a selection based on the criterion, we define three epochs for the group of the identified pixels. First one is the start time that is defined as the time when the identified pixels of the event appear for the first time. Second is the maximum time ( $t_{\max}$ ). This epoch is defined as the time when the identified pixels of the event appear at the apex. The last one is the appearing time that is defined as the time when an identified pixel appear in the region that is farther than 70% of the maximum length toward the apex for the first time. If the jet structure is elongating with time, the maximum time

and appearing time must not be the same as the start time. The third criterion uses this requirement.

### 3.3.7 Cut-off Process caused by Limitation of Scheme

Although we developed the scheme carefully, there are limitations. One comes from the size. If the candidate events that satisfy the criteria based on the expected characteristics of X-ray jet are small, most of them are not X-ray jets, but they originate in the perturbations in coronal loops. To avoid the misdetection, we exclude the events with the maximum length smaller than  $1.3 \times 10^4$  km. According to statistical studies of polar X-ray jets (e.g. Savcheva et al. 2007, Sako et al. 2013), the typical length of X-ray jets in the polar regions is  $2 \times 10^4$  km. Therefore, the cut-off process does not influence the detection of the typical X-ray jets in the regions.

Since the jet structure elongates with the time, an  $r3$  pixel in the position of the shape map is basically supposed to have been both  $r3^+$  pixel and  $r3^-$  pixel during the lifetime of the identified event (except the pixel reconstructed in Section 3.3.4). In Section 3.3.6, a minimum duration of the jet from the start time to the maximum time is two time steps. So we select the event that the lifetime of the identified event is longer than three time steps.

The events that possess all three characteristics of X-ray jets and remain after the cut-off process are named 'candidate events'. The list of the candidate event is the detection result by the scheme.

## 3.4 Performance Evaluation of Scheme

### 3.4.1 Observational Data for Evaluation

To evaluate performance of our new scheme for detecting X-ray jets, we use two XRT datasets. Both datasets are X-ray images, which include CHs and QRs in the polar regions in their field of view, and were acquired using the Al-poly analysis filter whose temperature response covers from 1 MK to 10 MK (Narukage et al. 2011). The exposure time is 16 seconds. One of the datasets was obtained on 17 January 2007. The temporal and spatial resolution of the datasets is 30 seconds and 1.02 arcsec, respectively. The FOV is  $1053 \text{ arcsec} \times 527 \text{ arcsec}$  and the center of the images is located around the south pole. The other dataset was obtained on 5 September 2007, and the temporal resolution is 120 seconds. The FOV is  $1053 \text{ arcsec} \times 394 \text{ arcsec}$ , centered around the north pole.

### 3.4.2 How Many Candidate Events Correspond to Actual X-ray Jets?

#### Classification of Candidate Events

To investigate variation of X-ray jets production over the types of regions, the candidate events are classified based on where they are produced. In practice, since our data sets include only CHs and QRs, we divide the observed regions into the two types of regions based on the X-ray intensity. The threshold is derived using the method described in Sako et al. (2013). Since there was a change in the mean intensity in the quiet regions during 2007 due to the CCD contamination of XRT (see the upper panel of Figure 8 by Narukage et al. 2011), different thresholds have to be used for our two datasets. For the dataset obtained on 17 January 2007, we define that the CH is the region where the X-ray intensity is less than  $2.0 \text{ DN s}^{-1} \text{ pixel}^{-1}$ . For the dataset obtained on 5 September 2007, we use  $3.5 \text{ DN s}^{-1} \text{ pixel}^{-1}$  as the threshold.

In investigating each candidate, we check if the candidate event possesses the three characteristics described in Section 3.3.6, by visual inspection. The candidate events that possess three characteristics are named 'identified jets'. The others are named 'non-jet events'. Some of the non-jet events are classified so by the lack of the structure that is elongating with time. Because the scheme compares the start time with the maximum and appearing time, it does not actually trace the flow of an X-ray jet. On the other hand, the verification of the elongating structure by visual inspection strongly depends on the spatial and temporal resolution of the dataset. Therefore, there is a possibility that small X-ray jets are included in non-jet events. We cannot however confirm the possibility, so we decide to remove these non-jet events from our list.

Our scheme has the function to separate an X-ray jet from neighboring events, but we are not able to neglect the possibility that the group of the candidate pixels of an event still includes two events. To test the performance of the event separation, we investigate each identified jet by visual inspection. If the group of the candidate pixels includes only one X-ray jet, we call the candidate events 'selected jet'.

### **Detection Result Using Dataset Obtained on 17 January 2007**

When we apply our scheme to the dataset obtained on 17 January 2007, the scheme identifies 48 candidate events. The numbers of events in the classes described in the previous sub-section are shown in the first two columns, labeled as '30 seconds', of Table 3.2. The rate of successful detection (the number of the identified jets divided by the number of the candidate events) is 71% in the CHs and 33% in the QRs. The rate of successful identification (the number of the selected jets divided by the number of the identified jets) in the CHs and the QRs are 88% and 87% respectively. These rates show that the scheme works correctly, except for detection in the QRs. The main reason for the false detections in the QRs is that some transient brightenings in a nearby region occur simultaneously when the activity of the region becomes relatively high. In such cases, the reconstruction

process of our scheme unites the brightenings and the event-selection process identifies the united event as the candidate event. Such candidate events are produced in the QRs frequently and have detrimental effects.

Table 3.2: Numbers of events in coronal regions with different cadences for January 17th.

	30 seconds		60 seconds		90 seconds	
	CH	QR	CH	QR	CH	QR
Candidate event	24	24	22	13	20	15
Identified jet	17	8	16	5	14	4
Selected jet	15	7	14	2	12	4
Non-jet event	7	16	6	8	6	11

## Dependence on Temporal Resolution of Dataset

In order to investigate the time-resolution dependence of the performance of our scheme, we make the datasets with the time resolution of 60 seconds and 90 seconds from the dataset obtained on 17 January 2007. Then, we apply our scheme to the datasets. The results of the detection are shown in Table 3.2. The numbers of the candidate events and identified jets slightly decreases with the increased intervals between images. The impacts of increasing the cadence from 30 seconds to 90 seconds, however, are not so significant.

### 3.4.3 How Many X-ray Jets Detected by Visual Inspection Does Our Scheme Detect?

Comparing the number of the events detected by our scheme with that detected by visual inspection is one of the most important aspects in evaluating the performance. To make the comparison, we use the list of the events detected by the visual inspection (Sako et al. 2013). We use the dataset obtained on 5 September 2007. To equalize the criterion of the detection by our scheme, we exclude these events that satisfy either of following three conditions from the event list of Sako et al. (2013). 1) The events occurred above the limb. 2) The maximum length of X-ray jets is smaller than  $1.3 \times 10^4$  km. 3) Jets in multiple-jet events except the first one. The reason for the third condition is as follows. Our scheme cannot distinguish sequential multiple jets produced at the same jet-producing site during a footpoint flare individually, and identifies them as an Identified jet. Therefore, when multiple jets produced during a footpoint flare are detected by visual inspection individually, we exclude the jets after the first one.

Table 3.3 shows the numbers of X-ray jets detected in the dataset obtained on 5 September 2007. The correspondence rates (the number of the X-ray jets detected by both method divided by the number of the jets detected by visual inspection) are 60% in the CH and 25% in the QR. Because the intensity level of the jet structure could affect the measure-

ment of the jet-length by eyes, we tend to overestimate the measured length of the jet with the large footpoint flare. Therefore, we cannot exclude these events by the criterion about the jet-length. After investigating the X-ray jets that are not detected in the QR by our scheme, we found that they have the large footpoint flares and short and narrow jet structures. It is hard for our scheme to detect such X-ray jets. So the correspondence rate in the QR is significantly small.

How many undetected jets by visual inspection can be detected by our scheme? Table 3.3 shows 45% in the CH and 40% in the QR of the identified jets are not be detected by visual inspection. We confirmed the most undetectable identified jets are not enhanced in the X-ray images and running difference images. This result implies the advantage of our scheme that we identify smaller enhancements of the jet using the normalized excess image. Of course, these smaller enhancement jets will be identifiable in the normalized excess image by visual inspection.

Table 3.3: Number of the events in the CH and the QR in September 5th, 2007.

	CH	QR
X-ray jets detected by visual inspection	10	12
X-ray jets detected by our scheme (identified jet)	11	5
X-ray jets detected by both methods	6	3
Identified jets undetected by visual inspection	5	2

### 3.5 An Application Example

One of the advantages of our scheme is that the shapes and time evolutions of X-ray jets are obtained as by-products. In this section, we present an example of the data analyses using the by-product. In the demonstration, we use the datasets described in Section 3.4.1.

Morphology of the X-ray jets is important in understanding the configuration of the coronal magnetic field associated with the X-ray jets. Shimojo et al. (1996) classified the shape of the X-ray jets basically by the difference between the widths at the bottom and at the top of the jet structure. Since our scheme outputs information on time evolution of the structure of X-ray jets, the classification can be done from the variation of the width at each position and at each epoch. Furthermore, we can easily derive the growth rate of the width that is important as pointed out by Moore et al. (2013) for understanding the production of X-ray jets. In the below, we show the results of the morphological analysis based on our scheme.

From the group of the identified pixels, we derive the width of the jet structure at each height and time  $W(t, h)$ . Here  $t$  is the time and  $h$  is the length from the outer edge of the X-ray jet's structure near the footpoint flare, which is computed from the shape map. We assume that the bottom of the jet structure is at 50% of the maximum jet length from the outer edge because the aspect ratio of X-ray jets detected by our scheme must be larger than 2. The width of the apex side is measured at 85% of the maximum length from the outer edge ( $h_2$ ). Based on the difference between the widths, we classify the selected jets into three groups defined as follows; The 'converging type' has the jet structure for which the difference, which is obtained by subtracting the apex width from the bottom width, is larger than  $3 \times 10^3$  km; The 'diverging type' is which the difference is smaller than  $-3 \times 10^3$  km; When the difference ranges between  $3 \times 10^3$  km and  $-3 \times 10^3$  km, we classify the X-ray jet as the 'constant type'. The length of  $3 \times 10^3$  km corresponds to the size of the two pixels in the macro-pixel image that is used in our scheme (see Section 3.3.1). Figure 3.6a shows the correlation plot between the width at the bottom and the width difference from

the 37 selected jets detected from the dataset of QRs and CHs obtained on 17 January and 5 September. For the figure, the X-ray jets in QRs and CHs are classified as 'converging type' or 'constant type'.

Moore et al. (2013) shows that one of the differences between a 'blowout-jet' and a 'standard-jet' is whether the width is expanding with time. Because our scheme outputs the X-ray jet's shape and their elongation, we can easily derive the growth rate of the width from them, and reduce the difficulty of dividing the X-ray jets to the two types. We use the width at 75% of the maximum length from the outer edge ( $h3$ ), and the growth rate is derived from the widths at the following two epochs. One epoch is the  $t_{\max}$  defined in Section 3.3.6, and the other is defined as the time when the identified pixels appear the region that is farther than the half of the maximum length from the outer edge ( $t'$ ). Figure 3.6b is the histogram of the growth rates made from the 37 selected jets, and shows that the width of the 33 X-ray jets is expanding with time.

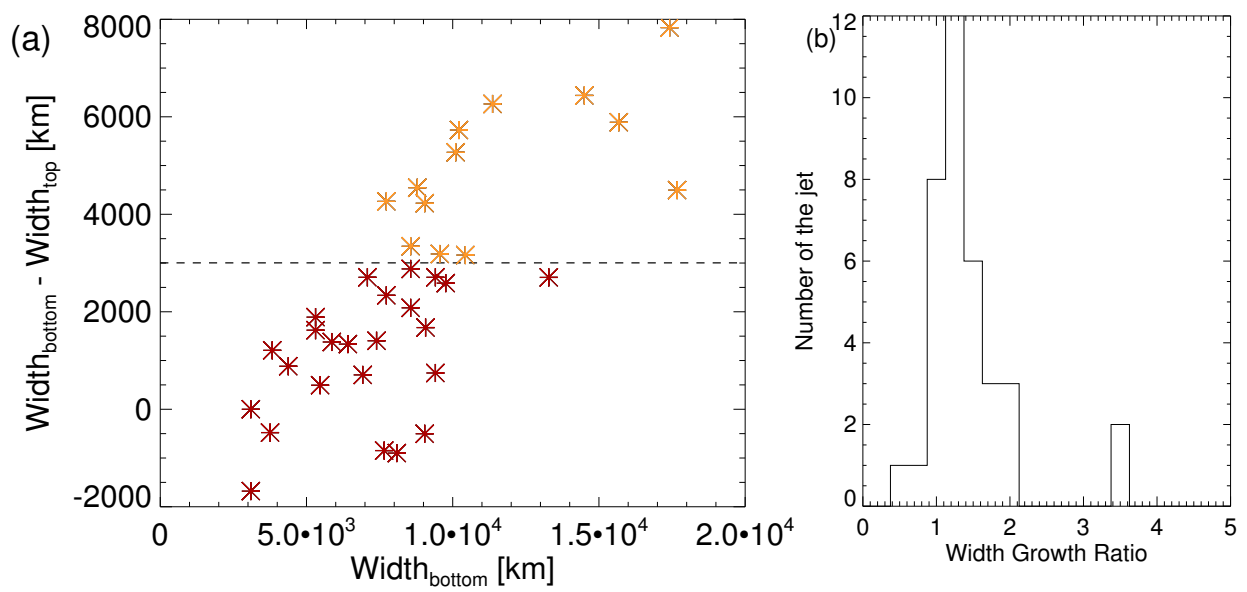


Figure 3.6: Characteristics of the width of the jet structure. Figure 3.6a is a scatter plot of the jet's width with a difference of the jet's width. The dash line shows  $\pm 3 \times 10^3$  km as the threshold. The orange and red-brown asterisks show the converging and constant types of the jet. Figure 3.6b is a histogram of the growth width ratio of selected jets. The bins size 0.25.

## 3.6 Summary

We developed a new scheme for detecting X-ray jets using X-ray images obtained by XRT aboard the *Hinode* satellite. The scheme comprises two main processes. First process carries out detection of active events that are identified by X-ray enhancements, and reconstructs narrow continuous structures of the active events. In the second process, the X-ray jets are selected from the active events based on the expected characteristics of X-ray jets. The scheme outputs the shape and its time evolution of the X-ray jets as by-products. To evaluate performance of our scheme, we applied our scheme to X-ray images that include QR and CHs. The features of our scheme are as follows;

- 70% of the events in the CHs that are detected by our scheme (candidate events) are in fact X-ray jets, but 67% of the candidate events in the QRs are not X-ray jets. The worse success rate in the QRs is mainly caused by the simultaneous brightenings in a nearby region. In such a case, our scheme identifies the simultaneous brightenings as an active event.
- Our scheme can separate the X-ray jet from the other event at the rate of over 85%, when the identified event is indeed an X-ray jet.
- The numbers of the candidate events and identified jets slightly decreases with the increased intervals between images. The impacts of increasing the cadence from 30 seconds to 90 seconds, however, are not so significant.
- Of the X-ray jets in the CHs detected by visual inspection, 60% can be detected by our scheme. The rate in the QRs is decreased to 25%. In the QR case, our scheme cannot detect X-ray jets with the large associated footpoint flares, and the short jet structure.

As by-products, the scheme outputs the shapes and time evolutions of the X-ray jets. We demonstrated how we could use the by-product for the morphological study of X-ray

jets. The detection by our scheme is not completely obtained the X-ray jets from the X-ray images, but we can get a large number of X-ray jets using our scheme from a large data volume automatically. We believe that by-products are useful for X-ray jet studies in many ways.

# Chapter 4

## A Study of Acceleration Mechanisms of X-ray Jets

### 4.1 Abstract

To study the acceleration mechanism of X-ray jets, we analyze 31 X-ray jets in active regions, 59 X-ray jets in quiet regions, and 60 X-ray jets in coronal holes from XRT data. No large differences in the morphological parameters are found between the jets in the active regions, the quiet regions, and the coronal holes. On the other hand, the jet speed, the thermal energy of the footpoint flare, the heating flux of the footpoint flare, and the temperature of the jet structure in the active regions are larger than those in the quiet regions and the coronal holes.

We evaluate the ranges of the temperature, and the speeds of the magnetic-driven jet and evaporation jet. Based on the expected ranges of the temperature and the speed of the jets, we classify the observed X-ray jets into the evaporation jets, the magnetic-driven jets, and the unclassified events. We have found that both evaporation jets and magnetic-driven jets are produced in the active regions, the quiet regions, and coronal holes.

## 4.2 Introduction

An X-ray jet is an active event in the solar corona. Details of the X-ray jet have been studied from the observations by Soft X-ray Telescope (SXT; Tsuneta et al. 1991) aboard the *Yohkoh* satellite (Ogawara et al., 1991) and X-Ray Telescope (XRT; Golub et al. 2007, Kano et al. 2008) aboard *Hinode* satellite (Kosugi et al., 2007). The structure of most X-ray jets comprises two components (Shibata et al. 1992, Shimojo et al. 1996). One is a narrow structure that elongates with time. We call it 'jet structure'. Because of the reported blue-shift motion in the jet structure (e.g. Kamio et al. 2007, Kamio et al. 2010), it is considered to be a plasma flow. The other is a 'footpoint flare', which is a bright loop or a bright point located around the root of a jet structure, and exhibits a brightening when an X-ray jet starts. The X-ray intensity of a footpoint flare is larger than that of the associating jet structure. Around a footprint flare, the photospheric magnetic field is found to be of mixed polarity (Shimojo et al., 1998), and emerging and/or canceling events are seen Chifor et al. (2008b), Shimojo & Tsuneta (2009), and Huang et al. (2012). Considering the evolution of the magnetic field and the morphology of the footpoint flare, Shibata et al. (1992) proposed a model of X-ray jets based on magnetic reconnection. Let us consider a closed loop in background unipolar fields as an initial magnetic configuration. Suppose that one footpoint of the closed field gets closer to the unipolar field with the opposite polarity. A current sheet will be created in the interface, where the magnetic reconnection will start, and an X-ray jet will be produced by the energy release.

Three types of plasma jets have been proposed as the X-ray jet candidates, based on the process responsible for converting the energy released by reconnection to kinetic energy (Shibata et al., 1992). One is the 'reconnection jet'. The heated plasma surrounding the reconnection point is accelerated by magnetic tension of the reconnected open field. The accelerated plasma along the open field is observed as a jet. Second is called the 'twisted jet'. If the reconnection is between unipolar fields and a twisted loop, the twist component of the loop propagates to the unipolar field by reconnection, and creates a gradient of the

magnetic pressure in the unipolar field. The hot plasma heated around the reconnection point is accelerated by the magnetic pressure gradient. Since the plasma in the first types of jets is accelerated by magnetic force, we call these jets 'magnetic-driven jets'. The third type is the 'evaporation jet'. The energy released by reconnection is transferred by non-thermal particle and/or thermal conduction. The downward energy heats the chromospheric plasma to the coronal temperature, and produces a pressure gradient between the corona and the chromosphere. The gradient of gas pressure accelerates hot chromospheric plasma and creates a hot and dense jet in the corona.

Two or three-dimensional MHD simulations based on the model of X-ray jets have been performed, but most of the simulations reproduce only the magnetic-driven jets because their simulation do not take account of the process of thermal conduction. On the other hand, in a one-dimensional HD simulation with the thermal conduction considered (Shimojo et al., 2001), only the evaporation jet is reproduced. Miyagoshi & Yokoyama (2003, 2004) carried out a two dimensional MHD simulation with the thermal conduction based on the two-loop side model. They show that two different types of jets (evaporation jet and low-density jet) are produced simultaneously around the emerging flux region. The low-density jets produced directly by reconnection jets, so the reconnection jet must have the density lower than that of the evaporation jet. They show that there are the differences in the density and the speed between the two types of jets.

One way to classify jets is to use only the speed of jets. The speed of magnetic-driven jet is similar to the Alfvén speed, while the plasma of the evaporation jet flows roughly with the sound speed. Since the difference between these speeds in the corona is large, we can easily classify the observed jets by a single speed threshold. So far, the acceleration mechanism of X-ray jets has been investigated this way in most of the previous studies (Shimojo et al. 1996, Cirtain et al. 2007). However, this classification scheme is not always justified, because Alfvén and sound speeds depend on the temperature, density and magnetic field strength of jets. Some authors examined the relation between the temperature and speed of an X-ray jet, noting that the sound speed is proportional to the square

root of the temperature. Shimojo & Shibata (2000) derived the temperature and density of the X-ray jets in active regions (ARs), and found that the most of the X-ray jets are slower than the sound speed of the plasma. They also found that the mass of the jets derived from the data is similar to the value estimated from the thermal energy of the footpoint flare assuming that the conductive flux from the flare site balances with the enthalpy flux carried by the evaporation jet. Matsui et al. (2012) and Tian et al. (2012) investigate the coronal jets observed with EUV Imaging Spectrometer (EIS: Culhane et al. 2007) aboard *Hinode* satellite, and found not only the jets whose speed depends on temperature, but also jets without such temperature dependence. They suggest that the former group represents one is the evaporation jet and the latter is the magnetic-driven jet. The X-ray jets observed with the EIS and other EUV imaging spectrometers are very rare because the timescale for scanning a wide field of view is longer than the lifetime of typical X-ray jets. Therefore, it is very hard to investigate the acceleration mechanisms of jets from the EUV spectrum data. X-ray jets in ARs have been identified as evaporation jets based on the physical parameters (temperature and mass) derived from the observation data (Shimojo & Shibata, 2000). The acceleration mechanism of X-ray jets in coronal holes (CHs) and quiet regions (QRs) is still a puzzle, and we cannot neglect a possibility of ARs producing magnetic-driven jets.

In this study, we derive the temperatures and the speeds of X-ray jets from the data. To compare with these estimates, we also evaluate the temperature and the speed in the evaporation jets and the magnetic-driven jets from the expected ranges of the physical parameters in the corona (magnetic strength, density, height to the reconnection region). By such comparison, we classify the X-ray jets into the evaporation jet, the magnetic-driven jet, the unclassified events.

## 4.3 Observation Data and Analysis Methods

### 4.3.1 Observation Data

The X-ray images used in the paper are obtained by the XRT during the period from January 1st, 2007 to May 15th, 2012 (Appendix 4.1). The spatial resolution is  $1.028 \text{ arcsec pixel}^{-1}$ . The time resolution is shorter than 30 seconds except for two AR data sets with 40 seconds cadence and two polar data sets with 35 seconds cadence. We used the X-ray images around the pole to obtain the jets in the CHs and the QRs. As for the detection of AR jets, we used the X-ray images around the ARs. We used the X-ray images taken with the following X-ray filters: Al-poly or Ti-poly. We pre-processed the X-ray intensity and instrument pointing using 'xrt\_prep.pro' and 'xrt\_jitter.pro' in the Solar Software package (SSWidl; Freeland & Handy 1998). The used X-ray images are normalized by the exposure time of the XRT.

### 4.3.2 Event Identification and Selection

#### Jet Identification

We first identify X-ray jets by visual inspection using normalized excess images. A normalized excess image is the X-ray image in which the background level is subtracted and what remains is divided by the standard deviation (for details see Chapter 3). We identify the continuous structure elongating with time as the jet structure.

After the identification of the X-ray jets, we select a subset for our analysis by the following three conditions. One condition is for measuring the apparent speed of a jet. When we measure the speed from the maximum length and duration, the measured apparent speed depends on the spatial and the time resolution of images, and the maximum length of the jet. To avoid the undesired effect of lower time and spatial resolutions, we select the X-ray jets longer than  $2.5 \times 10^4 \text{ km}$ . The second condition is for avoiding the saturated

pixels of the CCD. If there are the pixels in the structures of an X-ray jet with over 2500 DN (Kobelski et al., 2014), we remove the jet from our dataset. The third condition is for avoiding the effect of the contamination on the CCD. On the CCD of XRT, there are many contaminated regions like spots (Narukage et al., 2011). The precision of photometry in the contaminated region significantly degrades. Therefore, we do not analyze the jets if the contaminated regions indicated by the contamination map in the SSW database overlap with the footpoint flare. To classify X-ray jets by the jet-producing region, we use a threshold of the X-ray count for dividing the region into CHs and QRs (Sako et al., 2013). We identify ARs by visual inspection of X-ray images.

### **Identification of Bright Structures Related with Jet Structures**

Identification of the footpoint flare and derivation of its physical parameters are important for our analysis, since the temperature of a jet structure is estimated from the thermal energy in a footpoint flare, discussed in Section 4.3.3. In this section, we describe the identification procedures.

According to the X-ray jet model based on magnetic reconnection, the jet structure and the footpoint flare are produced simultaneously as a pair. Actually, it is not so simple to identify the pair, as discovered in recent high-resolution data. In most cases, more than one bright structures appear around the footpoint of the jet structure. Therefore, we need to identify which the bright structure is related with the jet structure as a footpoint flare.

The details of the identification is as follows; First, we identify all the bright structures around the footpoint of the jet structure by visual inspection, and enclose each of them with a rectangular box. Next, we make the running difference from the time profile of the averaged X-ray count in each rectangular box. If the running difference of the averaged X-ray count for a candidate structure is positive, we have a brightening for this structure. If there are brightenings in successive epochs, these brightenings are considered to represent a single event. There are some (temporally) isolated brightenings too, some of which

must be just a fluctuation in the background level (Chapter 3). We therefore ignore such isolated brightenings that the X-ray counts after the brightening is less than 1.5 times the count just before the brightening. We then look for overlaps in the period of brightening in each candidate structure and the period of jet-structure elongation, and select the bright structure in the overlapping period. If several bright structures are selected, we choose the brightest structure. We used the selected epoch as the time of the energy input into the footpoint flare ( $t_{\text{flare}}$ ). We define the size of the rectangular box that enclose the footpoint flare as the size of the footpoint flare ( $A_{\text{flare}}$ ).

### 4.3.3 Measurement and Estimation of Parameters

In this section, we describe how we measure and estimate parameters of footpoint flares and jet structures.

#### Thermal Energy of Footpoint Flares and Energy Flux From Reconnection Site

We assume that all the energy that precipitates from the reconnection site to the reconnected loop is thermalized. A peak thermal energy of the footpoint flare ( $E_{\text{flare}}$ ) is the total energy input from the reconnection site. If we moreover assume that the energy release rate is constant, the energy flux from the reconnection site ( $F$ ) can be derived from the peak thermal energy, the cross-section area to inject the released energy ( $A_{\text{cross}}$ ) and the time it takes to input the energy flux ( $t_{\text{flare}}$ ), as follows:

$$F \sim \frac{E_{\text{flare}}}{A_{\text{cross}} t_{\text{flare}}}. \quad (4.1)$$

Since  $t_{\text{flare}}$  is about a few minutes, we can neglect the radiative cooling. We assume that the shape of the footpoint flare is a semicircular loop. A height of the loop is defined as the

square root of the size of the footpoint flare. The width is derived for as  $0.25 \times \sqrt{A_{\text{flare}}}$  and the length is the longer of the rectangular region size of the footpoint flare. The derived width is 1-4 Mm, which is consistent with the loops regards by width by Aschwanden et al. (2000b). We use a square width as the cross-section area for the energy input. We estimate the  $F$  by Equation 4.1.

The peak thermal energy can in principle be derived from the peak X-ray counts taken with the X-ray filters, using the filter-ratio method, assuming the line-of-site depth of the footpoint flare and an isothermal plasma (e.g. Kano & Tsuneta 1995, Narukage et al. 2011). Unfortunately, however, most of the X-ray jets in QRs and CHs have been observed with only one X-ray filter, so we cannot apply the filter-ratio method for our dataset. In the current work, to derive the peak thermal energy, we derive the emission measure of the footpoint flare at the flare temperature, which is assumed to be  $10^{6.1}$  K, using the temperature response function of the X-ray filter. We used the peak X-ray count averaged in the footpoint flare during the period of the energy input into the footpoint flare. Although the estimated emission measure depends on the assumed flare temperature, the final estimate of the peak thermal energy depends only very weakly on the temperature. The reason is that the temperature responses of the X-ray filters used in the current work (Al-poly and Ti-poly filters), in the relevant temperature range of  $10^6$  K- $10^7$  K, are essentially proportional to the temperature squared, as shown in Figure 4.1. As a result, the electron number density is inversely proportional to the assumed temperature, which means that the thermal energy is not sensitive to the temperature.

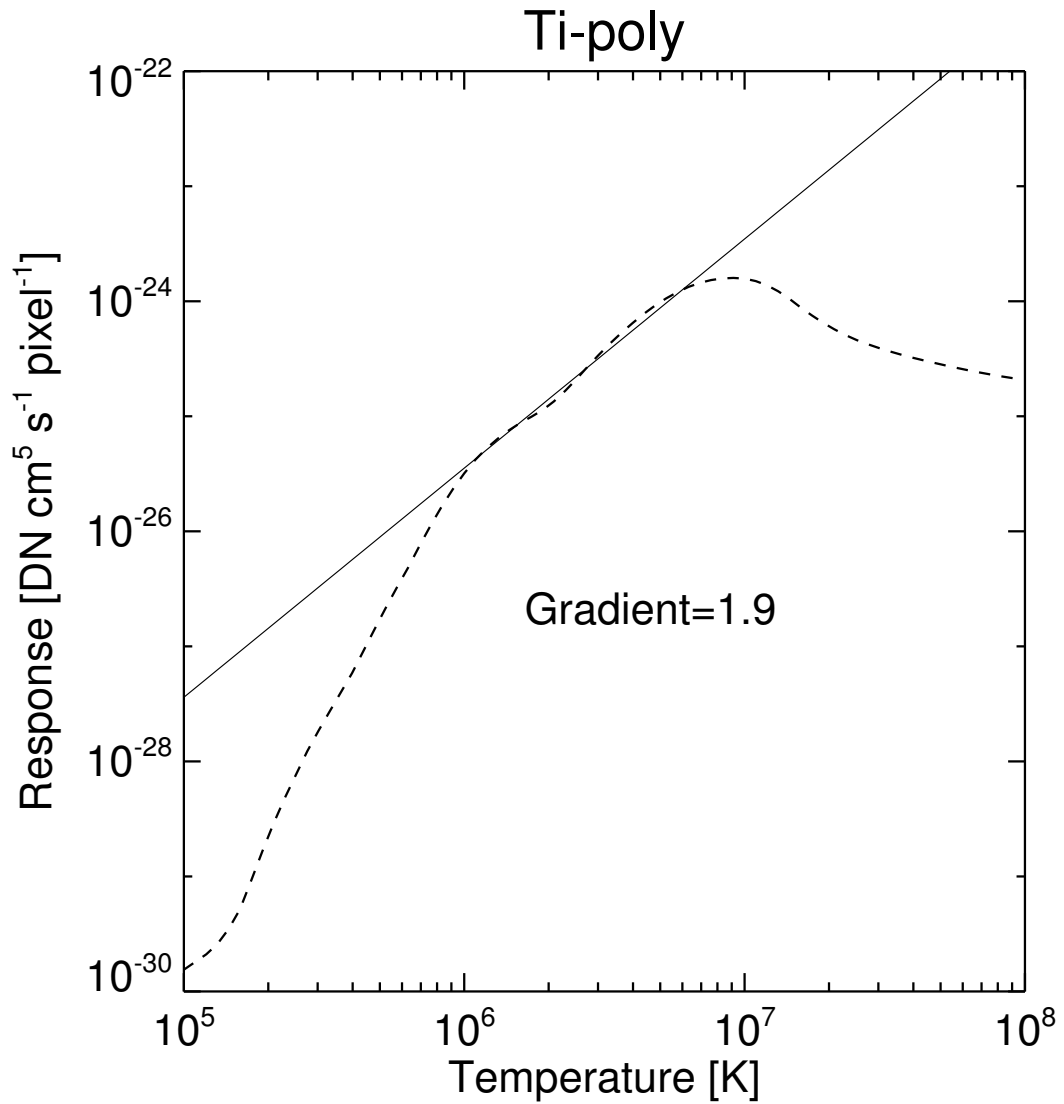


Figure 4.1: The temperature response curve of Ti-poly filter of XRT in May, 2010. The vertical axis is the data number flux when XRT observes the solar plasma at an inputted temperature, and the horizontal axis indicates the inputted temperature. The dashed line is the temperature response curve and the solid line is the fit line with an index of 1.9.

## **Length and Width of Jet Structures**

To measure the length of a jet structure in the X-ray image, we first define the apex and the footpoint of the jet by visual inspection of the image at the time of the maximum length, and mark five points between the apex and footpoint along the jet structure, by eyes. We fit a polynomial function with third order to the coordinates of the five points. This curve is used as the locus of the jet. The length of a jet structure is defined as the length of the curve between the apex and the footpoint along the locus of the jet. From the X-ray image at the time of the maximum length, the width of the jet is defined as the width of the middle of the jet structure, by visual inspection.

## **Apparent Speed of Jet Structures**

To estimate the apparent speed of a jet, a time-distance map of the X-ray excess along the locus of the jet is created. First of all, we need to estimate the background level, at selected position, one pixel-width apart from each other, along the locus. For each position, the X-ray count is integrated both spatially and temporally. The spatial range of integration is across the width of the jet, discussed in the previous subsection. The temporal range is from 1.5 hours before the jet begins, until 1.5 hours after the jet disappeared, except if there is no data, we obviously have to cut off there. Second, we binarize the normalized excess images using a threshold (for details see Chapter 3), and use those pixels above the threshold (and within the jet width) alone to compute the average X-ray count as function of time and position.

Finally, the background level is subtracted to yield the time-distance map of the X-ray excess, which is further smoothed by taking the running average with a  $5 \times 10^3$  km window. Note that, if a pixel has a negative value, it is excluded from the averaging procedure.

The edge is defined to be where the X-ray count exceeds one sigma level, which is de-

rived from the photon noise error expected from the background. When we estimate this error from the background intensity and the conversion factor of XRT (Narukage et al., 2011), we assume that the plasma temperature of ARs, QRs, and CHs is 2.5, 1.5, and 1.0 MK respectively (Withbroe & Noyes, 1977). The photon noise error is scaled as the factor of the square of  $N \times M$ , where  $N$  is the number of the binary pixels across the jet width and  $M$  is the number of the pixels in the time-distance map to average the X-ray excess within the  $5 \times 10^3$  km window. We determine two points at the top and bottom positions of the edge, and derive the time and the distance for the elongation of the jet structure to estimate the jet speed.

The speeds of the jets are underestimated because the estimated speeds are the apparent speeds. Some authors reported the actual jet speed derived from the EUV images and line spectra. Matsui et al. (2012) derived the speed of the AR jet using *STEREO*/SECCHI-EUVI A&B images. The actual jet speed is about 1.1 times the apparent speed derived from the data observed from the earth side. Because the estimation of the actual speed by their method is limited by the separation angle from the *STEREO* orbiter to the earth, we cannot estimate the actual speed for all of our jets. We estimate the actual speed of 6 AR jets by their method from the EUV images of 195 Å channel, and the ratio of the actual speed to the apparent speed of jets is 1.0-1.2. The LOS speeds of the jets around the pole are derived from the EUV line spectrum, and it is smaller than one hundred km s<sup>-1</sup> (e.g. Kamio et al. 2007, 2009). When we assume the radial magnetic fields, the actual speed of the jets is 1.1-1.2 time the averaging apparent speed of jets in the polar regions (170-200 km s<sup>-1</sup> by Sako et al. 2013). Therefore, we have to note that there is 10-20% uncertainty in our speed measurement.

## **Temperature of Jets**

In this part, we describe how to evaluate the temperature of an X-ray jet. When we derive a temperature of coronal plasma from XRT data, the filter ratio method (Narukage

et al., 2011, 2014) is usually used. To use the method, we need a minimum of two X-ray images taken with different X-ray filters within a time scale, which is shorter than the time variation of a phenomenon. Because most of the jets selected for the study were observed with only one X-ray filter, we cannot use the method and an alternative method is needed. In the paper, we evaluate the temperature from the heating flux ( $F$ ), which is derived in the previous part of the section, based on some assumptions. To validate our method, we compare the temperature evaluated by our method with the temperature derived by the filter ratio method, for some jets for which data obtained with two filters are found.

**Evaluation of Temperature from Heating Flux** For the evaluation of the temperature, we assume the followings based on the X-ray jet model; 1) The heating flux toward the footpoint flare is equal to that toward the jet structure. 2) The energy is transferred from the reconnection site to the chromosphere by thermal conduction. 3) The energy flux driven by thermal conduction from the reconnection site is balanced with the heating flux. 4) The plasma in a jet structure is isothermal. The balance in 3) implies

$$F \sim -\kappa \frac{dT}{dL}, \quad (4.2)$$

where  $L$  is the distance from the reconnection site to the chromosphere,  $T$  is the temperature. The factor  $\kappa$  is a thermal conduction coefficient along magnetic fields in the corona, and is approximated by  $\kappa = \kappa_0 T^{\frac{5}{2}}$ , where  $\kappa_0 = 9 \times 10^{-7}$  (Spitzer, 1962). Based on the X-ray jet model, we additionally assume that the reconnection occurs around the top of the reconnected loop. Therefore, the height of the reconnection site is much higher than the height of the upper boundary of chromosphere. Considering additionally that we can neglect the temperature of chromosphere because the coronal temperature is 100 times higher than the chromospheric temperature,  $dT/dL$  in Equation 4.2 can be simplified

to  $T/L$  and we can use  $\sqrt{A_{\text{flare}}}$  for  $L$ . As a result of the assumptions,  $T$  is now the temperature around the reconnection site. From Equations 4.1 and 4.2, we can give the following equation;

$$T \sim \left( \frac{FL}{\kappa_0} \right)^{\frac{2}{7}} \sim \left( \frac{E_{\text{flare}}L}{\kappa_0 A_{\text{cross}} t_{\text{flare}}} \right)^{\frac{2}{7}}. \quad (4.3)$$

Because a magnetic-driven jet is constructed from plasma around the reconnection site, the temperature of a magnetic-driven jet is the same as that around the reconnection site. On the other hand, the time scale of heat conduction of the system is much shorter than the time scale of dynamics and radiation, hence the plasma in the magnetic fluxes connected to the reconnection site is isothermal and the temperature of the evaporated plasma, which construct the footpoint flare and the evaporation jet, is also the same as that around the reconnection site. Therefore, we can evaluate the temperature of the both jets using Equation 4.3.

When we derive the thermal energy of the footpoint flare, we assume that the temperature of the footpoint flare is  $10^{6.1}$  K. The assumed temperature might be different from the temperature evaluated by Equation 4.3. To improve the precision of the evaluation, we can use the evaluated temperature for re-calculating the thermal energy of the footpoint flare. However, the difference found by the re-calculation is very small because the thermal energy derived from a XRT image taken with Al-poly or Ti-poly filter does not strongly depend on the temperature. This is why we do not carry out the iteration process.

**Estimation of Temperature by Filter Ratio Method** In all X-ray jets, 29 jets were observed with both Al-mesh and Ti-poly filters. Unfortunately, the jets in ARs are not included in the 29 jets. Because the temperature in the jet structure is uniform (Pucci et al., 2013), we integrate the X-ray counts spatially. For a footpoint flare, we integrate

the X-ray counts in the region which is described in Section 4.3.3. For a jet structure, we integrate the counts in the fan shape region constructed from the locus and width of the jet, which are defined in the previous part of the section.

As mentioned before, when we use the filter ratio method, the time difference between two images taken with the different filters must be shorter than the time scale of the event. Although the time variation of the total X-ray counts during a jet structure formation shows rapidly changes, the typical exposure time for QRs and CHs is long and the time difference between two images in most of the events is not sufficiently short. We select just 9 X-ray jets that satisfy the following criterions; 1) The time profile of the total X-ray count of the footpoint flare and jet structure has a single peak during the time of the energy input into the footpoint flare. 2) The time difference between two images taken with different X-ray filters is shorter than 8 seconds.

Finally, we make the time profile of running mean of the total X-ray counts of the footpoint flare and jet structure. The averaging is over three images. The time interval of images depends on the observing sequence and is roughly 60 seconds. Before applying the filter ratio method to the total X-ray counts, the background subtraction is done. The background level is defined as the running mean value before the time of the energy input into the footpoint flare. From these total X-ray counts after the background subtraction, we derive the temperature of the footpoint flare and jet structure. If there are multiple data points during the time of the energy input into the footpoint flare, we select the temperature that is associated with the largest total X-ray count during the time as that of the event. To valid the assumptions in the evaluation of the temperature from the heating flux, we compare these temperature of the jet structure with the estimated temperature from the heating flux in Section 4.4.4.

## 4.4 Estimated Parameters

We obtained 51 X-ray jets in the ARs, 83 X-ray jets in the QRs, and 91 X-ray jets in the CHs by visual inspection. We analyze 31 events in the ARs, 59 events in the QRs, and 60 events in the CHs, which satisfy the selection rules in Section 4.3.2. In this section, we report the estimated parameters of the jet structure and the footpoint flare, which is summarized in Table 4.1.

Table 4.1: Physical parameters of X-ray jets in each region

Parameter		ARs	QRs	CHs
Length of jets ( $10^4$ km)	Range	2.5-14.8	3.4-15.0	3.0-16.9
	Average	5.8	7.8	7.8
Width of jets ( $10^3$ km)	Range	1.5-9.8	3.0-15.0	3.8-13.5
	Average	3.9	7.0	7.2
Speed of jets ( $\text{km s}^{-1}$ )	Range	97-893	38-524	64-613
	Average	383	239	256
Area of footpoint flares ( $10^7$ $\text{km}^2$ )	Range	2.0-30.7	2.0-20.1	2.4-23.6
	Average	11.4	7.7	9.9
Time of energy input (second)	Range	22-399	56-510	60-1202
	Average	140	176	247
Cross-section ( $10^6$ $\text{km}^2$ )	Range	1.3-19.2	1.3-12.6	1.5-14.7
	Average	7.9	4.9	6.2
Thermal energy of footpoint flares ( $10^{25}$ erg)	Range	3.2-200.0	1.0-30.5	0.8-62.5
	Average	79.3	5.5	8.2
Heating flux ( $10^6$ $\text{erg cm}^{-2} \text{s}^{-1}$ )	Range	10.2-281.3	1.7-18.6	1.2-17.3
	Average	113.9	7.1	6.2

#### 4.4.1 Morphological Parameters

The measurement error of the length and the width is  $2 \times 10^3$  km- $3 \times 10^3$  km, which correspond to 3-4 pixels of the XRT. The width, and the area of the footpoint flare in the QRs, and CHs are similar to these parameters reported by Savcheva et al. (2007) and Sako et al. (2013), but the length of the jets is greater than the typical length by these studies because we had the minimum length of  $2.5 \times 10^4$  km. There are no large differences in the jet length, the jet width, and the area of the footpoint flares in the ARs, the QRs, and the CHs.

#### 4.4.2 Jet Speed

Because the projection effect is small as discussed in Section 4.3.3, we can regard the apparent speed as the actual speed. To estimate the jet speed, we smooth the time-slice map of the X-ray excess along the jet distance with a  $5 \times 10^3$  km window, and the positional error should be about the window size. We consider the measurement error of the apparent speed is roughly  $40 \text{ km s}^{-1}$ , using the average time for the jet structure elongation of 130 seconds.

The range of the jet speed is from few ten  $\text{km s}^{-1}$  to 500-800  $\text{km s}^{-1}$ . We can find the high-speed jets above  $500 \text{ km s}^{-1}$  not only in CHs but also in QRs and ARs. The average jet speed in CHs and QRs is slightly faster than the averaged speed in polar CHs and QRs (about  $170 \text{ km s}^{-1}$ ) by Savcheva et al. (2007) and Sako et al. (2013). The average jet speed in ARs is faster than the result by Shimojo et al. (1996), who studied the parameters of the X-ray jets and found 70% of their jets occurred in ARs. The apparent speed of the jet depends on the length of the jet and the spatial resolution and the time resolution of used images. Since the used XRT data have the spatial and the time resolution higher than those of the SXT and the length of the used jet is greater than  $2.5 \times 10^4$  km, we can identify the jets faster than previous studies. The average speed of the jets in ARs is faster than those in CHs and QRs.

### **4.4.3 Thermal Energy and Heating Flux of Footpoint Flare**

The averaged value for the thermal energy of the footpoint flares in the ARs is ten times larger than those in the QRs and the CHs. The thermal energy of the footpoint flare in the ARs is smaller than those of the footpoint flares in the ARs by Shimojo & Shibata (2000). From the assumption that the released energy by reconnection is converted to the thermal energy of the footpoint flare, as described in Section 4.3.3, the regional difference in the thermal energy indicates the difference in the amount of energy released by the reconnection region. The average heating flux of the AR jets is also larger than that of the jets in the CHs and the QRs. Because there is no large difference in the cross-section of the footpoint flares and the duration of the energy input in the footpoint flare between each region, the difference in the heating flux is showing the difference in the thermal energy of the footpoint flares.

### **4.4.4 Temperature of Footpoint Flare and Jet Structure**

First, we discuss validating the temperature evaluation from the heating flux. We estimate the temperatures of the 9 X-ray jets energy of the footpoint flares in QRs and CHs by the filter ratio method, and compare the estimated temperatures with the temperatures evaluated from heating flux (Figure 4.2). We found that there are no large differences between the temperatures calculated by the different methods. It suggests that the temperature evaluated from the heating flux is a good estimate of the temperature of jet structures. We also check whether the temperature of jet structures is the same as that of footpoint flares, using the temperature derived by the filter ratio method. Figure 4.3 shows the temperatures of the footpoint flare and jet structure analyzed in this study and Shimojo & Shibata (2000). Our data indicate no large difference in the temperatures of the structures,

which is consistent with their result. Hereafter, we discuss only the temperature evaluated from heating flux.

Figure 4.4 shows the estimated temperatures of the jet structures from the heating flux. The averaged temperature of the jet structure in each region is 1.6 MK (CHs), 1.7 MK (QRs) and 3.6 MK (ARs). The result shows that the temperature of the jets in the QRs is similar to that in the CHs, but the jets in the ARs are hotter than those in the other regions.

Shimojo & Shibata (2000) derived the temperature of 16 jets in ARs from the soft X-ray images obtained by *Yohkoh/SXT* using the filter ratio method (Hara et al., 1992), and the temperature range of the AR jets is 3-8 MK ( $\text{Log}_{10}T=6.5-6.9$ , average: 6.75). Because here the thermal energy of the footpoint flares in the ARs is smaller than those estimated by Shimojo & Shibata (2000), their average temperature is higher than our estimate. About 70% of the AR jets are hotter than 3 MK in temperature, which correspond to the temperature of the jet structures by Shimojo & Shibata (2000). There are the differences in the characteristics of the X-ray filters of the SXT and the XRT. We can detect jets with the temperature lower than 3 MK in ARs by the XRT. These considerations suggest the estimated temperatures of the jets in ARs are reasonable values.

To evaluate the temperature estimation of the jets in the CHs and the QRs, we investigate some jets observed with *SDO/AIA*. The jets in CHs and QRs appear only in the images of 193 Å and 211 Å channels. The peak of temperature response of these channels is around 1.5-2 MK (Lemen et al., 2012) that is similar to the peak of the temperature distribution for the CH jets and the QR jets (Figure 4.5). The estimated temperature of the jet structure in the polar CH by the filter ratio method (Pucci et al., 2013) is consistent with our results. These results suggest that our temperature estimates are valid.

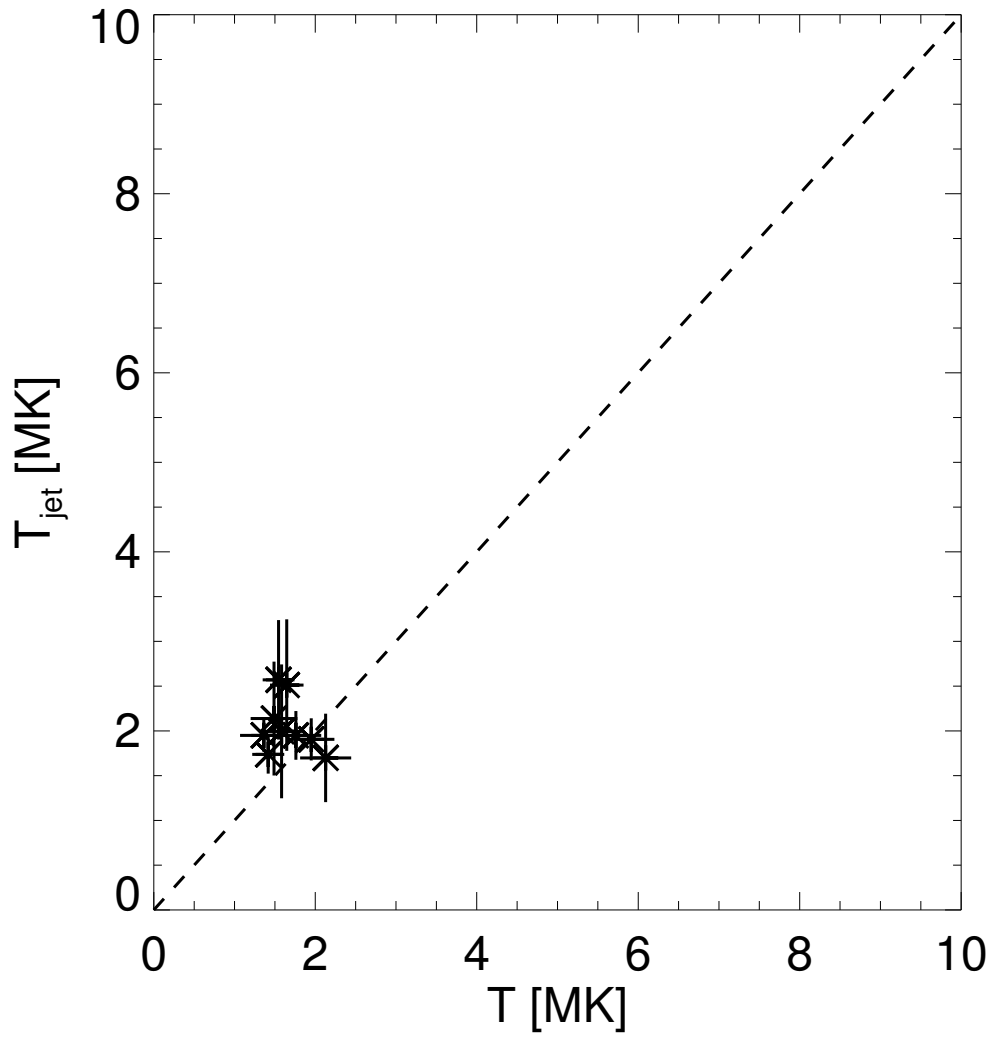


Figure 4.2: A scatter plot of the temperature of the jet structure estimated by two different methods. The vertical axis is the estimated temperature by filter ratio method. The horizontal axis is the temperature of the jet structure, which is estimated from the heating flux.

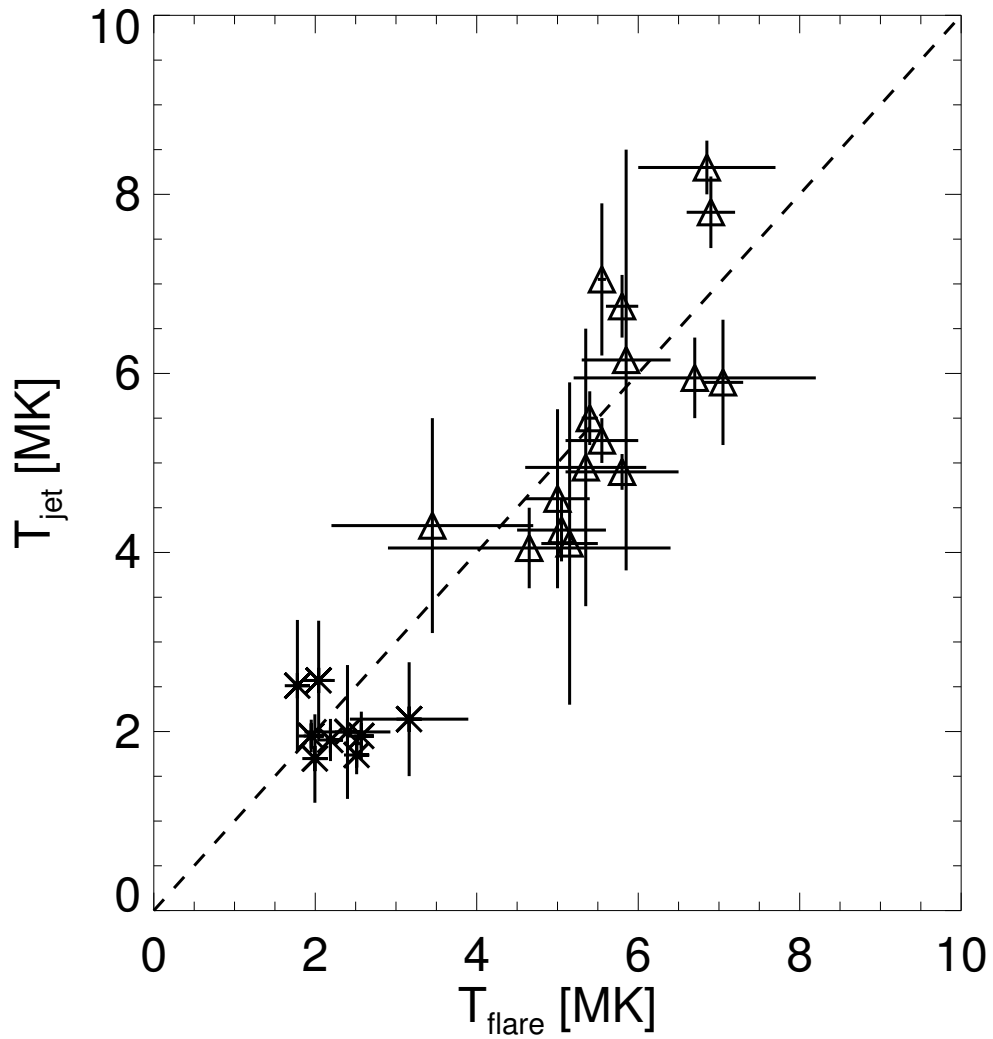


Figure 4.3: A scatter plot between the temperature of the jet structure and the footpoint flare. An asterisk indicates our events and a triangle indicate events by Shimojo & Shibata (2000).

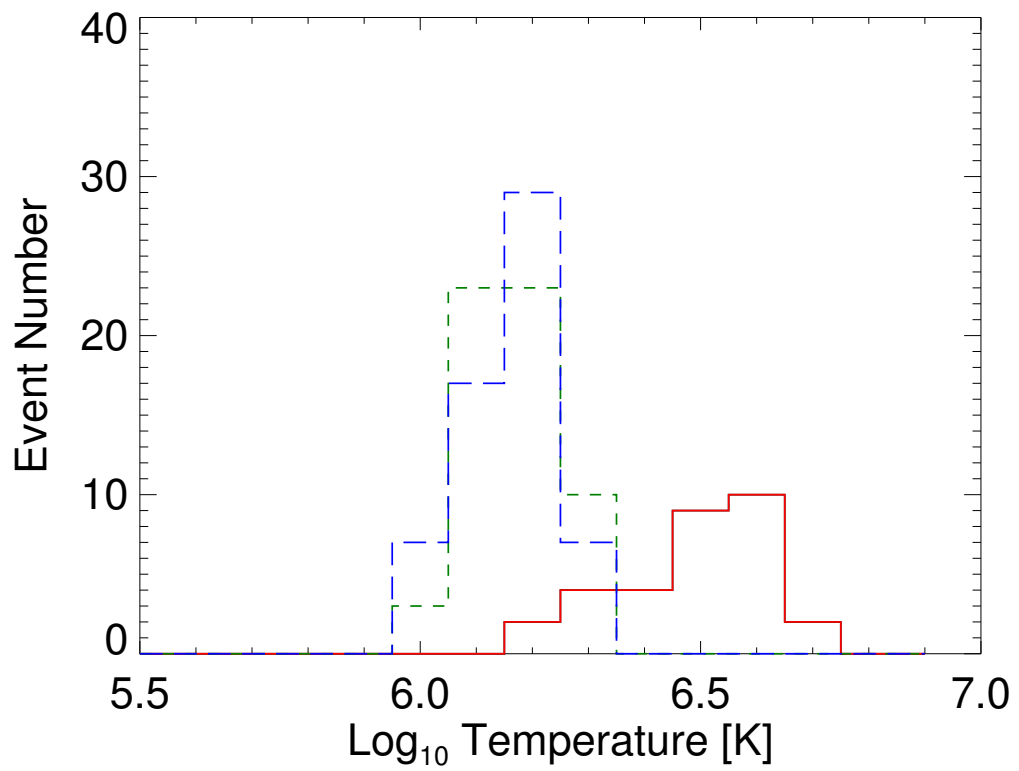


Figure 4.4: The histogram of the estimated jet temperature in the ARs (red solid), the QRs (green dash), and the CHs (blue dash).

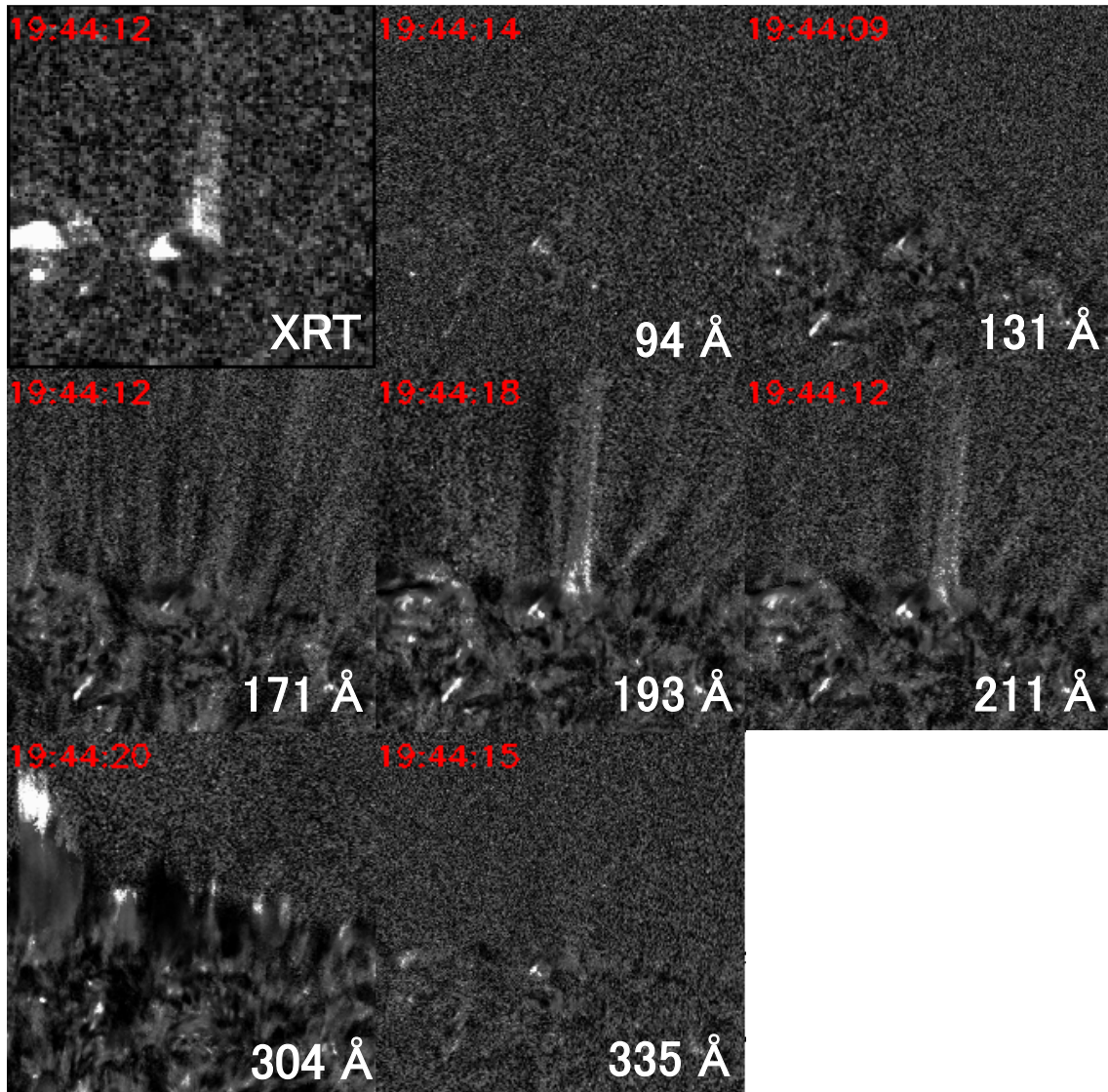


Figure 4.5: Cutout normalized images surrounding an X-ray jet in the CH around the north pole at September 10th, 2010. Upper panels are the images of XRT, 94 Å channel, and 131 Å channel. Middle panels are the images of 171 Å channel, 193 Å channel, and 211 Å channel. Lower panels are the images of 304 Å channel, 335 Å channel.

## 4.5 Acceleration Mechanism of Jet

In the model of X-ray jets by Shibata et al. (1992), there are jets driven by magnetic force and pressure force. In this section, we classify the observed jets into these jets using the estimated temperature and speed of jets.

### 4.5.1 Evaluation of Range For Temperature and Speed.

First, we describe how to determine the ranges for the temperature and the jet speed, for the magnetic-driven jet and the evaporation jet.

We estimate the temperature of jets based on the X-ray jet model described in the Section 4.2. For the estimation, we apply the same assumptions made in Section 4.3.3. Additionally, we assume that the heating flux of the footpoint flare can be regarded as the magnetic energy flux into the reconnection region (Miyagoshi & Yokoyama, 2004). The balance in the additional assumption is expressed by the following set of formulae (Miyagoshi & Yokoyama, 2004):

$$F \sim M_A \frac{B^2}{8\pi} V_A \quad (4.4)$$

$$V_A = \frac{B}{(4\pi n_e m_p)^{\frac{1}{2}}}. \quad (4.5)$$

Here  $B$  is the magnetic field strength,  $n_e$  is the electron number density in the inflow region,  $m_p$  is the proton mass,  $V_A$  is the Alfven speed and  $M_A$  is the Alfven Mach number of the inflow. From Equations 4.3, 4.4, and 4.5, the temperature  $T_{\text{cal}}$ , the temperature around the reconnection site and the evaporation plasma, is given by

$$T_{\text{cal}} \sim \left\{ \frac{B^3 L M_A}{8\pi\kappa_0(4\pi n_e m_p)^{\frac{1}{2}}} \right\}^{\frac{2}{7}}. \quad (4.6)$$

As discussed in Section 4.3.3, we consider no significant difference between the temperatures of the magnetic-driven jet and the evaporation jet. Therefore, we can estimate the temperature for both jets by Equation 4.6.

The speed of the magnetic-driven jet roughly is the Alfvén speed given by Equation 4.5 (Shibata et al., 1992). On the other hand, estimating the speed of the evaporation jet is not so simple because the supersonic flow is involved. Although the upper limit of the speed of the upward evaporation plasma has been estimated to be 2.35 times the sound speed of the evaporation plasma (Fisher et al., 1984), the hydrodynamic simulation with the thermal conduction using the realistic parameters of X-ray jets show that the Mach number of the upward evaporating plasma is 0.8-1.8 (Shimojo et al., 2001). Moreover, the Mach number of the upward evaporating plasma of large flares (M&X-classes) is 0.4-1.2 (Antonucci et al., 1990). Based on these results, we decide that the range of the speed of the evaporation jet is 0.4-1.2 times the sound speed.

Based on the assumptions described in this section, the estimations of the temperature and the speed of the jets need only three free parameters; magnetic field strength ( $B$ ), electron number density ( $n_e$ ), and distance from the reconnection site to the chromosphere ( $L$ ). We use the reasonable values for the free parameters and fix the ranges of the temperature and the speed of each jet. The used values are follows;  $B=0-500$  G,  $n_e=10^8-10^{9.5}$  cm<sup>-3</sup>, and  $L=10^8-10^{9.5}$  cm. The ranges of  $B$  and  $n_e$  cover the values of ARs, QRs, and CHs in the corona. The minimum and maximum of  $L$  correspond to the heights of the lower boundary of the corona and the coronal loop in ARs, respectively. In our calculation, only extreme values for  $L$  and  $n_e$  are considered, while  $B$  was varied in the given range.

To confirm that the estimated temperature and speed ranges for the evaporation jet are

reasonable, we create a plot that shows the estimated values and the data reported in the previous studies of flares and jets (Figure 4.6). Except for the flows with very low speed ( $< 100 \text{ km s}^{-1}$ ) and lower temperature ( $< 4 \text{ MK}$ ), the speeds and temperatures of the flows observed within flares are located in the estimated range for the evaporation jet. It shows that the evaluation of temperature and speed ranges for evaporation jets is correct because the flow in flares measured from the soft X-ray/EUV lines indicates the evaporation flow. In the case of jets, the speeds and temperatures of the jets in ARs derived from SXT data (Shimojo & Shibata, 2000) are located in the estimated range for the evaporation jet. It is consistent with Shimojo & Shibata (2000). On the other hand, the EUV spectrum data of jets shows differences. The speed and temperature of the jets reported by Tian et al. (2012) are located in the estimated range for two types of the jets, while the some data points of the jet reported by Matsui et al. (2012) are located in the estimated range for magnetic-driven jets. The data of Matsui et al. (2012) might suggest that the magnetic-driven jet is seen in multi-temperature structures.

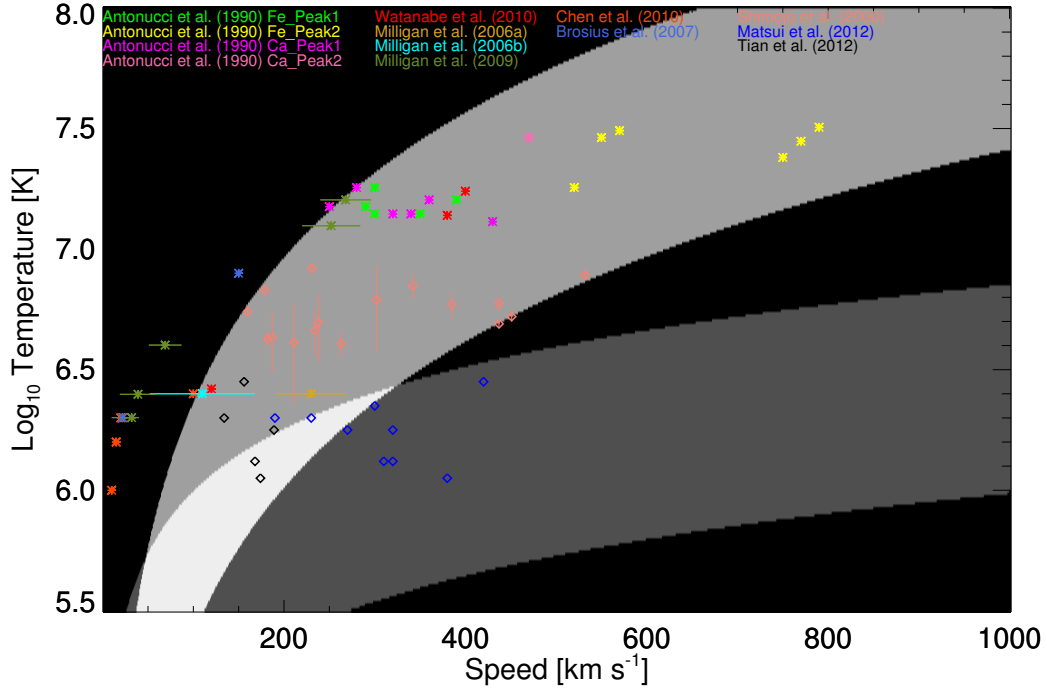


Figure 4.6: A temperature-speed map for jets. The temperature is evaluated by Equation 4.6. The speed of the magnetic-driven jet is evaluated by Equation 4.5. We decide the range of the speed of the evaporation jet is 0.4-1.2 times the sound speed. The dark-gray region is where the magnetic-driven jets are expected. The light-gray region is the region for the evaporation jets. The white region indicates where both the evaporation jet and the magnetic-driven jet might appear. The black region is outside the expectation. The asterisks indicate flares and diamonds are for jets. The previous studies of AR flares covered here are Antonucci et al. (1990), Watanabe et al. (2010), Milligan et al. (2006a), Milligan et al. (2006b), Milligan & Dennis (2009), Chen & Ding (2010), and Brosius & Holman (2007). The previous studies of AR jets included are Shimojo & Shibata (2000), Matsui et al. (2012), and Tian et al. (2012). We obtain the speed and the temperature of these events from the figures in their papers, if the speed and the temperature are not quoted directly.

## 4.5.2 Identification of Jet Type Based on Temperature and Speed

To classify the observed jets into the evaporation jets and magnetic-driven jets, we compare the temperature and the speed of the observed jets with the estimated ranges for two classes of jets. Figure 4.7 shows the estimated ranges and the data points of the observed X-ray jets. The jets in the ARs are located around 3-6 MK and distributed in both the estimated range for the evaporation and for the magnetic-driven jets. It indicates that a magnetic-driven jet is produced even in ARs. Most of the jets in the CHs and the QRs are located in the range of 1-2 MK temperature and 50-350 km s<sup>-1</sup> jet speed. The distribution of jets in the CHs and the QRs covers the estimated ranges for evaporation jets and for magnetic-driven jets and the overlapped range.

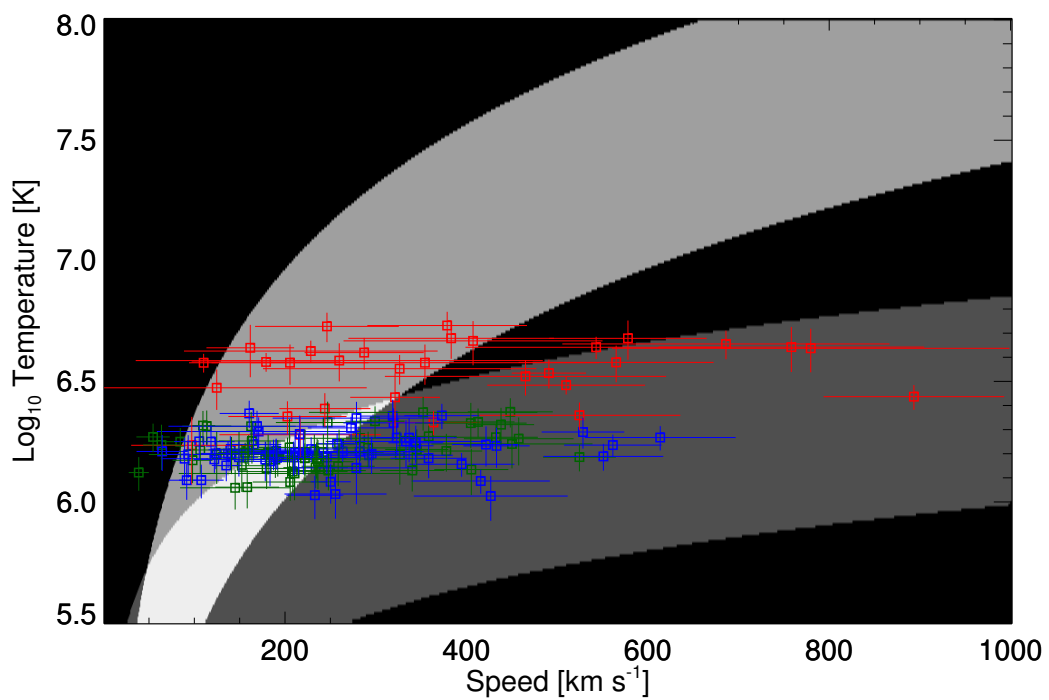


Figure 4.7: As Figure 4.6 except with our event samples plotted. The red squares, the green squares, and the blue squares indicate the AR jets, the QR jets, and the CH jets, respectively.

### 4.5.3 Multi-Jet Structures

The two-dimensional MHD simulation by Miyagoshi & Yokoyama (2004), with thermal conduction effect, reproduces the evaporation jet and the magnetic-driven jet simultaneously. They also show the differences in the speed, the density, and the emission measure between the two types of jets.

In our event list, there are few multi-jet structures because, when two jets appear successively, we are likely to miss the second one as such a brightening, on top of the already increased X-ray count due to the first jet, tends to be judged less significant. However, quite by chance we found an interesting multi-jet structure. The event, which is illustrated in Figure 4.8, occurred on 20 January 2007 in the QR. The X-ray jet is classified as an evaporation jet from the bright jet structure in the left side (the region marked 'Jet 1'). The speed of the first jet in Jet 1 (please note that here 'Jet 1' refers to a region rather than an event) is  $167 \text{ km s}^{-1}$ .

There are four bright structures (Foot 1, 2, 3, and 4) around the root of Jet 1. By comparing the running difference of the averaged intensity of the bright structures with the elongating period of the jet in Jet 1 (Figure 4.9), it is concluded that Foot 1, 2 and 3 are all related to the energy release that produces Jet 1, and they are the footpoint flares of the X-ray jet<sup>1</sup>. The said first jet appeared a few minutes before the peak time of Foot 3 (12:58:17UT; the dashed vertical line in Figure 4.9), which indicates the time of the maximum energy release. Around this time, another jet, a brighter one, is produced in Jet 1 (Figure 4.10). Moreover, yet another jet-like structure appeared in the region Jet 2, above Foot 2 and Foot 3. There was no brightening in Jet 2 before the peak time of Foot 3 (Figure 4.11). Because Jet 2 connects to Jet 1, and the distance between the root of Jet 2 and the cross point of the structures is short, we cannot measure the apparent speed of the jet in Jet 2, but can say that Jet 2 has a high-speed if Jet 2 is really a flow. Considering the relation between the appearing time of the jet in Jet 2, and the peak time of the energy re-

---

<sup>1</sup>Foot4 is associated with the other jet that is produced in the same region.

lease and the position of Jet 2 that is near the reconnection region predicted by the model of X-ray jets, the jet in Jet 2 might be a reconnection (magnetic-driven) jet.

We compare the averaged X-ray excess in Jet 1 with that in Jet 2 in Figure 4.8 at 12:58:17UT. The averaged X-ray excess in Jet 1 is 2.5 times larger than that in Jet 2. By design of our analysis, the temperatures for Jet 1 and Jet 2 are the same. Because the emission measure is proportional to the X-ray excess, there is the difference in the emission measure between Jet 1 and Jet 2. This result is consistent with the result by Miyagoshi & Yokoyama (2004), and further supports our classification scheme.

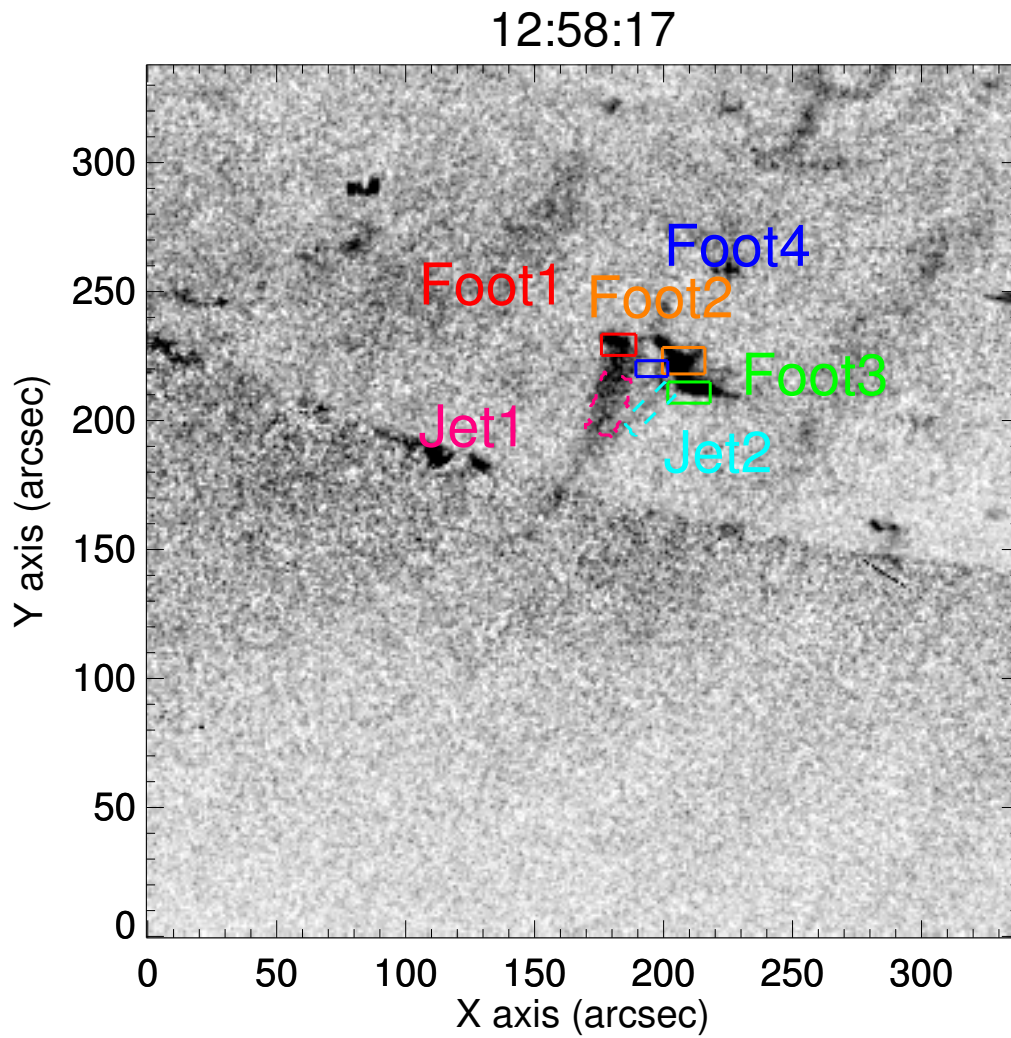


Figure 4.8: A cutout image surrounding an X-ray jet in the CH at January 20th, 2007. The solid rectangular regions are the footpoint flares and the dashed regions present the jet structures.

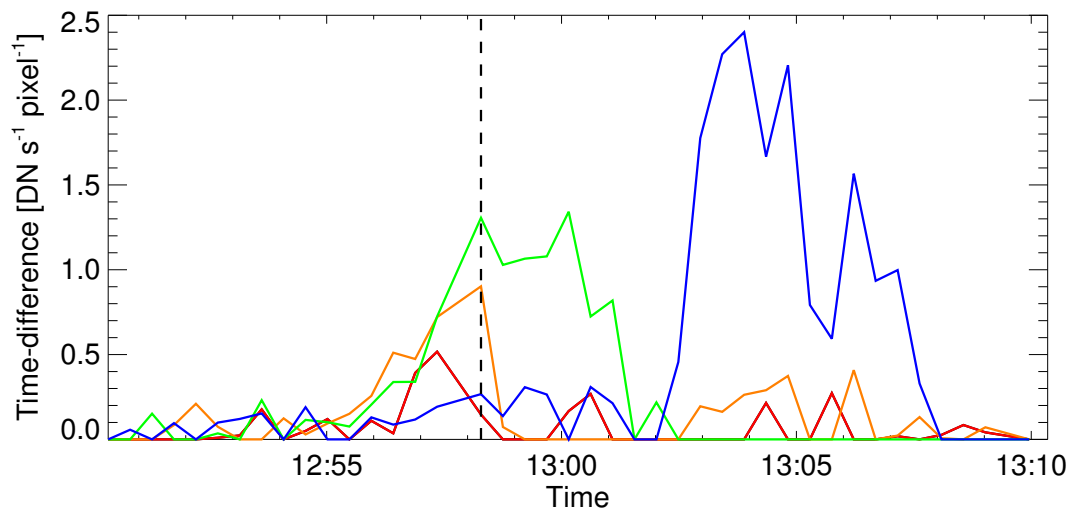


Figure 4.9: The running difference of the averaging X-ray count in Foot 1 (red), 2 (orange), 3 (green), and 4 (blue).

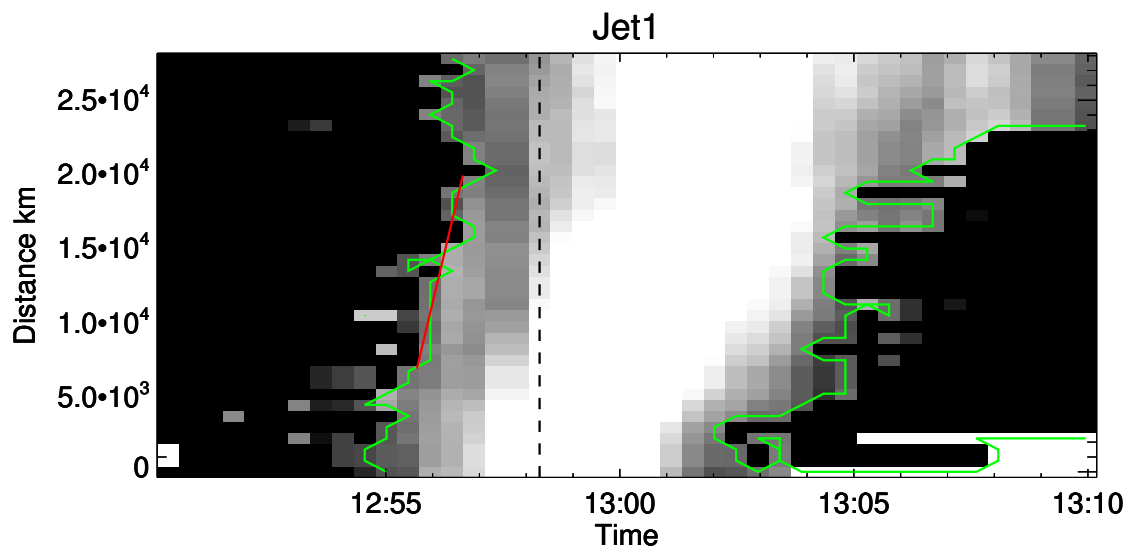


Figure 4.10: The time-distance map of the X-ray excess in Jet 1. The green line is the threshold of the photon noise error. We estimated the jet speed from the red line.

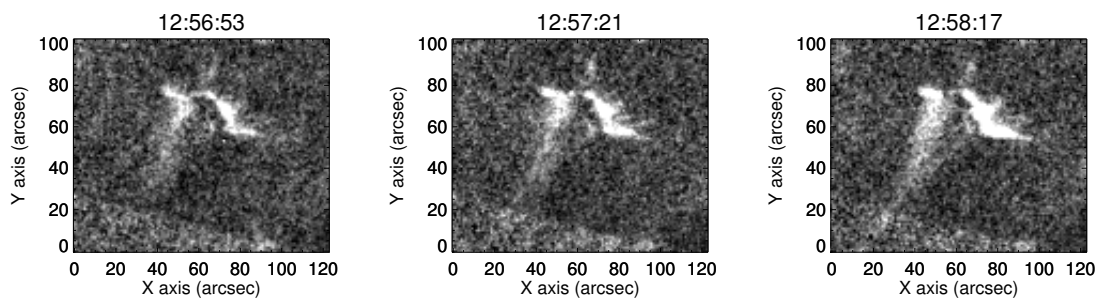


Figure 4.11: Cutout X-ray excess images around same event in Figure 4.6 from 12:56:53UT to 12:58:17UT.

## 4.6 Summary and Discussion

To study the acceleration mechanism of X-ray jets, we estimate the physical parameters of the jets in the ARs, the QRs, and the CHs. We obtain the following results.

1. There is no large difference in the morphological parameters of the jets in the ARs, the QRs, and the CHs. On the other hand the average value of the jet speed and the thermal energy of the footpoint flare in the ARs is larger than those in the QRs and the CHs.
2. We estimate the temperature of the jet structures from the thermal energy of the footpoint flare based on the assumptions described in Shimojo & Shibata (2000). The temperature of the jets in the ARs is higher than those of the jets in the QRs and the CHs.
3. We classify the X-ray jets in the ARs, the QRs, and the CHs into the evaporation jet and the magnetic-driven jet using the speed and the temperature of the jets. We found that both evaporation jets and magnetic-driven jets are produced in the ARs, the QRs, and CHs.
4. We found an event with both evaporation jet and magnetic-driven jet. The properties of the jets (emission measure and speed) are consistent with the prediction of Shibata et al. (1992) and Miyagoshi & Yokoyama (2004).

We found the different temperature and speed of the jets in the ARs, the QRs, and the CHs. What is the cause of these differences? To see clearly the relationship between the coronal magnetic field strength and the temperature, we add the contours of the magnetic field strength to the plot (Figure 4.12). The range of the magnetic strength of the AR jets is broad (from 10 G to 25 G). This result suggests the coronal magnetic strength in the background ARs is not uniform. On the other hand, the magnetic field strengths of the jets in the QRs and the CHs are concentrated around 5 G. Hence, the temperatures of jets

in such region concentrate around 1 MK and the regional difference in jets temperature is small.

In this study, we identified magnetic-driven jets in the corona (ARs, QRs, and CHs) using X-ray images obtained by XRT. We count the number of the two types of jets using the temperature and the speed of jets. The number ratio of the evaporation jet, the magnetic-driven jet, and ambiguous event (in overlapping region or non-expecting region) to the number of all of our jets is 0.33:0.38:0.29. For the AR jets, the number of the evaporation jet is larger than that of the magnetic-driven jet. Because the ambiguous event in the QRs and the CHs is about one-third of the jets, we cannot compare the event number of the evaporation jet with that of the magnetic-driven jet in the QRs and CHs. Because we used only jets larger than  $2.5 \times 10^4$  km in the length, we must note that the population of small jets, which are typical in CHs and QRs, may be different. To investigate the population of the two types of jets in such regions, we need the coronal imaging data obtained by the instrument with high spatial and temporal resolutions to investigate the time evolution of the smaller jet (a few times  $10^{-1}$  arcsec pixel $^{-1}$  and few seconds).

Based on our classification, details of the two types of jets will be studied. For example, there are the evaporation jet and the magnetic-driven jet in a footpoint flare at 01:35UT and 01:44UT in May 10th, 2012, which is illustrated in Figure 4.13. These jets have a similar morphology, but these jet structures elongate along the different magnetic fields. The first jet has the jet speed of  $690 \text{ km s}^{-1}$  and the temperature of 4.5 MK. The second jet has the  $260 \text{ km s}^{-1}$  speed and the 3.8 MK temperature. To understand the difference in the acceleration mechanism of these jets, the time evolution of the jet in smaller scales is important. We will investigate the time evolution of the velocity and temperature structures using multi-wavelength data with time and spatial resolution higher than those of XRT.

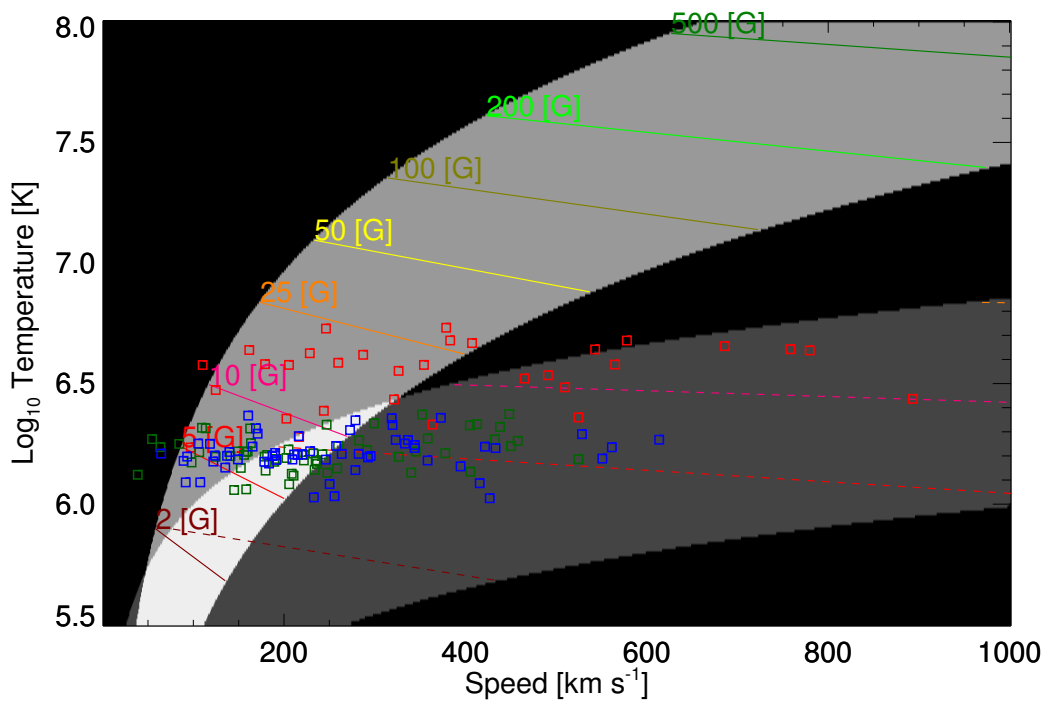


Figure 4.12: Same as Figure 4.2 but the observed jets and the contour for the coronal magnetic field strength overlapped. The red square, the green square, and the blue square indicate the AR jet, the QR jet, and the CH jet. The solid line and the dashed line show the contour of the coronal magnetic strength in the range of the evaporation jet and the magnetic-driven jet. The red-brown, red, pink, orange, yellow, olive, light green, and the dark green of the lines indicate 2 G, 5 G, 10 G, 25 G, 50 G, 100 G, 200 G, and 500 G.

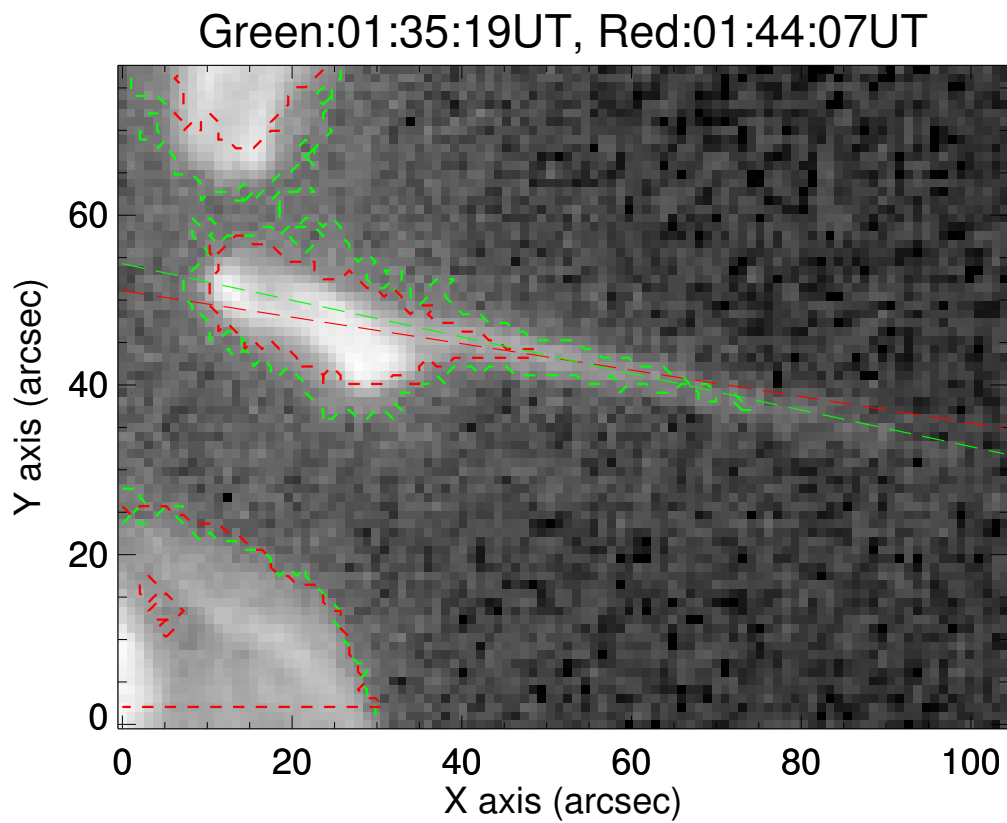


Figure 4.13: A cutout X-ray image surrounding an X-ray jet in AR at 01:35UT. The dashed green contour show the first jet at 01:35UT and the dashed red contour show the second jet at 01:44UT. The long dashed show the elongated direction of the first jet and the second jet.

## Appendix 4.1 Summary of Used XRT Observation Data

Table 4.2: Used XRT data in current study

Region	Start time [UT]	End time [UT]	Time [second]	Filter	FOVX [pixel]	FOVY [pixel]
CH,QR	2007-01-17T12:08:06	2007-01-17T16:07:11	30	Al-poly	1024	512
CH,QR	2007-01-18T12:11:36	2007-01-18T16:10:51	25	Al-poly	1024	512
CH,QR	2007-01-19T12:15:05	2007-01-19T18:03:48	30	Al-poly	1024	512
CH,QR	2007-01-20T12:11:38	2007-01-20T17:55:11	30	Al-poly	1024	512
CH,QR	2007-01-21T12:11:07	2007-01-21T17:59:20	30	Al-poly	1024	512
AR	2007-03-26T12:06:32	2007-03-26T18:20:53	40	Al-poly	512	512
AR	2007-03-26T18:36:32	2007-03-26T23:59:10	40	Al-poly	512	512
AR	2007-03-28T11:22:48	2007-03-28T17:52:00	10	Al-poly	512	512
AR	2007-06-06T18:14:35	2007-06-07T06:39:41	20	Ti-poly	512	512
AR	2007-06-07T06:54:05	2007-06-07T10:42:49	20	Ti-poly	512	512
AR	2007-06-08T10:50:06	2007-06-08T17:47:16	20	Ti-poly	512	512
AR	2007-06-14T00:15:43	2007-06-14T05:59:36	20	Ti-poly	512	512
AR	2007-07-15T00:06:48	2007-07-15T06:00:19	20	Al-poly	384	384
AR	2007-07-16T06:26:48	2007-07-16T10:29:57	20	Al-poly	384	384
AR	2010-03-28T18:13:38	2010-03-29T06:19:03	30	Ti-poly	384	384
CH,QR	2010-06-17T10:12:16	2010-06-17T17:38:08	30	Ti-poly	384	384
CH,QR	2010-07-24T10:11:50	2010-07-24T17:40:16	30	Ti-poly	384	384
AR	2010-08-02T18:16:18	2010-08-03T05:27:16	10	Ti-poly	384	384
CH,QR	2010-08-24T09:50:23	2010-08-24T18:11:44	35	Ti-poly	384	384
CH,QR	2010-08-25T06:14:23	2010-08-25T11:37:58	35	Ti-poly	384	384
CH,QR	2010-08-26T11:03:08	2010-08-26T18:50:40	30	Ti-poly	384	384
CH,QR	2010-08-29T18:16:37	2010-08-30T02:11:39	30	Ti-poly	384	384
CH,QR	2010-08-30T17:49:06	2010-08-31T01:44:08	30	Ti-poly	384	384
CH,QR	2010-09-04T17:55:37	2010-09-05T01:57:08	30	Ti-poly	384	384
CH,QR	2010-09-05T18:04:07	2010-09-06T01:59:08	30	Ti-poly	384	384
CH,QR	2010-09-06T18:19:08	2010-09-07T02:14:10	30	Ti-poly	384	384
CH,QR	2010-09-07T18:09:07	2010-09-08T02:04:08	30	Ti-poly	384	384
CH,QR	2010-09-08T18:12:38	2010-09-09T02:07:40	30	Ti-poly	384	384
CH,QR	2010-09-09T18:32:07	2010-09-10T02:27:10	30	Ti-poly	384	384

Table 4.3: Continued Table 4.2

Region	Start time (UT)	End time (UT)	Time (second)	Filter	FOVX (pixel)	FOVY (pixel)
CH,QR	2010-09-10T18:14:06	2010-09-11T02:09:08	30	Ti-poly	384	384
CH,QR	2010-09-11T18:10:35	2010-09-12T02:06:06	30	Ti-poly	384	384
CH,QR	2010-09-12T17:58:34	2010-09-13T01:59:36	30	Ti-poly	384	384
CH,QR	2010-09-16T18:14:05	2010-09-17T02:19:07	30	Ti-poly	384	384
CH,QR	2010-09-17T18:35:04	2010-09-18T02:39:06	30	Ti-poly	384	384
AR	2010-09-26T07:45:55	2010-09-26T12:04:29	30	Ti-poly	384	384
CH,QR	2010-10-01T10:06:03	2010-10-01T17:59:39	30	Al-poly	384	384
AR	2010-11-03T20:14:01	2010-11-04T05:47:02	25	Ti-poly	384	384
AR	2010-11-17T15:09:15	2010-11-17T18:49:33	30	Ti-poly	384	384
AR	2010-11-19T12:03:29	2010-11-19T17:41:56	25	Ti-poly	384	384
CH,QR	2011-01-06T09:57:05	2011-01-06T14:45:14	30	Al-poly	384	384
CH,QR	2011-01-07T10:14:41	2011-01-07T14:59:19	30	Al-poly	384	384
CH,QR	2011-02-04T10:25:05	2011-02-04T17:53:41	30	Al-poly	384	384
CH,QR	2011-02-05T10:09:35	2011-02-05T16:05:40	30	Al-poly	384	384
AR	2011-07-14T18:03:30	2011-07-14T19:51:14	20	Ti-poly	384	384
AR	2011-07-26T04:47:59	2011-07-26T10:15:48	20	Ti-poly	384	384
AR	2011-07-28T06:03:28	2011-07-28T09:37:23	20	Ti-poly	384	384
CH,QR	2011-08-26T11:25:16	2011-08-26T17:56:37	30	Ti-poly	384	384
CH,QR	2012-01-10T09:46:46	2012-01-10T15:29:41	30	Ti-poly	384	384
CH,QR	2012-01-28T09:41:15	2012-01-28T15:37:20	30	Ti-poly	384	384
CH,QR	2012-03-23T10:03:15	2012-03-23T15:29:39	30	Ti-poly	384	384
CH,QR	2012-04-06T09:33:22	2012-04-06T15:29:18	30	Ti-poly	384	384
CH,QR	2012-04-09T12:03:21	2012-04-09T17:57:45	30	Ti-poly	384	384
CH,QR	2012-04-12T09:53:50	2012-04-12T17:47:22	30	Ti-poly	384	384
CH,QR	2012-04-15T10:11:52	2012-04-15T15:59:43	30	Ti-poly	384	384
CH,QR	2012-04-30T10:03:17	2012-04-30T15:59:39	30	Ti-poly	384	384
AR	2012-05-09T18:13:30	2012-05-10T02:15:23	25	Ti-poly	384	384
AR	2012-05-10T07:00:59	2012-05-10T08:57:56	25	Ti-poly	384	384

# Chapter 5

## Summary and Future Directions

In this section, we summarize the results of our study and discuss the remaining questions and the future directions.

### 5.1 Summary of Our Results

We discussed two remaining questions arising from the results using the data obtained by *Hinode*/XRT and *Yohkoh*/SXT.

- Is there regional difference in characteristics of X-ray jets in the corona?
- Can both evaporation jets and magnetic-driven jets occur in active regions (ARs), quiet regions (QRs), and coronal holes (CHs)?

To answer these questions, we studied X-ray jets using X-ray images obtained by *Hinode*/XRT.

In Chapter 2, to answer the first question, we investigated the X-ray jet characteristics in polar regions, that included QRs and CHs, using XRT data for three weeks, and equatorial QRs. No significant regional differences in jet parameters (e.g. length, lifetime) are found for X-ray jets in the polar coronal holes (PCHs), the polar quiet regions (PQRs), the coronal hole boundary regions (CHBs), and the equatorial quiet regions (EQRs). There are,

however, regional differences in mean occurrence rates of X-ray jets. The mean occurrence rate of X-ray jets in CHBs is 2 to 3 times higher than that in the PCHs, the PQRs, and the EQRs. We cannot compare the mean occurrence rates of X-ray jets in such region with that of X-ray jets in ARs because we cannot obtain XRT data around ARs in conditions similar to the polar XRT data. We also showed the characteristics, which include the heating flux of the footpoint flare and the temperature of the jets, of X-ray jets longer than  $2.5 \times 10^4$  km in ARs, QRs, and CHs in Chapter 4. We found no large difference in the heating flux, thermal energy of the footpoint flare, and the temperature of the jets between in the QRs and CHs. From a comparison of jet characteristics in QRs and CHs with those in ARs, no significant regional differences in the jet length, width, and area of footpoint flare are found for the jets in such coronal region. The heating flux, thermal energy of footpoint flares, and the temperature of jets in ARs, however, are larger than those in QRs and CHs.

In Chapter 4, we first classified the jets into evaporation jets, magnetic-driven jets, and events overlapped both jets using the temperature and the speed of the jets. We identified both evaporation jets and magnetic-driven jets produced in ARs, QRs, and CHs, as our answer to the second question.

## **5.2 Remaining Questions and Future Directions**

In our studies, we showed the characteristics of X-ray jets in ARs, QRs, and CHs. In particular, we first identified the evaporation jet, the magnetic-driven jet, the overlapping event of two types in those coronal regions using the speed and the temperature of the jets. Before our study, it was difficult to know whether the observed characteristics of the jet are good indicators of the evaporation jet or the magnetic-driven jet. Based on our classification, we can separately study the characteristic of the evaporation jets and the magnetic-driven jet except the jets in the overlapping parameter region. We think that two

major questions of the acceleration mechanism of X-ray jets remain.

### 1. Three-Dimensional Magnetic Configuration of Coronal Jets

One weak point of imaging observations is that we study jets using only the plane-of-sky components of kinematics. Because only a few jets around the pole are reported with the three-dimensional morphology figured out (Patsourakos et al. 2008, Kamio et al. 2010), observationally the three-dimensional structure of the jet is not understood well.

The three-dimensional magnetic configuration of large AR flares is that the loop structures are lined along the two-ribbon flare. We can see this stable structure of flares for a few hours, while the shape of a jet is changing three-dimensionally during the lifetime of the jet ( $\sim 10$  minutes). Recent results that revealed the complex and multi-jet structures show the importance of understanding three-dimensional configuration of the jet. If the multi-jet structures appear in a single jet event, we cannot tell whether these jet structures elongate along the same field or different field. Based on the three-dimensional configuration of the jet structure, we can identify the untwist motion of twisted jets, and divide the magnetic-driven jet into the reconnection jets and the twisted jets.

We can study the three-dimensional jet structure using two images acquired nearly simultaneously from the different locations by the *STEREO/SECCHI-EUVI A&B* (Patsourakos et al. 2008, Kamio et al. 2010). Because the coronal jets frequently occur around the pole during the solar minimum, we will statistically investigate the three-dimensional jet structure. Another important study is the extrapolation of the coronal field surrounding the jet using measured vector magnetic fields in the photosphere by the *Hinode/SOT-SP*. Because the time interval of the scan for creating the vector field maps is much longer than the time scale of the jet, we can only study the magnetic configuration before or after the magnetic reconnection,

but the initial configuration of jets can be studied. In future, if the vector magnetic field in the chromosphere is observed with the performance similar to that of the SOT, we can study the height structure of the magnetic field around the jet from a comparison between the photospheric field and the chromospheric field.

## 2. Temperature and Velocity Structure of Coronal Jets

From the observations by *Yohkoh/SXT*, it was discovered that the energy release that produces the jets can be caused by magnetic reconnection. In this study, we identify the evaporation jets and the magnetic-driven jets using the temperature and the speed of the jets. As a next step, we need to investigate how much magnetic energy is converted by reconnection to kinetic energy and thermal energy. To study this, the details of the temperature and velocity structure of jets are needed. Because the observation by the *Hinode/EIS* does not resolve the time evolution of the jet, we cannot study temporal evolution of velocity and temperature structures of the jet.

The studies using the coronal imaging observation with the high resolution (*TRACE*, *XRT*, *AIA*, and *Hi-C*) reported complex and transient motions of jet structures (e.g. transverse motion, twisted structure). To derive the physical parameters using the imaging observation, we needed a lot of assumptions and only investigate the values averaged over the entire structure of the jet. To study the temperature and velocity structures in the complex and transient jet structure, we need the imaging spectroscopic observation with the time resolution and the spatial resolution that match the time and spatial scales of these jets. The *EUVST* in the *Solar-C* mission of Japan will be one of the best instruments for our purpose.

In this section, we discussed two kinds of studies using available data, and data that are expected in future. We hope these will lead to the final understanding of the acceleration process of coronal jets.

# References

- Abramenko, V. I., Fisk, L. A., & Yurchyshyn, V. B. 2006, *ApJ*, 641, L65
- Alexander, D., & Fletcher, L. 1999, *Sol. Phys.*, 190, 167
- Antonucci, E., Dodero, M. A., & Martin, R. 1990, *ApJS*, 73, 147
- Archontis, V., & Hood, A. W. 2013, *ApJ*, 769, L21
- Aschwanden, M. 2006, *Physics of the Solar Corona: An Introduction with Problems and Solutions* (Springer)
- Aschwanden, M. J., Nightingale, R. W., Tarbell, T. D., & Wolfson, C. J. 2000a, *ApJ*, 535, 1027
- Aschwanden, M. J., & Parnell, C. E. 2002, *ApJ*, 572, 1048
- Aschwanden, M. J., Tarbell, T. D., Nightingale, R. W., et al. 2000b, *ApJ*, 535, 1047
- Aurass, H., Klein, K.-L., & Martens, P. C. H. 1994, *Sol. Phys.*, 155, 203
- Bain, H. M., & Fletcher, L. 2009, *A&A*, 508, 1443
- Brosius, J. W., & Holman, G. D. 2007, *ApJ*, 659, L73
- Canfield, R. C., Reardon, K. P., Leka, K. D., et al. 1996, *ApJ*, 464, 1016
- Chae, J., Qiu, J., Wang, H., & Goode, P. R. 1999, *ApJ*, 513, L75

- Chandrashekar, K., Bemporad, A., Banerjee, D., Gupta, G. R., & Teriaca, L. 2014a, A&A, 561, A104
- Chandrashekar, K., Morton, R. J., Banerjee, D., & Gupta, G. R. 2014b, A&A, 562, A98
- Chen, F., & Ding, M. D. 2010, ApJ, 724, 640
- Chen, H., Jiang, Y., & Ma, S. 2009, Sol. Phys., 255, 79
- Chen, N., Ip, W.-H., & Innes, D. 2013, ApJ, 769, 96
- Chifor, C., Young, P. R., Isobe, H., et al. 2008a, A&A, 481, L57
- Chifor, C., Isobe, H., Mason, H. E., et al. 2008b, A&A, 491, 279
- Christe, S., Krucker, S., & Lin, R. P. 2008, ApJ, 680, L149
- Cirtain, J. W., Golub, L., Lundquist, L., et al. 2007, Science, 318, 1580
- Culhane, J. L., Harra, L. K., James, A. M., et al. 2007, Sol. Phys., 243, 19
- Dalmasse, K., Pariat, E., Antiochos, S. K., & DeVore, C. R. 2012, in EAS Publications Series, Vol. 55, EAS Publications Series, ed. M. Faurobert, C. Fang, & T. Corbard, 201–205
- Doschek, G. A., Landi, E., Warren, H. P., & Harra, L. K. 2010, ApJ, 710, 1806
- Fisher, G. H., Canfield, R. C., & McClymont, A. N. 1984, ApJ, 281, L79
- Fisk, L. A. 2003, Journal of Geophysical Research (Space Physics), 108, 1157
- Fletcher, L., Metcalf, T. R., Alexander, D., Brown, D. S., & Ryder, L. A. 2001, ApJ, 554, 451
- Freeland, S. L., & Handy, B. N. 1998, Sol. Phys., 182, 497
- Glesener, L., Krucker, S., & Lin, R. P. 2012, ApJ, 754, 9

Golub, L., Deluca, E., Austin, G., et al. 2007, *Sol. Phys.*, 243, 63

Guo, Y., Démoulin, P., Schmieder, B., et al. 2013, *A&A*, 555, A19

Hagenaar, H. J., De Rosa, M. L., & Schrijver, C. J. 2008, *ApJ*, 678, 541

Hara, H., Tsuneta, S., Lemen, J. R., Acton, L. W., & McTiernan, J. M. 1992, *PASJ*, 44, L135

He, J.-S., Marsch, E., Curdt, W., et al. 2010, *A&A*, 519, A49

Huang, Z., Madjarska, M. S., Doyle, J. G., & Lamb, D. A. 2012, *A&A*, 548, A62

Iida, Y., Hagenaar, H. J., & Yokoyama, T. 2012, *ApJ*, 752, 149

Ito, H., Tsuneta, S., Shiota, D., Tokumaru, M., & Fujiki, K. 2010, *ApJ*, 719, 131

Jiang, Y., Bi, Y., Yang, J., et al. 2013, *ApJ*, 775, 132

Jiang, Y. C., Chen, H. D., Li, K. J., Shen, Y. D., & Yang, L. H. 2007, *A&A*, 469, 331

Kahler, S., Jibben, P., & Deluca, E. E. 2010, *Sol. Phys.*, 262, 135

Kamio, S., Curdt, W., Teriaca, L., Inhester, B., & Solanki, S. K. 2010, *A&A*, 510, L1

Kamio, S., Hara, H., Watanabe, T., & Curdt, W. 2009, *A&A*, 502, 345

Kamio, S., Hara, H., Watanabe, T., et al. 2007, *PASJ*, 59, 757

Kano, R., & Tsuneta, S. 1995, *ApJ*, 454, 934

Kano, R., Sakao, T., Hara, H., et al. 2008, *Sol. Phys.*, 249, 263

Kim, Y.-H., Kim, K.-S., & Jang, M. 2001, *Sol. Phys.*, 203, 371

Kim, Y.-H., Moon, Y.-J., Park, Y.-D., et al. 2007, *PASJ*, 59, 763

Ko, Y.-K., Raymond, J. C., Gibson, S. E., et al. 2005, *ApJ*, 623, 519

- Kobelski, A. R., Saar, S. H., Weber, M. A., McKenzie, D. E., & Reeves, K. K. 2014, *Sol. Phys.*, 289, 2781
- Kosugi, T., Matsuzaki, K., Sakao, T., et al. 2007, *Sol. Phys.*, 243, 3
- Kotoku, J., Kano, R., Tsuneta, S., et al. 2007, *PASJ*, 59, 735
- Krucker, S., Kontar, E. P., Christe, S., Glesener, L., & Lin, R. P. 2011, *ApJ*, 742, 82
- Kundu, M. R., Raulin, J. P., Nitta, N., et al. 1995, *ApJ*, 447, L135
- Lemen, J. R., Title, A. M., Akin, D. J., et al. 2012, *Sol. Phys.*, 275, 17
- Liu, W., Berger, T. E., Title, A. M., Tarbell, T. D., & Low, B. C. 2011, *ApJ*, 728, 103
- Lucas, B. D., & Kanade, T. 1981, in *IJCAI*, ed. P. J. Hayes (William Kaufmann), 674–679
- Madjarska, M. S. 2011, *A&A*, 526, A19
- Madjarska, M. S., Huang, Z., Doyle, J. G., & Subramanian, S. 2012, *A&A*, 545, A67
- Martens, P. C. H., Attrill, G. D. R., Davey, A. R., et al. 2012, *Sol. Phys.*, 275, 79
- Martínez González, M. J., & Bellot Rubio, L. R. 2009, *ApJ*, 700, 1391
- Matsui, Y., Yokoyama, T., Kitagawa, N., & Imada, S. 2012, *ApJ*, 759, 15
- Milligan, R. O., & Dennis, B. R. 2009, *ApJ*, 699, 968
- Milligan, R. O., Gallagher, P. T., Mathioudakis, M., et al. 2006a, *ApJ*, 638, L117
- Milligan, R. O., Gallagher, P. T., Mathioudakis, M., & Keenan, F. P. 2006b, *ApJ*, 642, L169
- Miyagoshi, T., & Yokoyama, T. 2003, *ApJ*, 593, L133
- . 2004, *ApJ*, 614, 1042
- Moore, R. L., Cirtain, J. W., Sterling, A. C., & Falconer, D. A. 2010, *ApJ*, 720, 757

- Moore, R. L., Sterling, A. C., Falconer, D. A., & Robe, D. 2013, *ApJ*, 769, 134
- Moreno-Insertis, F., & Galsgaard, K. 2013, *ApJ*, 771, 20
- Moreno-Insertis, F., Galsgaard, K., & Ugarte-Urra, I. 2008, *ApJ*, 673, L211
- Narukage, N., Sakao, T., Kano, R., et al. 2014, *Sol. Phys.*, 289, 1029
- . 2011, *Sol. Phys.*, 269, 169
- Neugebauer, M. 2012, *ApJ*, 750, 50
- Nishizuka, N., Shimizu, M., Nakamura, T., et al. 2008, *ApJ*, 683, L83
- Nisticò, G., Bothmer, V., Patsourakos, S., & Zimbardo, G. 2009, *Sol. Phys.*, 259, 87
- . 2010, *Annales Geophysicae*, 28, 687
- Ogawara, Y., Takano, T., Kato, T., et al. 1991, *Sol. Phys.*, 136, 1
- Paraschiv, A. R., Lacatus, D. A., Badescu, T., et al. 2010, *Sol. Phys.*, 264, 365
- Pariat, E., Antiochos, S. K., & DeVore, C. R. 2009, *ApJ*, 691, 61
- . 2010, *ApJ*, 714, 1762
- Patsourakos, S., Pariat, E., Vourlidis, A., Antiochos, S. K., & Wuelser, J. P. 2008, *ApJ*, 680, L73
- Pucci, S., Poletto, G., Sterling, A. C., & Romoli, M. 2012, *ApJ*, 745, L31
- . 2013, *ApJ*, 776, 16
- Raouafi, N.-E., Georgoulis, M. K., Rust, D. M., & Bernasconi, P. N. 2010, *ApJ*, 718, 981
- Raulin, J. P., Kundu, M. R., Hudson, H. S., Nitta, N., & Raoult, A. 1996, *A&A*, 306, 299
- Sako, N., Shimojo, M., Watanabe, T., & Sekii, T. 2013, *ApJ*, 775, 22

- Savcheva, A., Cirtain, J. W., DeLuca, E. E., & Golub, L. 2009, *ApJ*, 702, L32
- Savcheva, A., Cirtain, J., Deluca, E. E., et al. 2007, *PASJ*, 59, 771
- Shibata, K., Nitta, N., Strong, K. T., et al. 1994, *ApJ*, 431, L51
- Shibata, K., Shimojo, M., Yokoyama, T., & Ohyama, M. 1997, in *Astronomical Society of the Pacific Conference Series*, Vol. 111, *Magnetic Reconnection in the Solar Atmosphere*, ed. R. D. Bentley & J. T. Mariska, 29
- Shibata, K., & Uchida, Y. 1985, *PASJ*, 37, 31
- . 1986, *Sol. Phys.*, 103, 299
- Shibata, K., Ishido, Y., Acton, L. W., et al. 1992, *PASJ*, 44, L173
- Shimizu, T. 1995, *PASJ*, 47, 251
- Shimizu, T., Shine, R. A., Title, A. M., Tarbell, T. D., & Frank, Z. 2002, *ApJ*, 574, 1074
- Shimizu, T., Tsuneta, S., Acton, L. W., Lemen, J. R., & Uchida, Y. 1992, *PASJ*, 44, L147
- Shimojo, M. 1999, PhD thesis, the school of Mathematics and Physical Science, the Graduate University of Advanced Studies for the degree of Doctor for Philosophy (Science)
- Shimojo, M. 2012, in *Astronomical Society of the Pacific Conference Series*, Vol. 454, *Hinode-3: The 3rd Hinode Science Meeting*, ed. T. Sekii, T. Watanabe, & T. Sakurai, 103
- Shimojo, M., Hashimoto, S., Shibata, K., et al. 1996, *PASJ*, 48, 123
- Shimojo, M., & Shibata, K. 2000, *ApJ*, 542, 1100
- Shimojo, M., Shibata, K., & Harvey, K. L. 1998, *Sol. Phys.*, 178, 379
- Shimojo, M., Shibata, K., Yokoyama, T., & Hori, K. 2001, *ApJ*, 550, 1051

- Shimojo, M., & Tsuneta, S. 2009, *ApJ*, 706, L145
- Shimojo, M., Narukage, N., Kano, R., et al. 2007, *PASJ*, 59, 745
- Shiota, D., Tsuneta, S., Shimojo, M., et al. 2012, *ApJ*, 753, 157
- Spitzer, L. 1962, *Physics of Fully Ionized Gases*
- Subramanian, S., Madjarska, M. S., & Doyle, J. G. 2010, *A&A*, 516, A50
- Tian, H., McIntosh, S. W., Xia, L., He, J., & Wang, X. 2012, *ApJ*, 748, 106
- Tsuneta, S., Acton, L., Bruner, M., et al. 1991, *Sol. Phys.*, 136, 37
- Tsuneta, S., Ichimoto, K., Katsukawa, Y., et al. 2008, *ApJ*, 688, 1374
- Uchida, Y., & Shibata, K. 1985, *PASJ*, 37, 515
- Wang, Y.-M., Hawley, S. H., & Sheeley, Jr., N. R. 1996, *Science*, 271, 464
- Wang, Y.-M., & Sheeley, Jr., N. R. 2002, *ApJ*, 575, 542
- Watanabe, T., Hara, H., Sterling, A. C., & Harra, L. K. 2010, *ApJ*, 719, 213
- Wiegmann, T., Solanki, S. K., Borrero, J. M., et al. 2010, *ApJ*, 723, L185
- Withbroe, G. L., & Noyes, R. W. 1977, *ARA&A*, 15, 363
- Yang, J.-Y., Jiang, Y.-C., Yang, D., et al. 2012, *Research in Astronomy and Astrophysics*, 12, 300
- Yang, S., Zhang, J., Li, T., & Liu, Y. 2011, *ApJ*, 732, L7
- Yokoyama, T., & Shibata, K. 1995, *Nature*, 375, 42
- . 1996, *PASJ*, 48, 353
- Young, P. R., & Muglach, K. 2014, *Sol. Phys.*, arXiv:1309.7324

Zhang, J., Ma, J., & Wang, H. 2006, ApJ, 649, 464

Zhang, J., Wang, J., & Liu, Y. 2000, A&A, 361, 759

Zhang, Q. M., Chen, P. F., Guo, Y., Fang, C., & Ding, M. D. 2012, ApJ, 746, 19

Zhang, Q. M., & Ji, H. S. 2014, A&A, 561, A134

Zheng, Y.-F., Wang, F., Ji, K. F., & Deng, H. 2013, Journal of Korean Astronomical Society, 46, 183

# Acknowledgments

I would like to express my sincere gratitude to my supervisors. Prof. Tetsuya Watanabe and Associate Prof. Takashi Sekii give a lot of times to discuss about my study and give helpful comments and suggestions on my thesis. I am grateful to Assistant Prof. Masumi Shimojo, who continuous guidance, encouragement, comments and suggestions of ideas during about 7 years are necessary for completion of this thesis. He also gave me first opportunity to be involved in solar physics, when I was an undergraduate student.

During the years, I had useful discussions with professors, researchers, and students of NAOJ, ISAS/JAXA, The graduate University for Advanced Studies (SOUKENDAI), Tokyo University, Nagoya University, HARVARD-SMITHONIAN CENTER FOR ASTROPHYSICS, and many other institutes. They gave me numerous helpful comments and I would like to acknowledge all of them.

*Hinode* is a Japanese mission developed and launched by ISAS/JAXA, collaborating with NAOJ as a domestic partner, NASA and STFC (UK) as international partners. Scientific operation of the *Hinode* mission is conducted by the *Hinode* science team organized at ISAS/JAXA. This team mainly consists of scientists from institutes in the partner countries. Support for the post-launch operation is provided by JAXA and NAOJ (Japan), STFC (U.K.), NASA, ESA, and NSC (Norway). I am thankful to the STEREO and SDO team for distributing SECCHI-EUVI-A&B and AIA data. This work was (partly) carried out on the Solar Data Analysis System operated by the Astronomy Data Center in cooperation with the *Hinode* Science Center of the National Astronomical Observatory of Japan.

Finally, I would like to express my warmest thanks to my parents and brother for their continuous support.